# Chapter 6

# Results and Discussion for Unsteady Measurements

## 6.1 Data Acquisition and Reduction

The unsteady voltage values $E(t')$ from the constant temperature anemometers, each connected to a hot-film sensor, were acquired by using a custom written Labview software program. This program also provided the control and the adjustment of the tunnel data acquisition hardware for the unsteady hot-film measurements. The number of samples taken in time for each unsteady maneuver was 1500. The unsteady voltage signals were acquired with a sample rate of 1000 Hz. Note that sampling frequency is well above the frequency response of the constant temperature anemometers (200 Hz). Total sampling time was 1.5 seconds. The actual maneuver covered approximately 0.33 seconds of this time period. The rest of the sampling time was spent for taking the pre-maneuver and the post-maneuver data. The pitch-up maneuver was executed 10 times at each roll angle position in order to reduce the uncertainty of unsteady data.

As used in the steady data reduction part, the measured unsteady values are represented as arrays of indexed variables in order to simplify the description of the data reduction procedure. In the unsteady data reduction process, the unsteady voltage value acquired from each anemometer can be written as

$$E(t') = E(t_j, s_k, r_l, \phi_m) \tag{6.1}$$

$$j = 1, ..., 1500 \qquad k = 1, ..., 15 \qquad l = 1, ..., 10 \qquad and \qquad m = 1, ..., nroll \tag{6.2}$$

where $t_j$ corresponds to a point in time; $s_k$ to the sensor number or the location; $r_l$ to the repetition number of the pitch-up maneuver; and $\phi_m$ to the DyPPiR roll angle of the model. Total number of the roll angles covered during the experiments, $nroll$, changes with respect to the model configuration. For the barebody case, 56 roll angle positions were covered. For the sail-on-side case, total number of roll angles was 117. However, data of the non-sail region and the data from sail region were reduced separately. For the non-sail region, total number of 71 roll angles were reduced, while for the sail side data reduction was made with 76 roll angles. The last 30 angles of the non-sail region and the first 30 angles of the sail side were the same. This was done in order to keep the continuity of the skin-friction distributions between the two regions during the smoothing process, which will be described later in this section.

The steps of the unsteady skin-friction data reduction can be outlined as follows:

1. At each roll angle position, the free-stream temperature $T(t_j, r_l, \phi_m)$, the dynamic pressure $q(t_j, r_l, \phi_m)$, and the atmospheric pressure $p(t_j, r_l, \phi_m)$ are calculated from the corresponding voltage values by the use of the calibration.

2. At each roll angle position, the plunge position $z(t_j, r_l, \phi_m)$ and the instantaneous angle of attack $\alpha(t_j, r_l, \phi_m)$ of the model are determined through the use of the DyPPiR plunge and pitch calibrations.

3. Each time point is non-dimensionalized by the reference time, $tref = L/U_\infty$ where $L$ is the model length and $U_\infty$ is the free-stream velocity.

4. Instantaneous skin friction values $C_f(t_j, s_k, r_l, \phi_m)$ for each roll angle, sensor and the repetition are calculated by

$$C_f(t_j, s_k, r_l, \phi_m) = \frac{\tau_w(t_j, s_k, r_l, \phi_m)}{q(t_j, r_l, \phi_m)} \tag{6.3}$$

   where $\tau_w$ is the unsteady wall shear stress value obtained by the use of King's law given by the equation 4.10

$$\tau_w(t_j, s_k, r_l, \phi_m) = \left[\frac{E^2(t_j, s_k, r_l, \phi_m) - A(s_k, \phi_m)}{B(s_k, \phi_m)}\right]^3 \tag{6.4}$$

In equation 6.4, $A(s_k, \phi_m)$ and $B(s_k, \phi_m)$ are the calibration coefficients obtained for each sensor by the procedure described in chapter IV. Note that at a particular roll angle position of the model, the calibration coefficients used in the unsteady measurements are the same as the ones used for the steady measurements, since the maneuvers are performed just after the last steady angle of attack and the change in the free-stream temperature between the steady and the unsteady measurements at a specific roll angle is negligible.

5. To reduce the noise in the unsteady measurements, the skin-friction values of each sensor, the plunge position and instantaneous angle of attack from 10 repetitions of the pitch-up maneuver performed at a specific roll angle position of the model are ensemble averaged:

$$C_{f_{avg}}(t_j, s_k, \phi_m) = \frac{\sum_{l=1}^{10} C_f(t_j, s_k, r_l, \phi_m)}{10} \tag{6.5}$$

$$z_{avg}(t_j, \phi_m) = \frac{\sum_{l=1}^{10} z(t_j, r_l, \phi_m)}{10} \tag{6.6}$$

$$\alpha_{avg}(t_j, \phi_m) = \frac{\sum_{l=1}^{10} \alpha(t_j, r_l, \phi_m)}{10} \tag{6.7}$$

6. Standard deviations $\sigma(t_j, s_k, \phi_m)$ of the ensemble averaged skin-friction values are calculated. The results from the unsteady experiments showed that the standard deviations of the ensemble averaged voltage values were two orders of magnitude smaller than the average values in most cases, therefore the unsteady data was highly repeatable and 10 repetitions for the pitchup maneuver at each roll angle position were sufficient to reduce the noise.

7. In order to determine the bad skin-friction values and exclude them from ensemble averaging, a statistical outlier detection method is used. In order to determine the outliers, a *student's* $t-$*distribution* is assumed for the 10 repetitions of the skin-friction values $C_f(t_j, s_k, r_l, \phi_m)$ at each roll angle position. Then the difference $d(t_j, s_k, \phi_m)$ from the mean value $C_{f_{avg}}(t_j, s_k, \phi_m)$ is calculated for each $C_f(t_j, s_k, r_l, \phi_m)$:

$$d(t_j, s_k, \phi_m) = \sqrt{\left[C_f(t_j, s_k, r_l, \phi_m) - C_{f_{avg}}(t_j, s_k, \phi_m)\right]^2} \tag{6.8}$$

and the condition

$$d \geq t \times \sigma(t_j, s_k, \phi_m) \tag{6.9}$$

is checked. Here $t$ value is chosen for 9 degrees of freedom with 90% confidence interval and equal to 1.833 (Holman [33]). The $C_f(t_j, s_k, r_l, \phi_m)$ values that satisfy the above condition are marked as outliers and their values are set to zero. The new $C_{f_{avg}}(t_j, s_k, \phi_m)$ are calculated by:

$$C_{f_{avg}}(t_j, s_k, \phi_m) = \frac{\sum_{l=1}^{10} C_f(t_j, s_k, r_l, \phi_m)}{10 - n_{outlier}} \tag{6.10}$$

where $n_{outlier}$ is the total number of outliers detected.

8. In order to reject the high frequency noise in $C_{f_{avg}}(t_j, s_k, \phi_m)$, a third-order digital Butterworth filter is used. As for the cutoff frequency, 20 Hz. is used. Wetzel [2] used the same value in the unsteady data reduction of the prolate spheroid work. In this study, different cutoff frequency values were tried. It has been seen that this value is high enough to preserve the frequency content and the magnitude of the unsteady data while filtering the high frequency noise.

9. Unsteady separation locations are obtained and the data are arranged for different output formats.

### 6.1.1 Determination of the unsteady separation locations

For the determination of the unsteady primary separation locations, $C_f = C_{f_{avg}}(t_j, s_k, \phi_m)$ vs. $\phi = \phi_m$ $(m = 1, ..., nroll)$ distributions for each sensor have to be analyzed. Since the actual maneuver starts at $t' = 3.0$ and ends at approximately $t' = 10.3$, there is no need to consider all the time steps in the maneuver. Between these two time values, a total number of 40 equally spaced time points are used. This corresponds to a time increment of $\Delta t = 0.01$ seconds between the start of the pitch-up and the end of the maneuver. The total number of time points to be used in the separation location determination is obtained as a result of many trials and it has been seen that further increase of the total number of points does not change the unsteady separation pattern obtained with 40 points.

An automated scheme is needed to find the unsteady separation locations at each time step and the sensor location, since it is impossible to determine the separation locations graphically (as done in the steady case) due to the large number of data sets to be examined. For this purpose, three methods were tried: in the first method, the minimum in

$C_f$ from each unsteady circumferential distribution is determined and the corresponding $\phi$ is taken to be the unsteady separation location. However, this method is not robust and accurate enough in the presence of outliers or wiggles in the separation region and gives misleading results. In the second method, after the minimum in $C_f$ is determined, a quadratic curve is fit to the concave separation region by the least squares method. In the fit process 11 $(C_f, \phi)$ points are used with the center value being the minimum of $C_f$ obtained from the first method. This helps smoothing the data near the separation region and improves the separation location determination. However, as observed in most of the actual cases, the $C_f$ distribution in the separation region is not symmetric with respect to the minimum $C_f$ value, therefore using a quadratic fit shifts the minimum from the true value. This offset is not constant for each distribution, so a bias correction to the data cannot be applied. The third method removed the problems encountered in the previous methods. In this approach, the *loess* method is used as described in the steady data reduction of the sail-on-side case. This method is considered in order to smooth the $C_f$ vs. $\phi$ distributions at each time step without changing the circumferential skin-friction pattern and to exclude the deviant points that distort the smoothed data. By using this technique, the asymmetry in the vicinity of the separation location is preserved, while the noise from the data is removed. The magnitude changes in the skin-friction values due to smoothing is found to be within the uncertainties. As a result, this last method is used to find the unsteady separation locations and to obtain the $C_f$ vs. $\phi$ distributions at each time step.

## 6.2 Unsteady Flow Topology

One of the methods to investigate the difference between the steady and the unsteady flow over the model is to compare the steady $C_f$ vs. $\phi$ distribution obtained at a certain pitch angle $\alpha$ with the unsteady one acquired at the corresponding instantaneous pitch angle $\alpha(t')$ for a specific $x/L$ location. Figures 6.1 through 6.39 show this comparison for all the $x/L$ locations of the sensor set B. Figures from 6.1 to 6.13 give the barebody results. Figures 6.14 to 6.26 show the data of the non-sail region of the sail-on-side case, and the figures between 6.27 and 6.39 give the comparison of the region with the sail. Note that, for each figure, the steady angle of attack and the instantaneous angle of attack are the same. The non-dimensional time $t'$ corresponding to the instantaneous

angle of attack is also shown in each figure. All the unsteady experiments were done with the slotted walls.

Unsteady $C_f$ distribution of the barebody case and the non-sail region of the sail-on-side case show similar trends compared to the steady distributions of each. As seen from figures 6.1 and 6.14, at $\alpha = 3.1\,^\circ$, the skin-friction magnitudes of the steady and the unsteady cases are approximately the same and the distributions of both are flat profiles. As the steady angle of attack is increased, the steady data start to deviate from this flat profile, and minima in $C_f$ distributions indicating primary separation can be observed. However, the unsteady skin-friction pattern remains approximately flat until $\alpha(t') = 13.2\,^\circ$. At this instantaneous angle of attack, the unsteady primary separation starts to develop at the downstream stations starting from $x/L = 0.706$. Figures 6.6 and 6.19 show the $C_f$ distributions at this angle of attack for the barebody and the sail-on-side case respectively. At higher angles of attack, the difference between the steady and the unsteady flow separation pattern is more obvious. At $\alpha = 21.4\,^\circ$, in figures 6.10 and 6.23, steady primary separation starts from $x/L = 0.266$ and shifts towards the windward side at the downstream stations. The unsteady separation can be first located at $x/L = 0.345$ and also moves towards the windward side as $x/L$ increases. Compared to the steady primary separation locations at the same $x/L$ stations, the unsteady separation locations are found to be more leeward. In particular, at $x/L = 0.501$, the primary separation location for the steady data is $\phi = 122^\circ$, while the unsteady primary separation occurs at $\phi = 136\,^\circ$ for the barebody case. From the same figures, another important observation can be made about the secondary flow separation. In the steady case, secondary separation starts to develop at $x/L = 0.434$, and can be seen as the second minima of the $C_f$ for the rest of the stations downstream. On the other hand, no secondary separation formation can be detected at any of the $x/L$ stations for the unsteady case. A weak unsteady secondary separation can be seen at the last instantaneous angle of attack $\alpha(t') = 27.6\,^\circ$, at the last four $x/L$ stations. As previously described in the steady results, at the first three stations on the nose region, a weak separation/reattachment pattern can be seen on the leeward side of the model at high steady angles of attack. However, this flow behavior cannot be observed for the unsteady case at the corresponding instantaneous angles of attack. In general, the magnitudes of the unsteady $C_f$ are lower than that of the steady ones at the same angle of attack and the $x/L$ location. This difference can be observed starting from $\alpha = 5.1\,^\circ$ and become

more obvious at higher angles of attack, especially on the leeward side of the model.

For the sail region, the unsteady data start to deviate from the steady $C_f$ values even at the first instantaneous angle of attack $\alpha(t') = 3.1\,^\circ$. In figure 6.27, the disturbances created by the sail can be seen on the $C_f$ distribution at the stations just downstream of the sail for the steady case, while the unsteady data do not show the same trend but follow a more flat pattern. (Note that the unsteady $C_f$ values at $x/L = 0.266$ are not shown for the $\phi$ values after $256\,^\circ$ in figures 6.27 through 6.39, since the data at these locations were too scattered and could not be distinguished from the noise.) No clear unsteady separation pattern like the first or the second minima seen in the steady case can be observed up to $\alpha(t') = 13.2\,^\circ$. After this angle of attack, minima in the $C_f$ indicating the unsteady separation can be located. As also seen in the steady case, the unsteady separation structure of the sail side is different from the unsteady crossflow separation topology observed on the barebody and the non-sail region of the sail-on-side case. Again, no clear categorization of the separation locations could be made. From figure 6.38, for $\alpha(t') = 25.5\,^\circ$, the second minima in the unsteady $C_f$ distributions at the sensor stations downstream of $x/L = 0.638$ can be seen to appear more leeward compared to the second minima of the steady case.

The results above show that in unsteady flows the separation topology is different from the one in an equivalent steady configuration. For the barebody and the non-sail region of the sail-on-side case, this difference originates from the fact that the unsteady separation location lags the steady separation. This can be clearly seen from the figures 6.40 through 6.59 where the quasi-steady and the unsteady primary separation locations are plotted against the non-dimensional time $t'$ for different $x/L$ stations. The quasi-steady data distribution are formed by first taking the steady separation locations and the corresponding steady angles of attack at a certain $x/L$ location. By using the DyPPiR pitch feedback data, the instantaneous angles of attack that match with the steady angles are selected. Then the non-dimensional time $t'$ for each steady separation location can be obtained and quasi-steady data as a function of $t'$ can be generated. Open symbols stand for the quasi-steady data and the filled symbols represent the unsteady data. For a better understanding of the mathematical difference between the steady, quasi-steady, and the unsteady separation locations, the functional relations that are defined in chapter 1 should be referred.

Figures 6.40 to 6.49 show the separation locations for the barebody case, and the figures

from 6.50 to 6.59 give the primary separation locations for the non-sail region of the sail-on-side case. In these figures, the horizontal distance between the unsteady and the steady separation location is an indication of the presence of a time lag. Since the maneuvers were performed with a constant pitch rate, the instantaneous pitch angle is a linear function of $t'$. By considering this fact in examining figures 6.1 to 6.26, it can also be thought that at an instantaneous pitch angle, for a specific $x/L$ location, the primary unsteady separation starts more leeward compared with the steady case. Therefore the total separated region occupies a smaller area, both on the model surface and in the flow field.

To understand why a lag exists, as described by Wetzel and Simpson [3], one should examine the path of a fluid particle during the maneuver. During the pitch-up maneuver, a fluid particle originally starts its trajectory on the windward side of the model at a lower angle of attack. Therefore, the particle experiences a less severe adverse pressure gradient along its path, and can travel farther around the leeside before separating when compared with a similar particle in a steady flow field. This history effect, the true total path the particle has traversed, differentiates the unsteady flow field from the steady one.

Figures 6.60 through 6.66 show the quasi-steady and the unsteady separation locations as a function of $t'$ at seven $x/L$ stations for the sail region of the sail-on-side case. The separation locations correspond to the second minima (at high $\alpha(t')$ these become the only minima as in the steady case) of the $C_f$ distributions measured from $\phi = 180\,^\circ$. Figures 6.60 and 6.61 show that the unsteady separation locations are approximately the same as the steady ones within the uncertainties at $x/L = 0.434$ and $x/L = 0.501$. At these stations, the unsteady separation locations are detected for the time points starting from $t' \simeq 8.0$ and the $\phi$ values of the separation locations are constant. At the other stations, $x/L = 0.570$, 0.638, 0.706, 0.774, and 0.819, the unsteady separation locations are more leeward compared to the quasi-steady ones at a given $t'$ during the maneuver and they approach the steady values at the end of the maneuver. The difference between the unsteady and the quasi-steady data gets bigger as $x/L$ increases.

Maybe the most important observation that can be made from these figures is about the unsteady separation pattern in the sail region as a function of $t'$. Except for $x/L = 0.434$ and 0.501, the unsteady separation data do not reach any of the steady separation locations at any instant of time during the maneuver. In other words, unsteady separation pattern do not follow the quasi-steady data with a time lag. In fact, a lag definition as

described for the unsteady crossflow separation may not be appropriate for the sail side separation topology based on the results obtained in this study. The results also indicate the complex nature of the unsteady flow separation on the sail side.

## 6.3 Time-Lag Models

The main interest is to be able to model or approximate the time lags associated with the unsteady flow fields. If one can determine the real physics behind the time-lag formation and approximate the lags with reasonable accuracy, then by using the quasi-steady data that are constructed through the use of the steady flow field information, the unsteady flow features such as unsteady skin-friction, force and moment coefficients can be estimated. In the next two sections, algebraic time-lag modelling and a first order differential time-lag model will be described with their application to the current study.

### 6.3.1 Algebraic Time-lag Models

Algebraic time lag modeling was a commonly used approach in the previous studies. Most of the algebraic time lag models are based on finding an effective angle of attack $\alpha_{eff}$ by using the descriptions of the flow kinematics. If a model rotates about some point $x_{cg}$ at a constant pitch rate $\dot{\alpha}$, a relative velocity normal to the model axis $\dot{\alpha}(x - x_{cg})$ will exist at other $x/L$ locations in addition to the velocity of the wind relative to the point of rotation. By using this fact, Montividas et al. [9] approximated an effective angle of attack as:

$$\alpha_{eff} = \alpha - \Delta\alpha_{eff} \tag{6.11}$$

where

$$\Delta\alpha_{eff} = \dot{\alpha}\frac{x_{cg} - x}{U_\infty} \tag{6.12}$$

However, this approximation did not describe the unsteady effects in their flow field associated with the onset of asymmetric vortex shedding at high angles of attack on ogive cylinders.

Ericsson [34] also studied the same problem and extended the effective angle of attack idea by including the convective lag effects in the flow field. He used the fact that a

vortex at a downstream station of the apex of the model (ogive cylinder) will react to the changed flow conditions at the apex at a time $\Delta t$ later. He also approximated that the disturbances originating at the apex of the model would propagate downstream with the free-stream velocity $U_\infty$ which would give $\Delta t = x/U_\infty$. Using equations 6.11 and 6.12, the effective angle of attack at the apex of the model ($x = 0.0$) can be obtained as:

$$\alpha_{eff_A} = \alpha - \dot{\alpha}\frac{x_{cg}}{U_\infty} \tag{6.13}$$

According to Ericsson's theory, the effective angle of attack $\alpha_{eff}(x, t')$ determining the vortex characteristics at station $x$ downstream of the apex, is

$$\alpha_{eff}(x, t') = \alpha_{eff_A}(0, t - \Delta t) \tag{6.14}$$

where $\Delta t = x/U_\infty$. By using the Taylor series expansion at $t$ for the effective angle of attack at the apex and assuming small non-dimensional rotation rates, $(\dot{\alpha}L/U_\infty) << 1$, one can write

$$\alpha_{eff}(x, t') = \alpha_{eff_A}(t) - \Delta t\frac{\partial \alpha_{eff_A}}{\partial t} \tag{6.15}$$

which gives

$$\alpha_{eff} = \alpha - \dot{\alpha}\frac{x_{cg} + x}{U_\infty} \tag{6.16}$$

Using the definition given by the equation 6.11, we can obtain $\Delta\alpha_{eff}$ from equation 6.16 as:

$$\Delta\alpha_{eff} = \dot{\alpha}\frac{x_{cg} + x}{U_\infty} \tag{6.17}$$

Equation 6.17 did approximate the lags in asymmetric vortex shedding on the pitching ogive cylinder successfully.

In this study, $\Delta\alpha_{eff}$ has been calculated both from the barebody experimental results and equation 6.17 for four different $x/L$ locations. Since the pitch rate has a constant value of $78\,^\circ/s$, the lag equation 6.17 gave constant $\Delta\alpha_{eff}$ values for each $x/L$ locations. For calculating $\Delta\alpha_{eff}$ from the experimental results, certain number of unsteady separation locations $\phi_{sep}$ and corresponding instantaneous pitch angles $\alpha(t')$ have been selected from the data. Then the same $\phi_{sep}$ values for the steady data and the corresponding steady pitch angles have been picked. For a specific $\phi_{sep}$, the difference between the instantaneous pitch angle and the steady pitch angle has been calculated as the effective angle of attack increment. The $\Delta\alpha_{eff}$ results obtained from equation 6.17 and the experimental

data have been compared in figure 6.67. As can be seen from this figure, there is a significant difference between experimental $\Delta\alpha_{eff}$ and the one calculated from equation 6.17. Especially for the stations $x/L \geq 0.501$, the magnitudes of the experimental $\Delta\alpha_{eff}$ are twice as much higher than that of obtained by using the model equation 6.17. Also, although the pitch rate is constant, experimental $\Delta\alpha_{eff}$ does change with the instantaneous pitch angle thus with the time. This comparison shows the difference between the lags in the unsteady crossflow separation over the model used in the present experiment and the flowfield associated with the asymmetric vortex shedding on the ogive cylinder. A more sophisticated time-lag modeling technique should be used in order resolve the complex nature of the time history effects on the unsteady cross flow separation locations.

### 6.3.2 First-Order Differential Time-Lag Model

Goman and Khrabrov [35] have developed a first order time lag model in order to approximate the time history of a dominant flow feature such as the separation location in general unsteady flows. They applied this model to pitching two-dimensional airfoils, delta wings and the unsteady aerodynamics of a complex fighter aircraft configuration as well. They used the separation location as an internal state variable, and defined the forces and moments as functions of this state variable. For a given maneuver, by obtaining the time history of this state variable, they were able to calculate the unsteady force and moments. This model mainly introduces a first-order delay differential equation for an internal state variable $x$ which accounts for unsteady effects associated with separated and vortex flow. The variable $x$ may represent the location of trailing edge flow separation on a pitching airfoil or that of vortex breakdown on a delta wing. The original form of the differential equation governing $x$ is given by:

$$\tau_1 \frac{dx}{dt} + x = x_0(\alpha - \tau_2 \frac{d\alpha}{dt}) \tag{6.18}$$

where $\tau_1$ and $\tau_2$ are time constants and $x_0$ describes the steady dependency of $x$ on $\alpha$. Goman and Khrabrov [35] defined $\tau_2$ as a quasi-steady time delay associated with changes in circulation, boundary layer convection lags, and/or boundary layer improvement effects, while $\tau_1$ as a relaxation time constant associated with global transient aerodynamic effects, or dynamic properties of the separated flow adjustment.

Wetzel and Simpson [3] implemented an extended version of this model for approximating

the time varying nature of the unsteady separation locations over the maneuvering prolate spheroid. The approximation successfully fit the experimental unsteady separation locations and non-dimensional time lag values for different $x/L$ stations of the prolate spheroid. The same extended version of the first-order differential lag model has been used in this study in order to approximate the unsteady primary separation locations of the barebody and the non-sail region of the sail-on-side case:

$$\tau' \left(\frac{x}{L}\right) \frac{d\phi_{uns}}{dt'} + \phi_{uns}\left(\frac{x}{L}, t'\right) = \phi_0\left(\frac{x}{L}, \alpha(t')\right) \tag{6.19}$$

In equation 6.19, $\phi_{uns}$ represents the approximation to the unsteady separation location and $\tau'$ stands for the first-order non-dimensional time lag. The $\phi_0$ is the quasi-steady separation location distribution which can be obtained from the steady separation data at each $\alpha = \alpha(t')$. Note that both the quasi-steady separation location $\phi_0$ and the approximation to the unsteady separation location $\phi_{uns}$ do also vary with $x/L$. This is one of the differences between the extended version and the original time lag model of Goman & Khrabrov [35]. In the original version, a single point of separation was considered. However, for the present study and the prolate spheroid case, since the crossflow separation occurs along a line rather than a point, $\phi_{uns}$ and $\phi_0$ were also functions of $x/L$. It should also be noted that the time lag $\tau'$ taken as an unknown in equation 6.19 is let to vary in $x/L$ and identified by fitting the model equation with the experimental data.

The first-order differential equation 6.19 mainly correlates the unsteady separation locations to the quasi-steady data by the time lag $\tau'$. Note that if we solve equation 6.19 at a constant $x/L$ location, the only dependent variable would be the non-dimensional time $t'$. Then the solution to this initial value problem can be obtained by first taking the Laplace transform of each side:

$$\tau' \left[s\phi_{uns}(s) - \phi_{uns}(0)\right] + \phi_{uns}(s) = \phi_0(s) \tag{6.20}$$

After rearranging the above equation, we obtain:

$$\phi_{uns}(s) = \frac{\phi_{uns}(0)}{s + \frac{1}{\tau'}} + \frac{1}{\tau'}\left(\frac{\phi_0(s)}{s + \frac{1}{\tau'}}\right) \tag{6.21}$$

Now if we take the inverse Laplace transform of each side of equation 6.21, we can get the final expression for $\phi_{uns}(t')$ as:

$$\phi_{uns}(t') = e^{-t'/\tau'}\left[\phi_{uns}(0) + \frac{1}{\tau'}\int_0^{t'} \phi_0(\beta) e^{\beta/\tau'} d\beta\right] \tag{6.22}$$

In the solution procedure, the quasi-steady separation distribution $\phi_0$ was obtained by fitting a cubic spline to the steady data. The independent variable was $t'$ in the fitting procedure. As the initial value for $\phi_{uns}$, the first steady separation location in the steady data was used. Since equation 6.22 represents the solution to an initial value problem, the determination of the initial value for $\phi_{uns}$ and thus the first steady separation location is important. However, in terms of getting the right time lag value, the choice of the initial value does not have a crucial role. As long as the pitch rate $\dot{\alpha}$ is constant, the same time lag will be obtained even if the initial value is slightly different than the true value and the uncertainty in the initial value will only effect the initial transient part. The integral on the right hand side of the equation 6.22 was evaluated numerically for each $t'$ value by using the trapezoidal approximation. For each $x/L$ station, the model equation 6.22 was solved with different values of the $\tau'$ in an iterative manner. The root mean square error between the approximated and experimental unsteady data was calculated at each iteration and the $\tau'$ that gave the smallest error had been chosen for that specific $x/L$ location.

The solid lines in figures 6.40 through 6.59 show the results of the time lag model approximation to the unsteady data at ten $x/L$ locations for the barebody and the non-sail region of the sail-on-side case. Note that all the stations were not used in calculating the time lags. At the stations $x/L \leq 0.266$, no unsteady separation location at any instant of time was observed. At the last station $x/L = 0.863$, the determination of the unsteady separation location was not accurate enough because of the flat nature of the $C_f$ profile near the minimum. For the rest of the stations, the first-order lag model approximation fits the measured unsteady separation locations reasonably well. In these graphs, for some of the $x/L$ locations, the last value of the unsteady and the steady separation locations are slightly different although they should be the same ideally. However, the differences are within the uncertainty of separation locations that is $\pm 2\,^\circ$. The model fit results show that the first-order differential lag model of Goman and Khrabrov does capture the time-varying nature of the unsteady crossflow separation locations reasonably and may be used as part of the unsteady aerodynamic models used to describe the physics of such flows.

Since the unsteady separation locations do not follow the quasi-steady separation data with a time lag, a first-order lag model approximation to the unsteady data of the sail side cannot be obtained. The physical model given by the differential equation 6.19 does

not describe the unsteady separation phenomena of the sail side. In order to approximate the sail side unsteady separation pattern, a more complicated physical model should be developed.

### Time lags

The time lag values $\tau'$ obtained from the first-order differential lag model equation fits for different $x/L$ locations are shown in figure 6.68. In this figure, circles represent the time lags of the barebody case, and the triangles stand for the results of the non-sail region of the sail-on-side case. For the barebody case, near the model rotation point $x_{cg}/L = 0.24$, the time lag value is close to zero indicating that the quasi-steady data follows the unsteady data closely. Then an increase until $x/L = 0.434$ can be seen. Since there are not enough points in this region, the nature of this increase (linear or non-linear) cannot be determined accurately. After this point, the time lag stays approximately constant between $x/L = 0.434$ and $x/L = 0.774$, taking an average value of 1.40. At $x/L = 0.819$, this value drops to 1.24. The non-dimensional time lag $\tau'$ vs. $x/L$ distribution of the non-sail region shows a similar trend as the one obtained for the barebody case. However, at the first two stations, the time lag values are considerable higher than the barebody values. For the other stations, time lags are approximately constant with an average value of 1.50.

Both the barebody and the non-sail region $\tau'$ vs $x/L$ distributions are different from the one obtained for the prolate spheroid by Wetzel and Simpson [3]. In that case, $\tau'$ changed approximately in a linear manner increasing in downstream direction over the prolate spheroid model. By making a linear fit to the time lag data and using the Ericsson's $\Delta\alpha_{eff}$ approach (see equation 6.17) with an unknown convection velocity $U_c$ for the propagation speed of the disturbances, Wetzel and Simpson [3] were able to determine that the disturbances propagate with a convection velocity of $U_c \simeq 0.3 \times U_\infty$. It should be noted that, for the prolate spheroid pitch-up maneuvers, the model center of rotation point was at $x/L = 0.5$, whereas in this study the rotation point is at $x/L = 0.24$. Also the Suboff model has a different geometry than the prolate spheroid, having a large proportion of a constant diameter region. Therefore, one may expect an influence of the rotation point and the model geometry on the time lags. However further study has to be done in order investigate the true complex nature of the time lags associated with the

unsteady flow field over this undersea vehicle geometry.

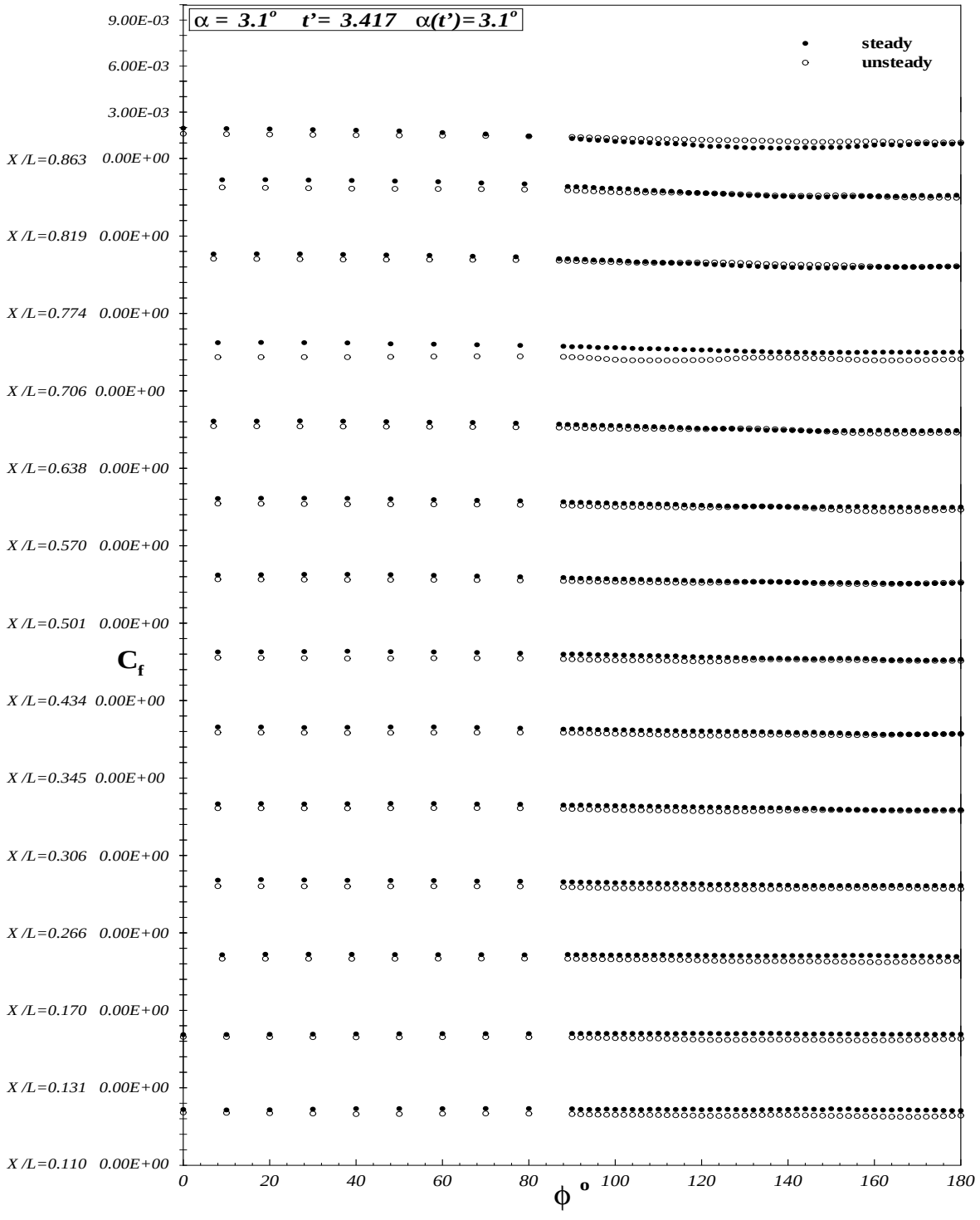


Figure 6.1: Comparison of barebody $C_f$ vs. $\phi$ distribution for steady and unsteady data at all $x/L$ locations. $\alpha = 3.1\,^\circ$, $t' = 3.417$, $\alpha(t') = 3.1\,^\circ$.

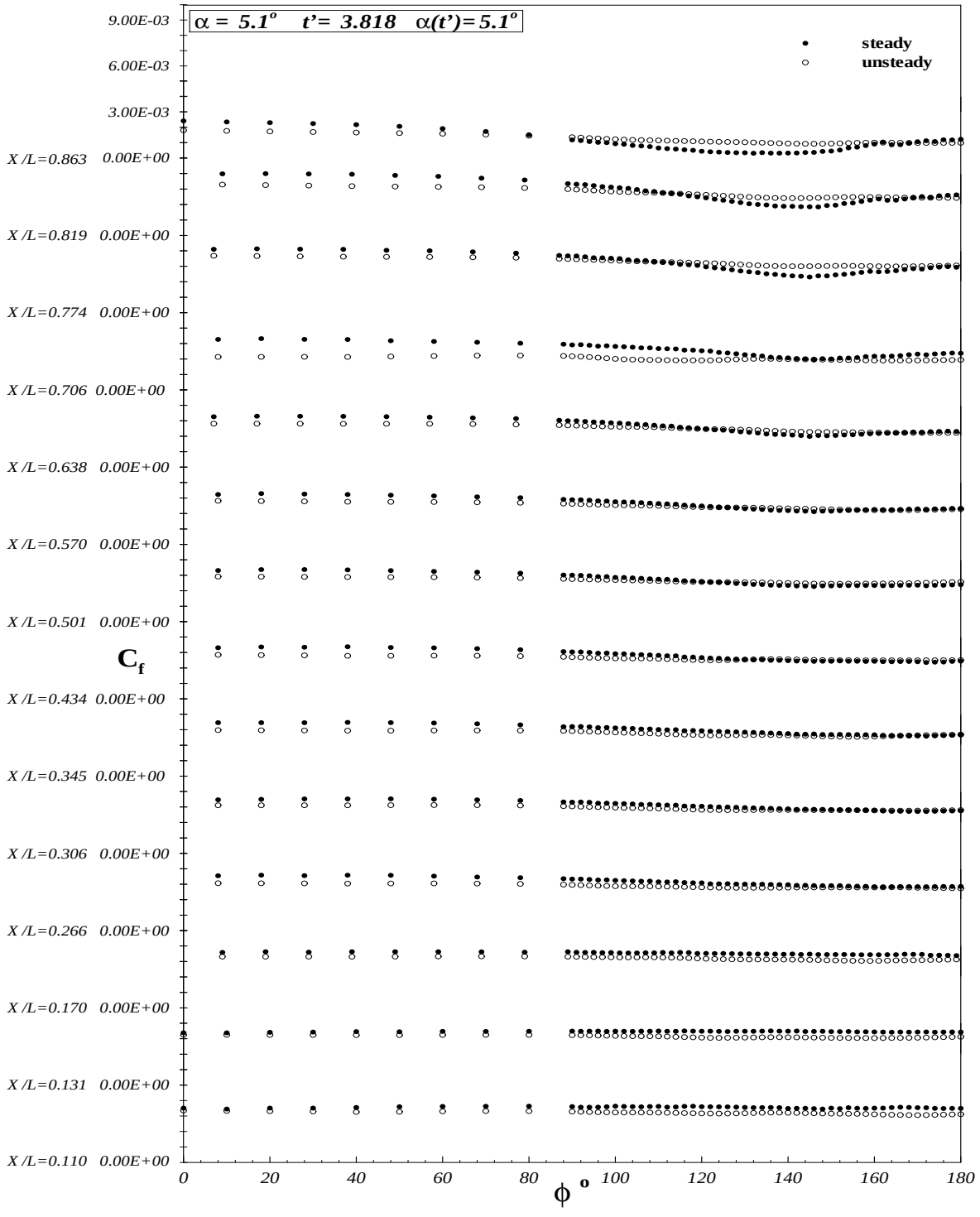


Figure 6.2: Comparison of barebody $C_f$ vs. $\phi$ distribution for steady and unsteady data at all $x/L$ locations. $\alpha = 5.1\,^\circ$, $t' = 3.818$, $\alpha(t') = 5.1\,^\circ$.

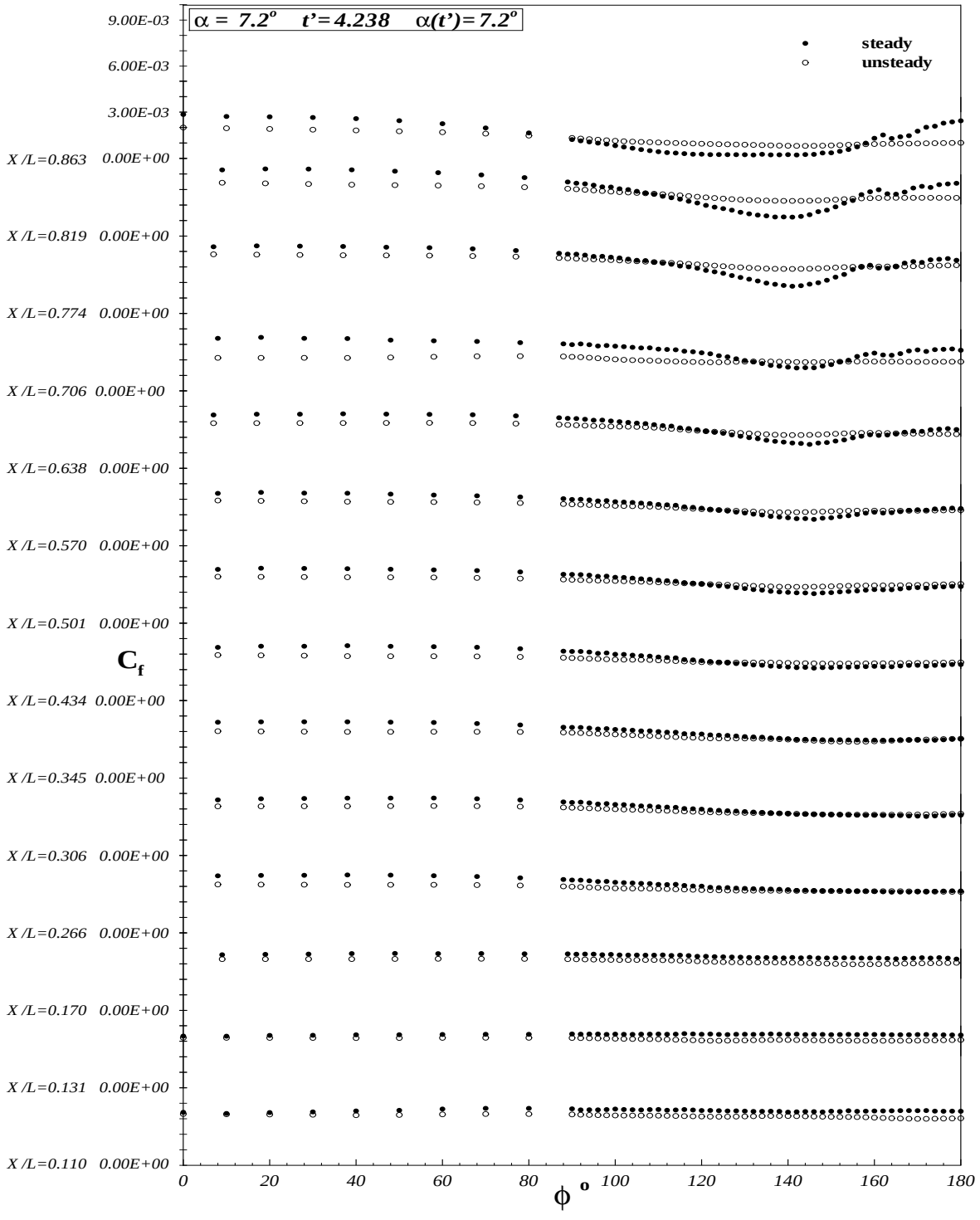


Figure 6.3: Comparison of barebody $C_f$ vs. $\phi$ distribution for steady and unsteady data at all $x/L$ locations. $\alpha = 7.2\,^\circ$, $t' = 4.238$, $\alpha(t') = 7.2\,^\circ$.

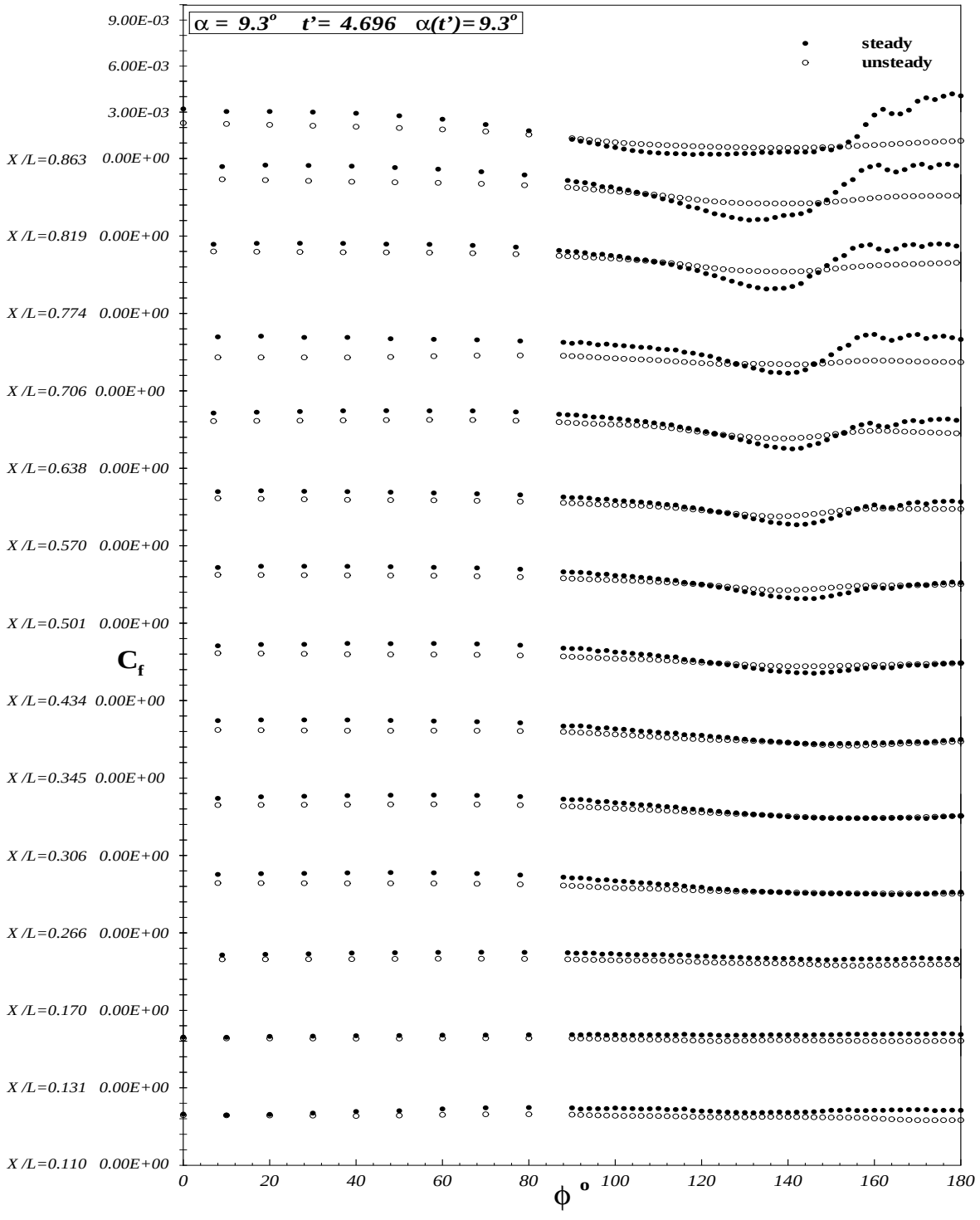


Figure 6.4: Comparison of barebody $C_f$ vs. $\phi$ distribution for steady and unsteady data at all $x/L$ locations. $\alpha = 9.3\,^\circ$, $t' = 4.696$, $\alpha(t') = 9.3\,^\circ$.

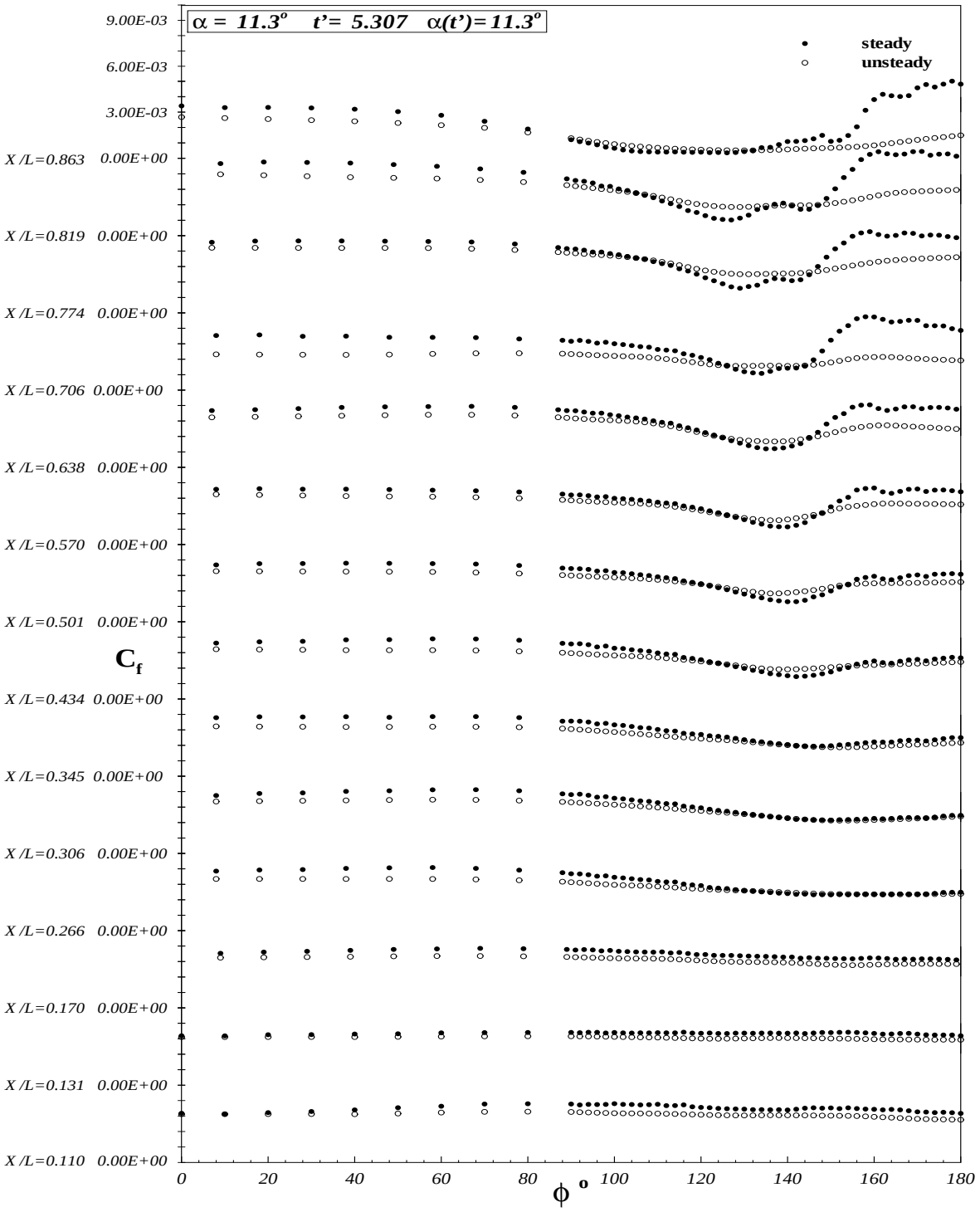


Figure 6.5: Comparison of barebody $C_f$ vs. $\phi$ distribution for steady and unsteady data at all $x/L$ locations. $\alpha = 11.3\,^\circ$, $t' = 5.307$, $\alpha(t') = 11.3\,^\circ$.

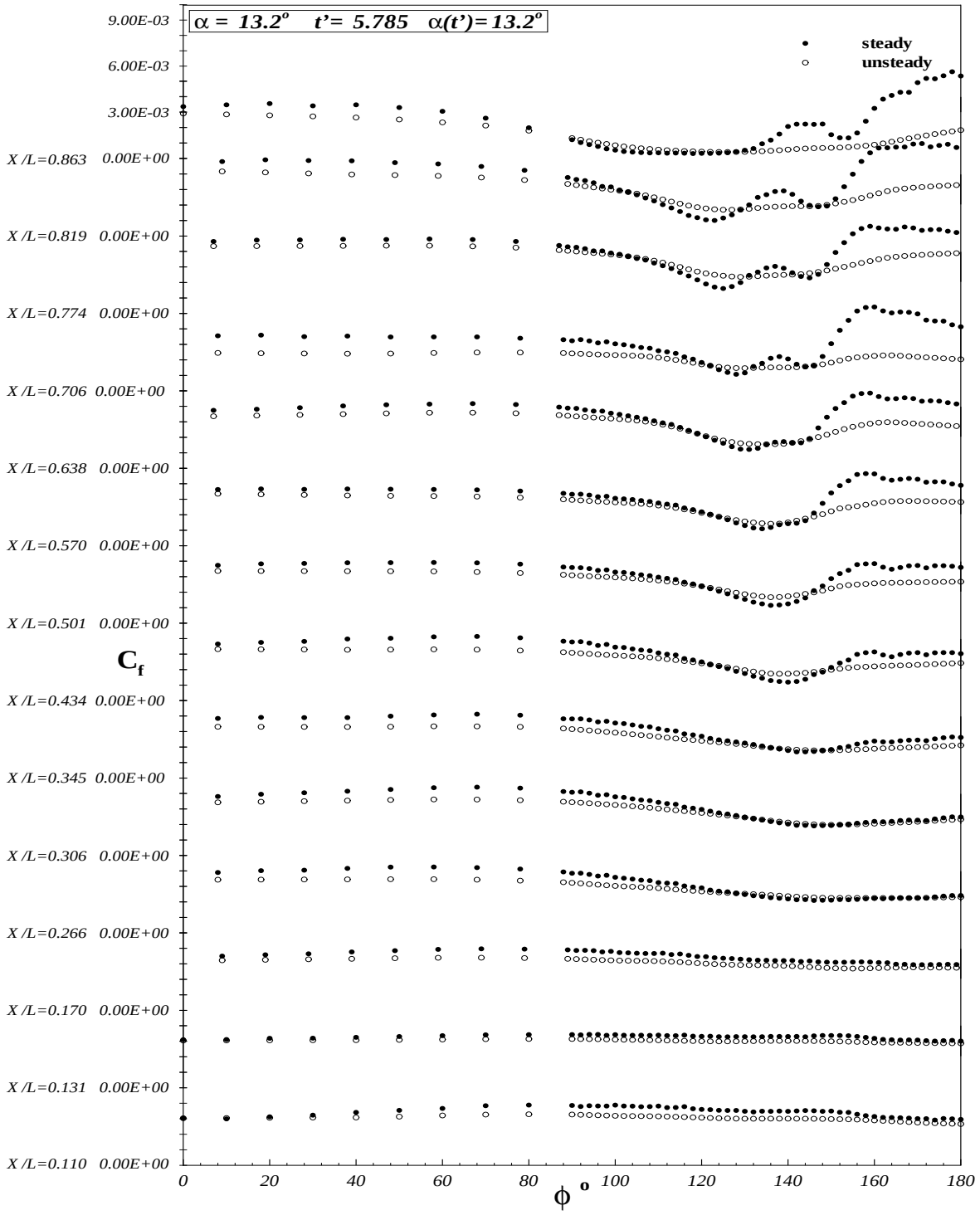


Figure 6.6: Comparison of barebody $C_f$ vs. $\phi$ distribution for steady and unsteady data at all $x/L$ locations. $\alpha = 13.2\,^\circ$, $t' = 5.785$, $\alpha(t') = 13.2\,^\circ$.

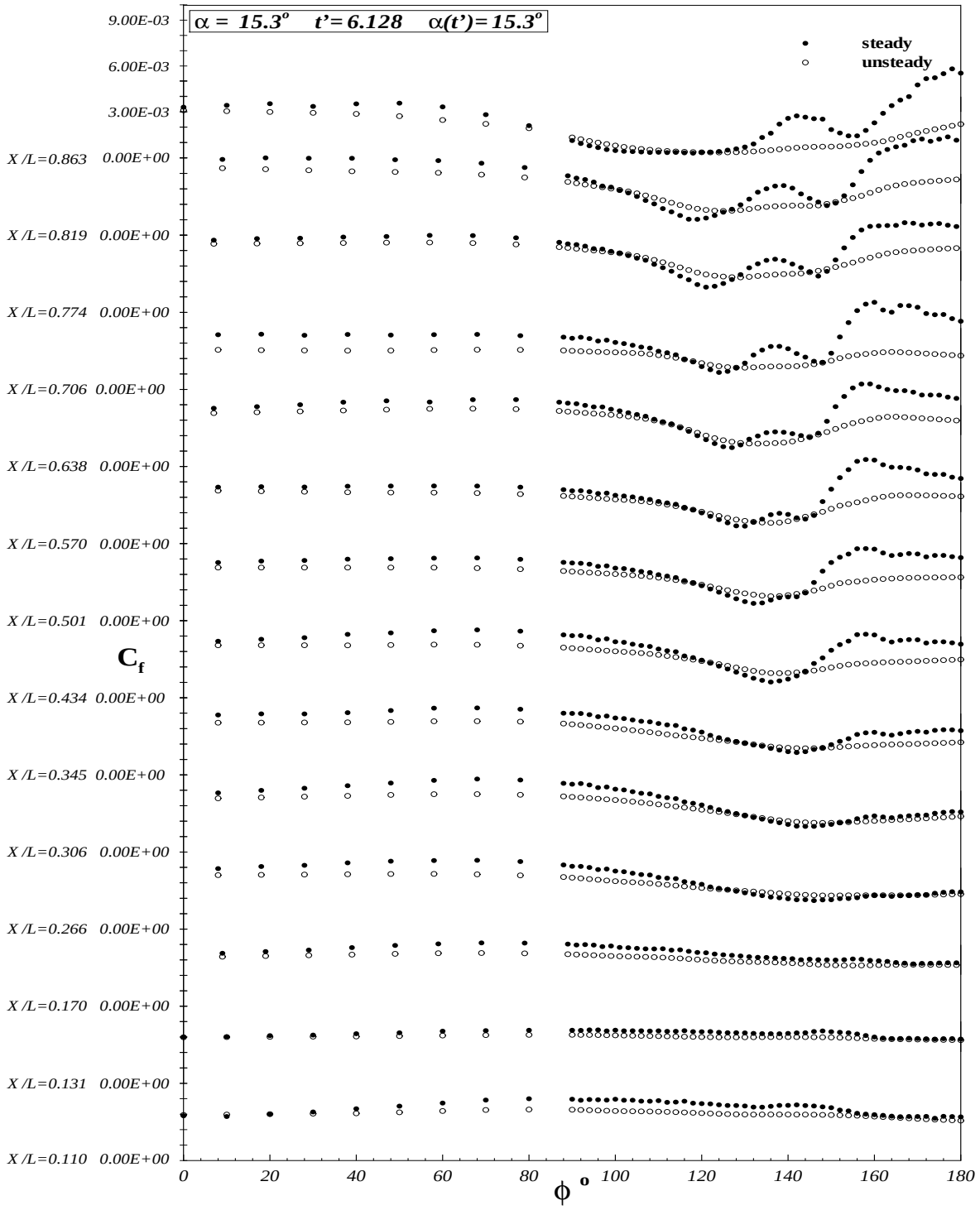


Figure 6.7: Comparison of barebody $C_f$ vs. $\phi$ distribution for steady and unsteady data at all $x/L$ locations. $\alpha = 15.3\,^\circ$, $t' = 6.128$, $\alpha(t') = 15.3\,^\circ$.

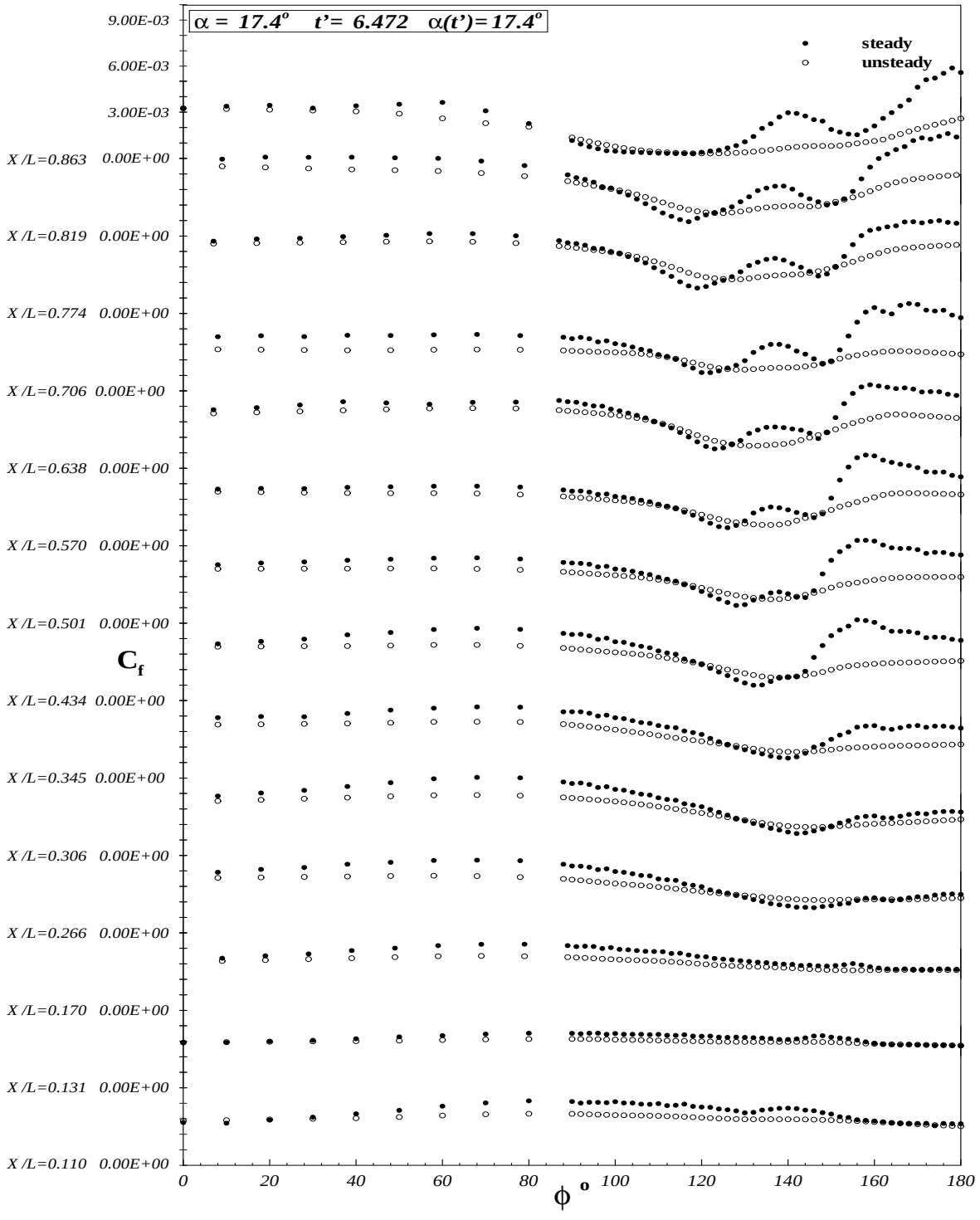


Figure 6.8: Comparison of barebody $C_f$ vs. $\phi$ distribution for steady and unsteady data at all $x/L$ locations. $\alpha = 17.4\,^\circ$, $t' = 6.472$, $\alpha(t') = 17.4\,^\circ$.

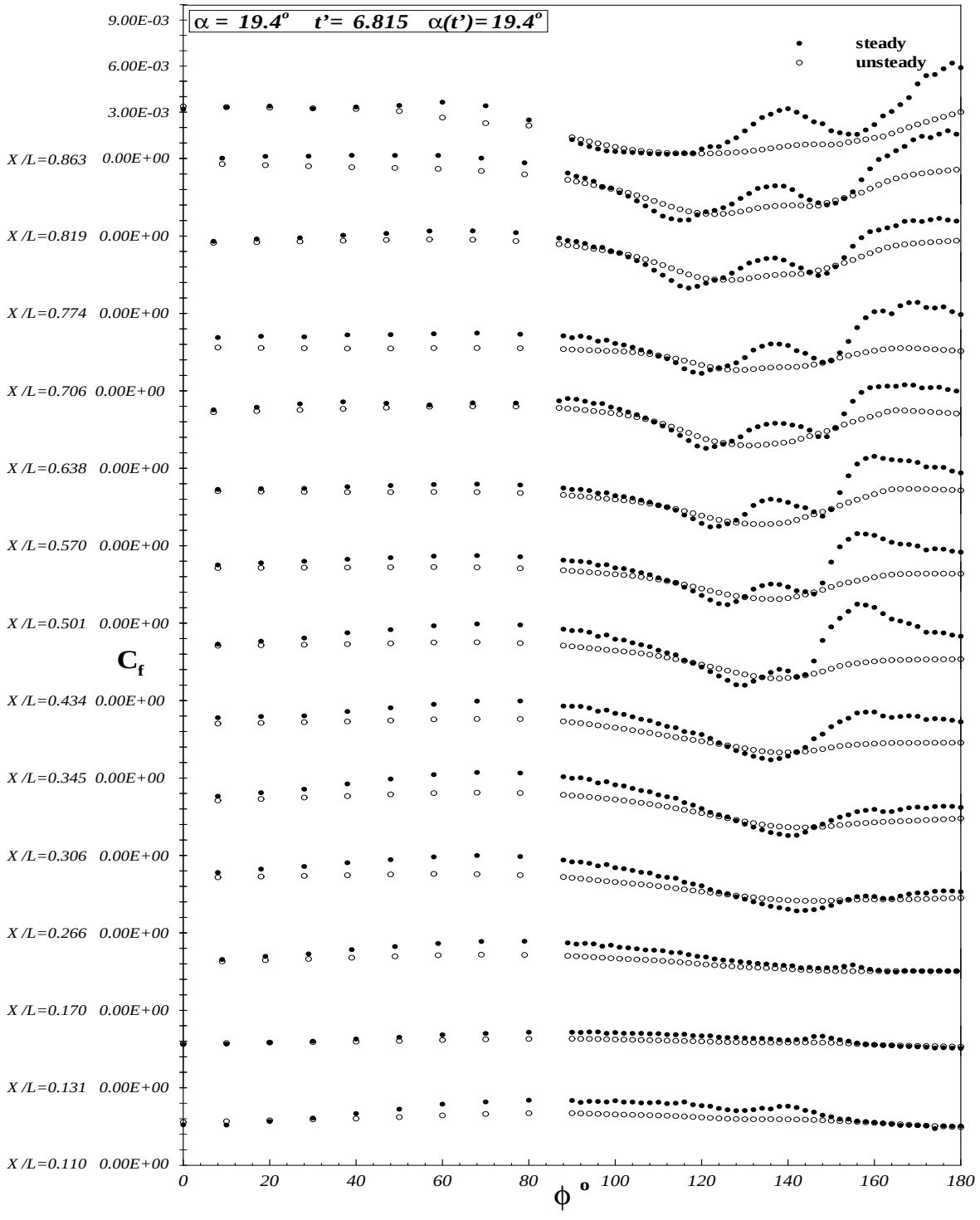


Figure 6.9: Comparison of barebody $C_f$ vs. $\phi$ distribution for steady and unsteady data at all $x/L$ locations. $\alpha = 19.4\,^\circ$, $t' = 6.815$, $\alpha(t') = 19.4\,^\circ$.

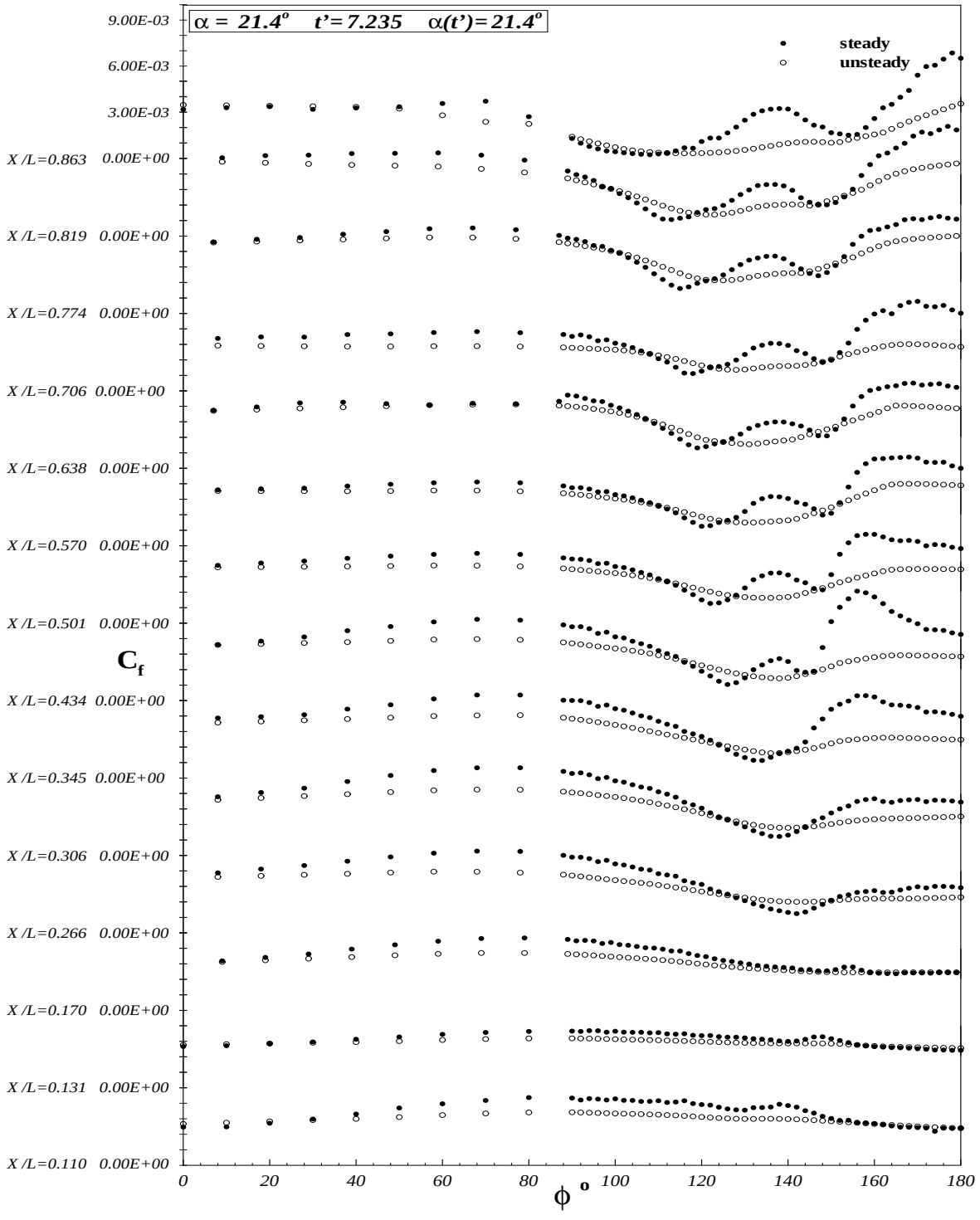


Figure 6.10: Comparison of barebody $C_f$ vs. $\phi$ distribution for steady and unsteady data at all $x/L$ locations. $\alpha = 21.4\,^\circ$, $t' = 7.235$, $\alpha(t') = 21.4\,^\circ$.

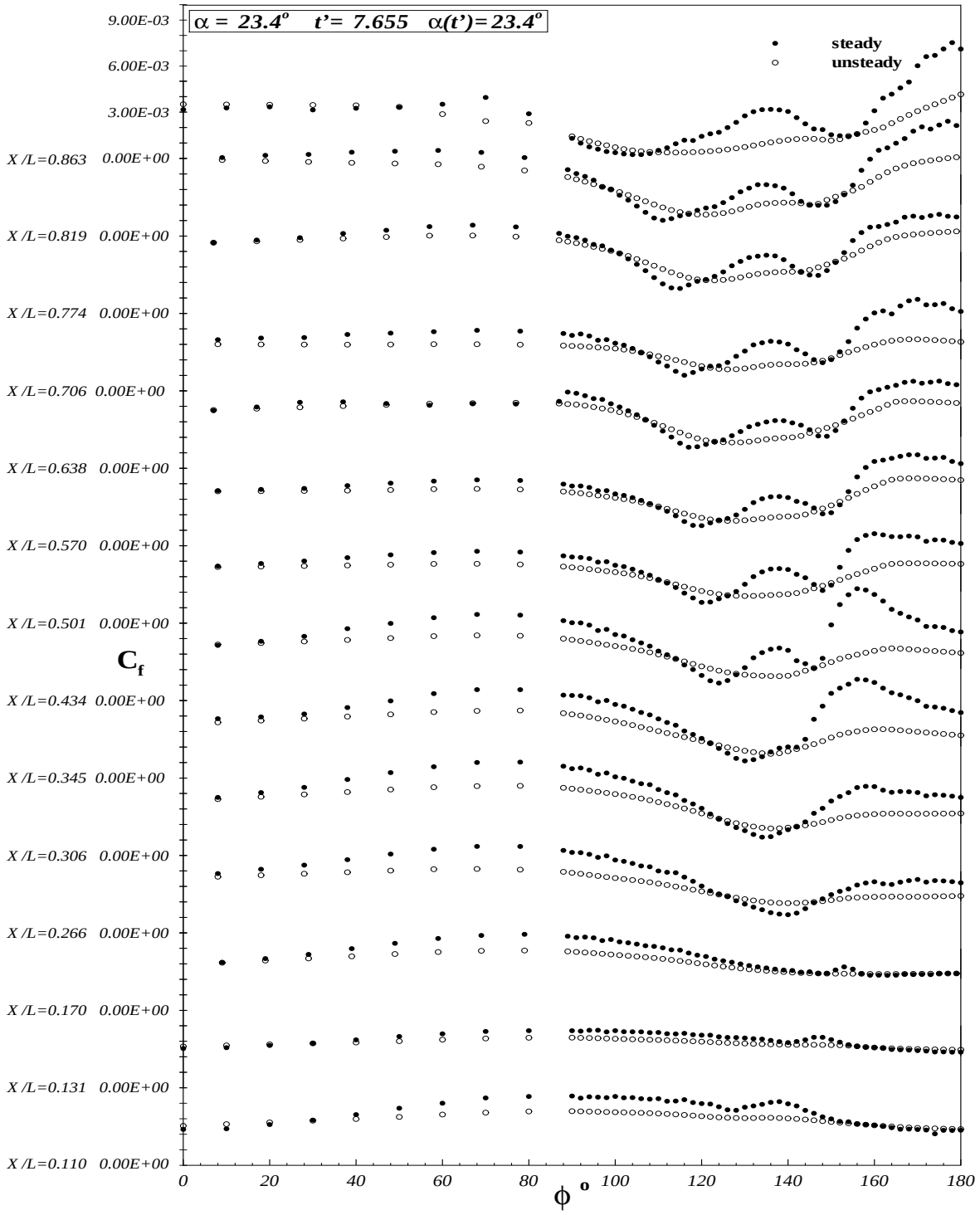


Figure 6.11: Comparison of barebody $C_f$ vs. $\phi$ distribution for steady and unsteady data at all $x/L$ locations. $\alpha = 23.4\,^\circ$, $t' = 7.655$, $\alpha(t') = 23.4\,^\circ$.

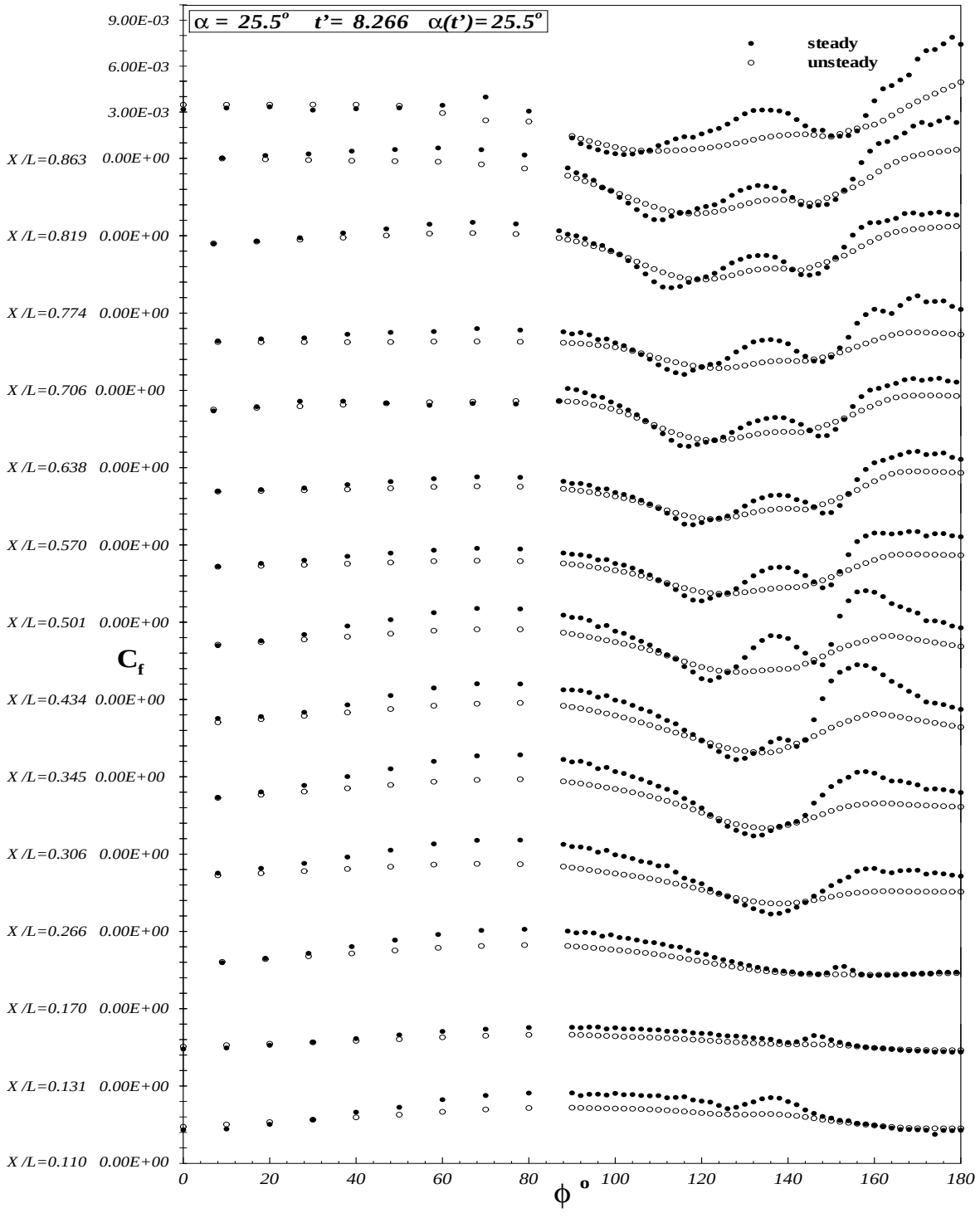


Figure 6.12: Comparison of barebody $C_f$ vs. $\phi$ distribution for steady and unsteady data at all $x/L$ locations. $\alpha = 25.5\,^\circ$, $t' = 8.175$, $\alpha(t') = 25.5\,^\circ$.

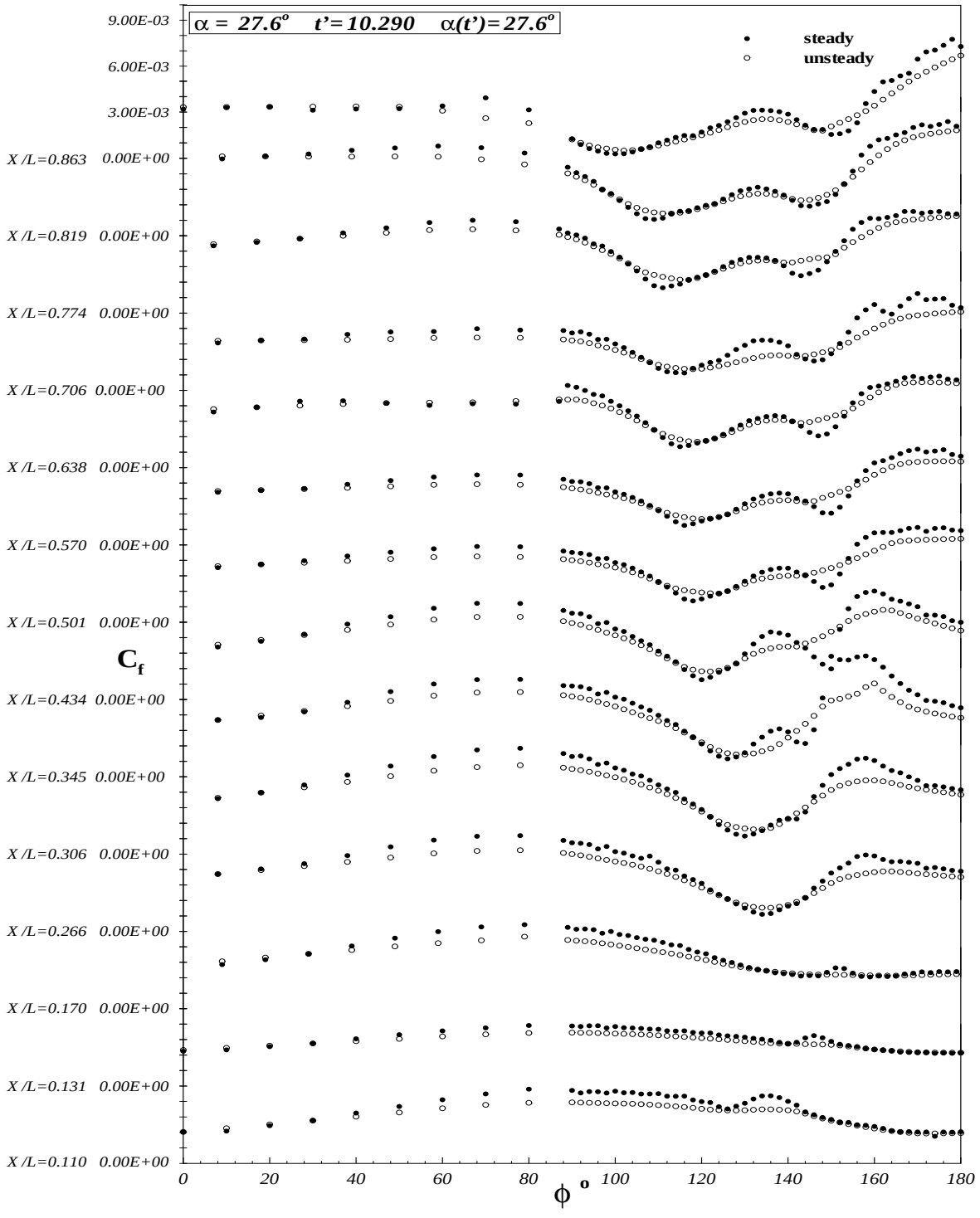


Figure 6.13: Comparison of barebody $C_f$ vs. $\phi$ distribution for steady and unsteady data at all $x/L$ locations. $\alpha = 27.6\,^\circ$, $t' = 10.290$, $\alpha(t') = 27.6\,^\circ$.

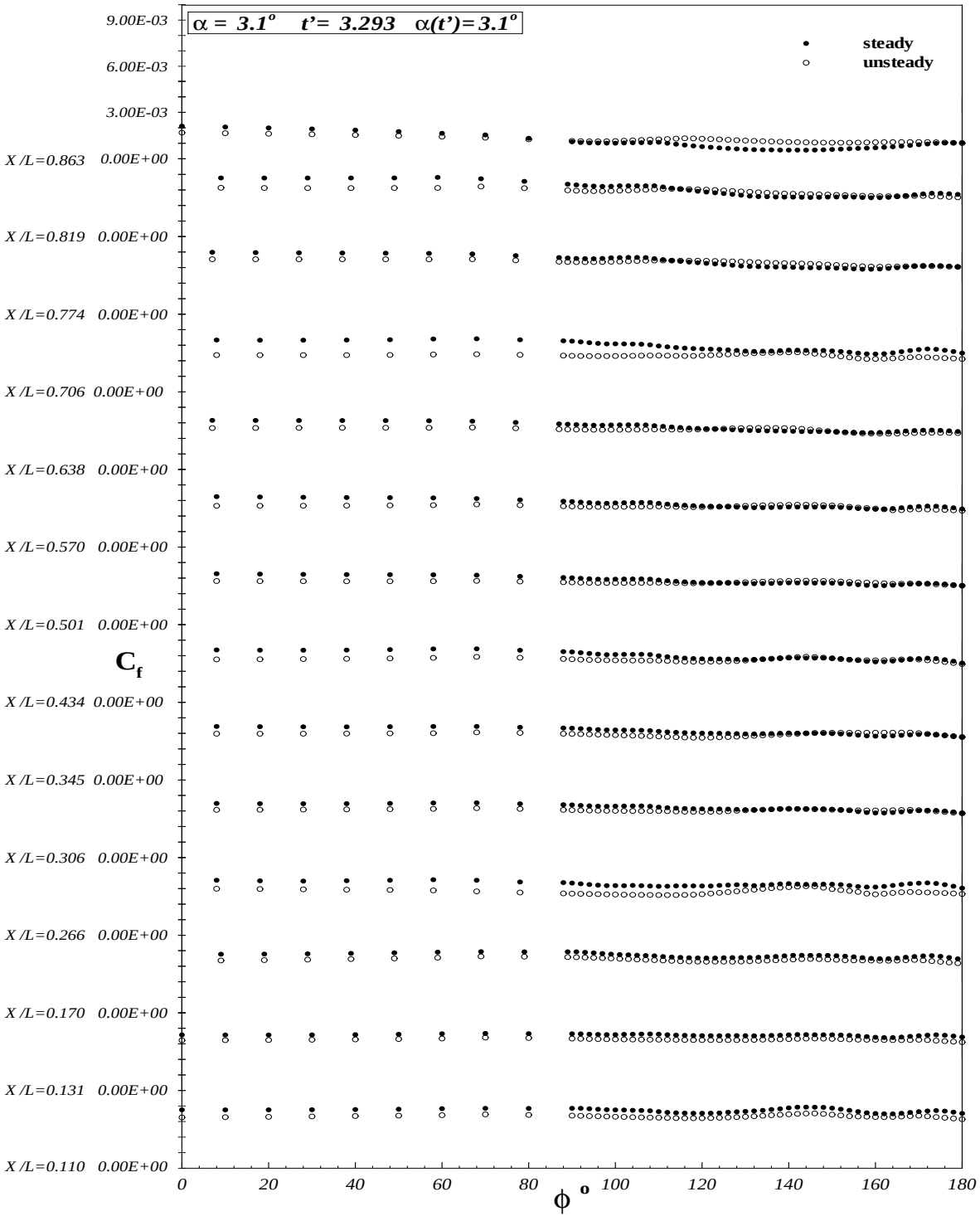


Figure 6.14: Comparison of sail-on-side (region without the sail) $C_f$ vs. $\phi$ distribution for steady and unsteady data at all $x/L$ locations. $\alpha = 3.1\,^\circ$, $t' = 3.293$, $\alpha(t') = 3.1\,^\circ$.

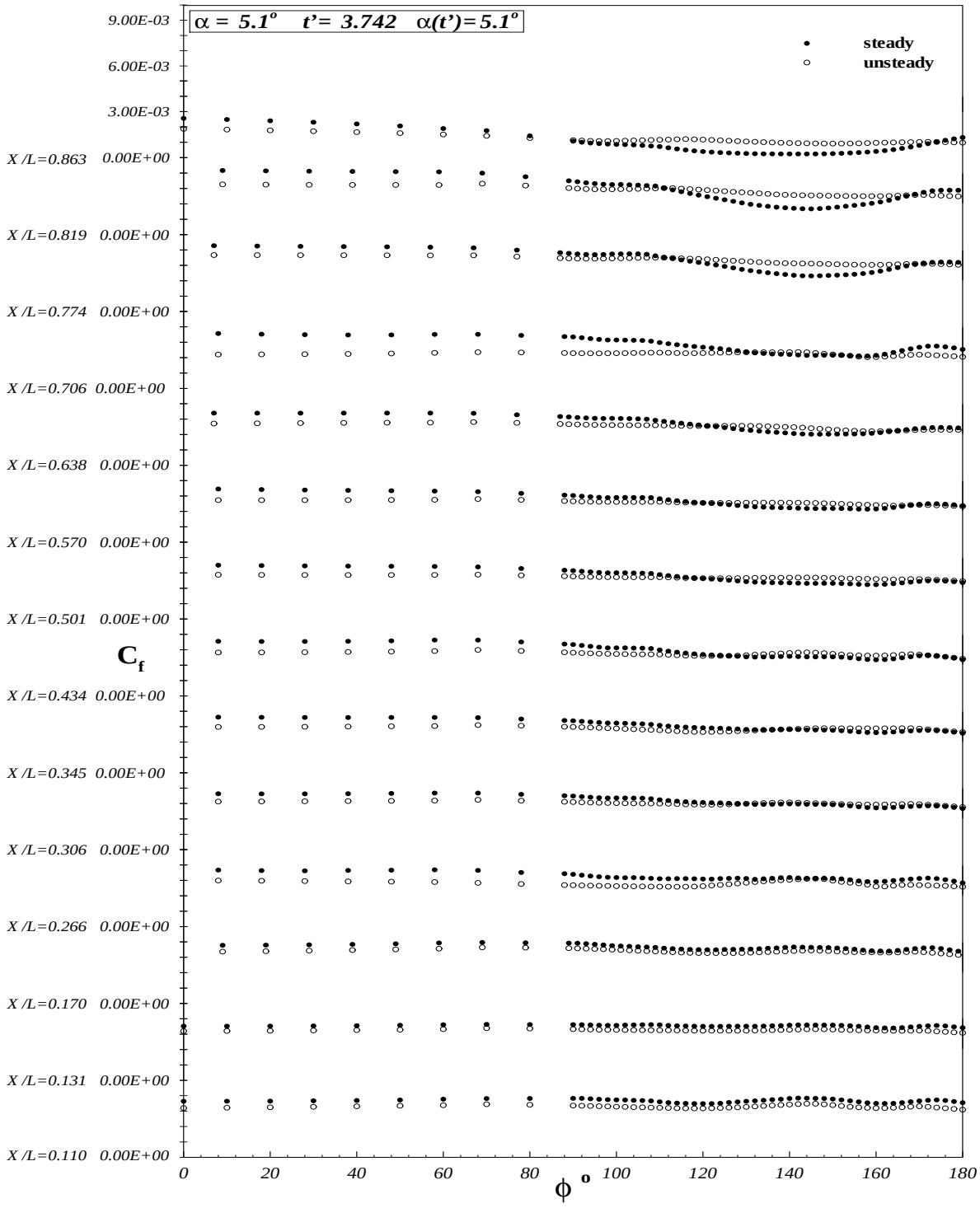


Figure 6.15: Comparison of sail-on-side (region without the sail) $C_f$ vs. $\phi$ distribution for steady and unsteady data at all $x/L$ locations. $\alpha = 5.1\,^\circ$, $t' = 3.742$, $\alpha(t') = 5.1\,^\circ$.

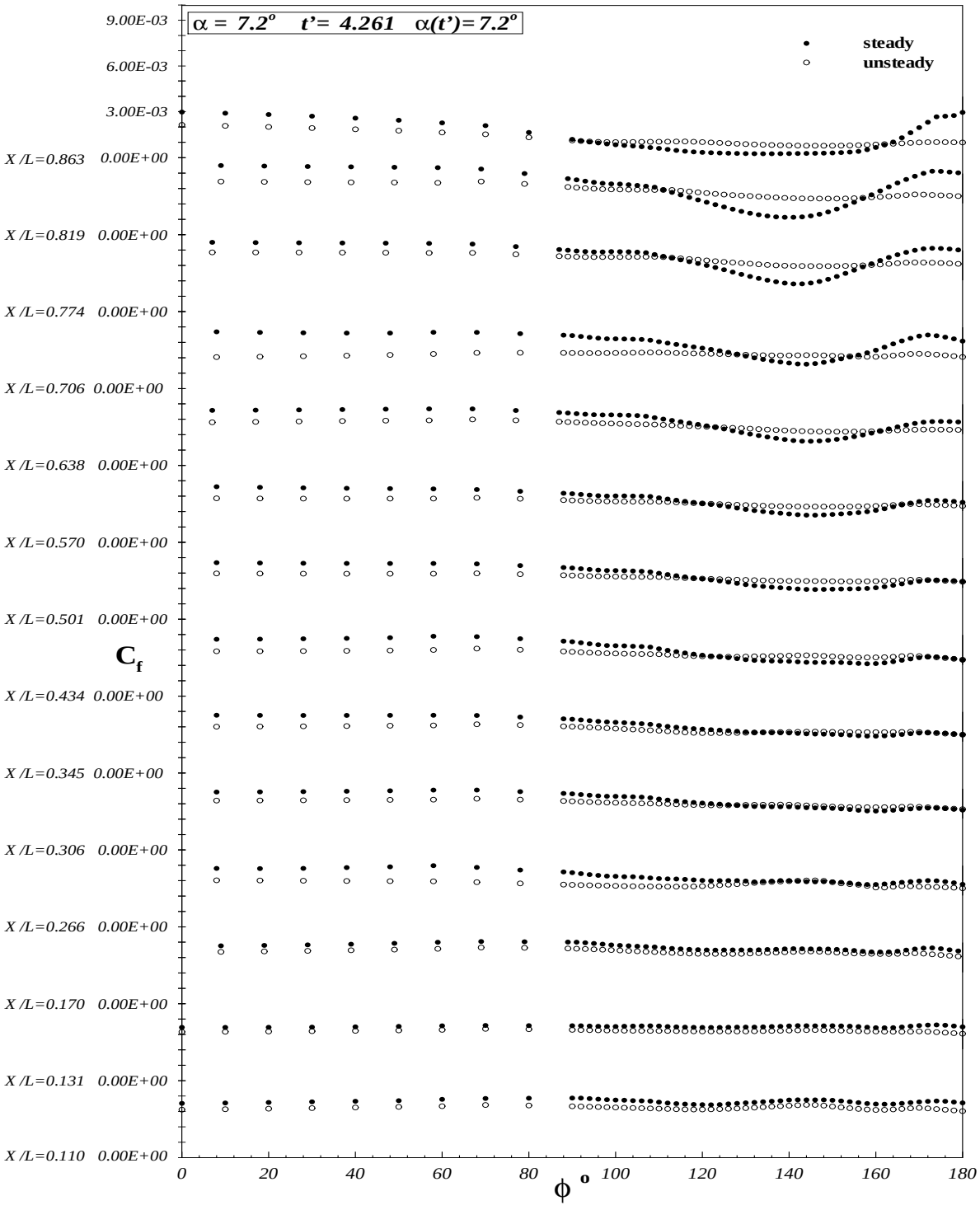


Figure 6.16: Comparison of sail-on-side (region without the sail) $C_f$ vs. $\phi$ distribution for steady and unsteady data at all $x/L$ locations. $\alpha = 7.2\,^\circ$, $t' = 4.261$, $\alpha(t') = 7.2\,^\circ$.

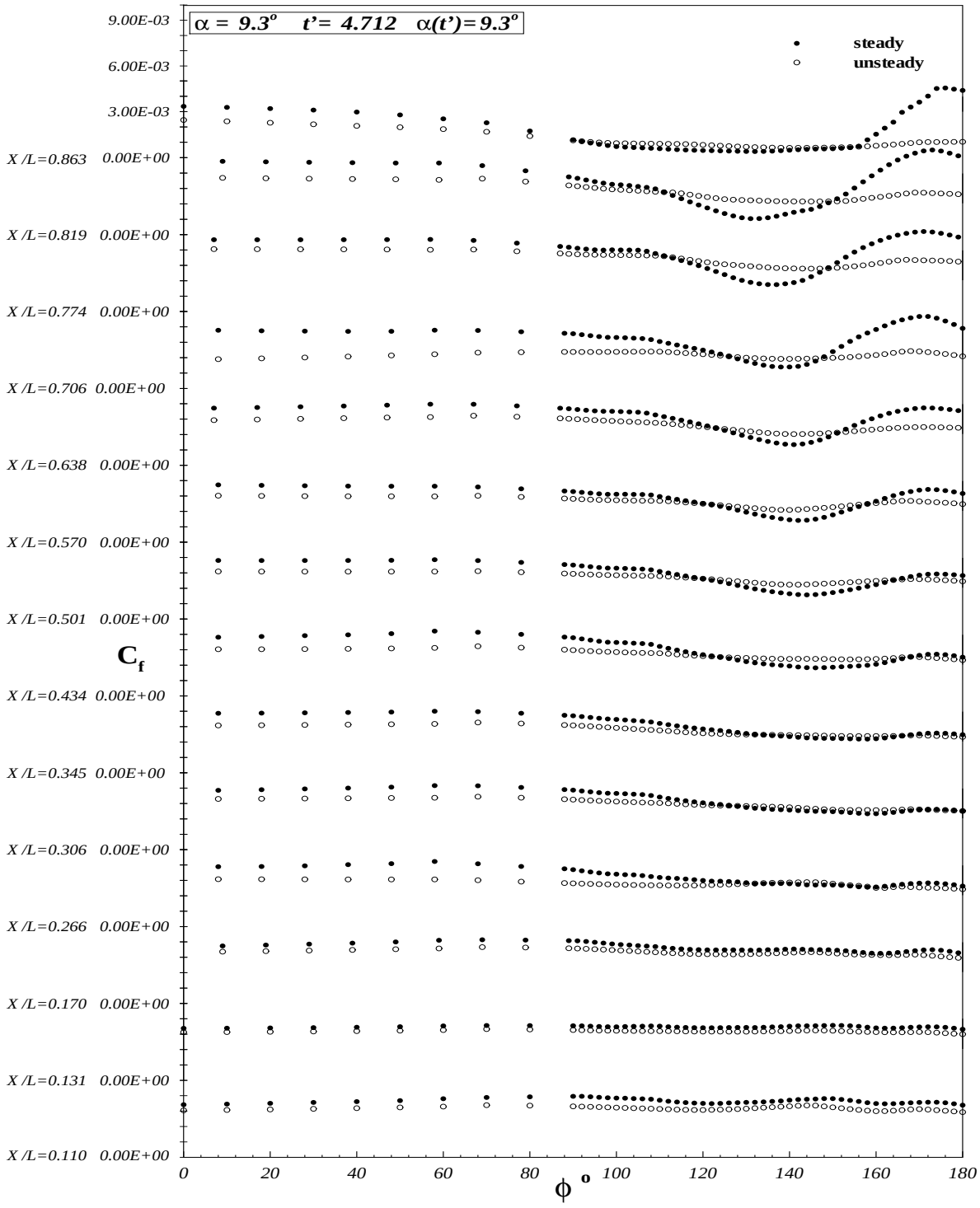


Figure 6.17: Comparison of sail-on-side (region without the sail) $C_f$ vs. $\phi$ distribution for steady and unsteady data at all $x/L$ locations. $\alpha = 9.3\,^\circ$, $t' = 4.7123$, $\alpha(t') = 9.3\,^\circ$.

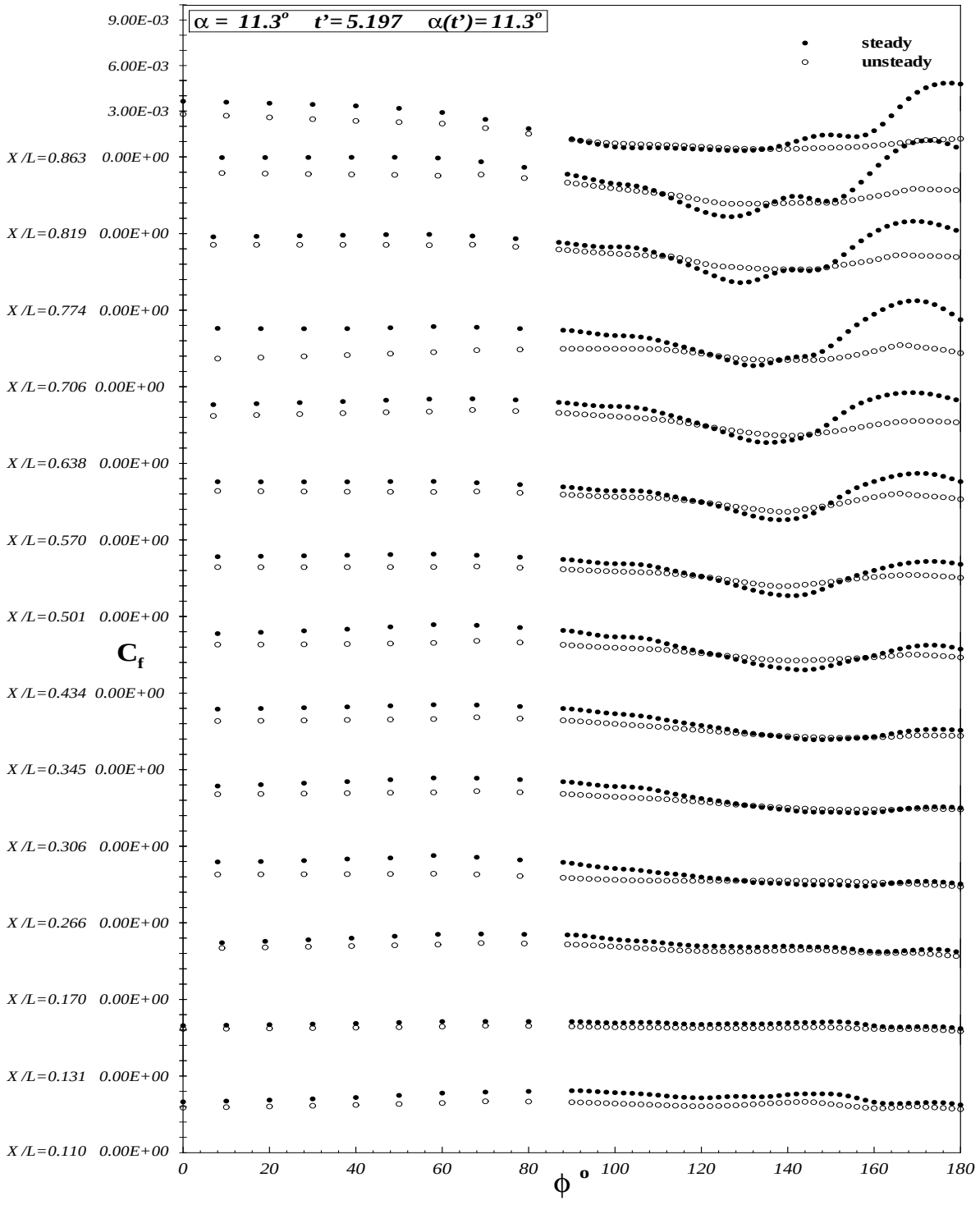


Figure 6.18: Comparison of sail-on-side (region without the sail) $C_f$ vs. $\phi$ distribution for steady and unsteady data at all $x/L$ locations. $\alpha = 11.3\,^\circ$, $t' = 5.197$, $\alpha(t') = 11.3\,^\circ$.

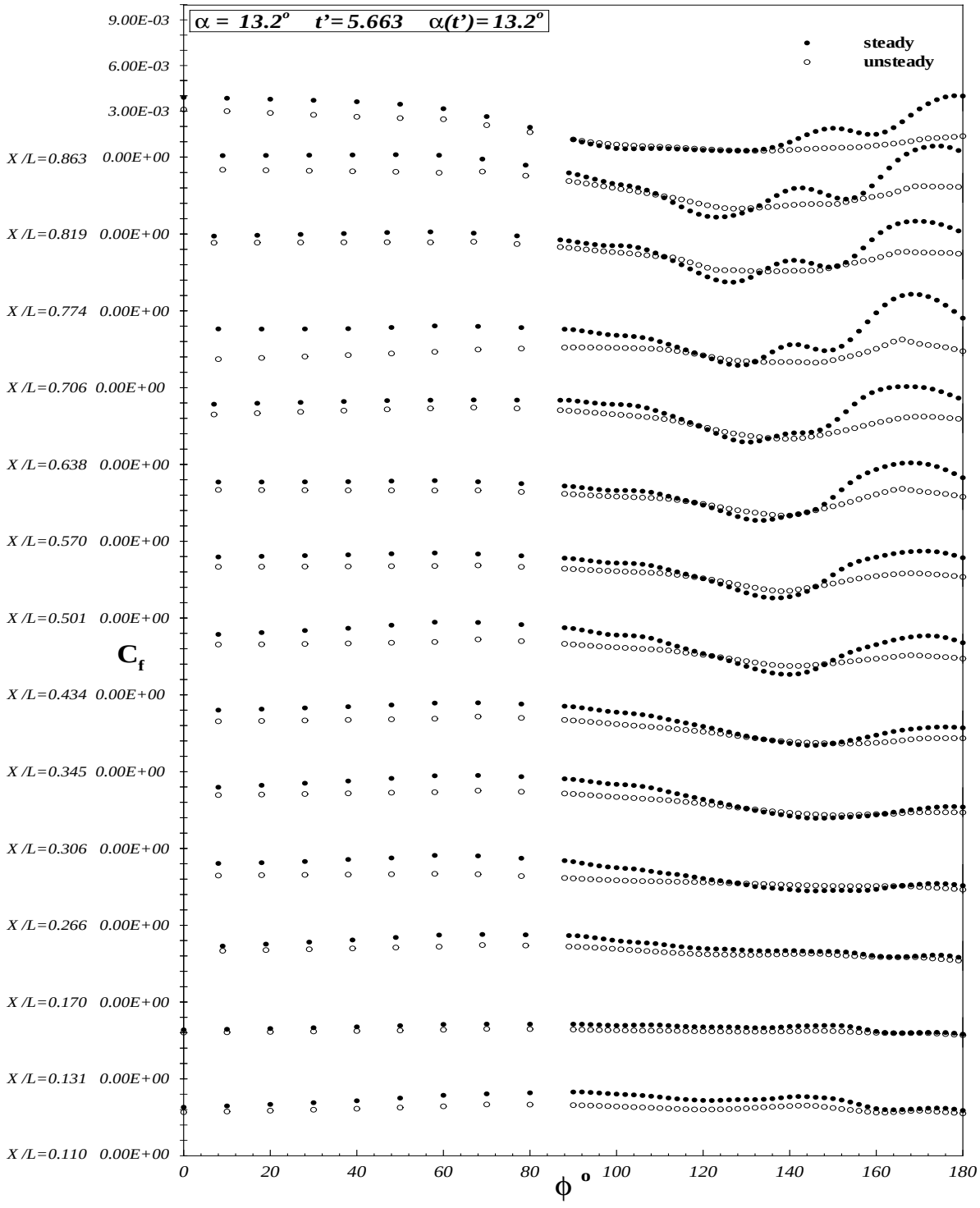


Figure 6.19: Comparison of sail-on-side (region without the sail) $C_f$ vs. $\phi$ distribution for steady and unsteady data at all $x/L$ locations. $\alpha = 13.2\,^\circ$, $t' = 5.663$, $\alpha(t') = 13.2\,^\circ$.

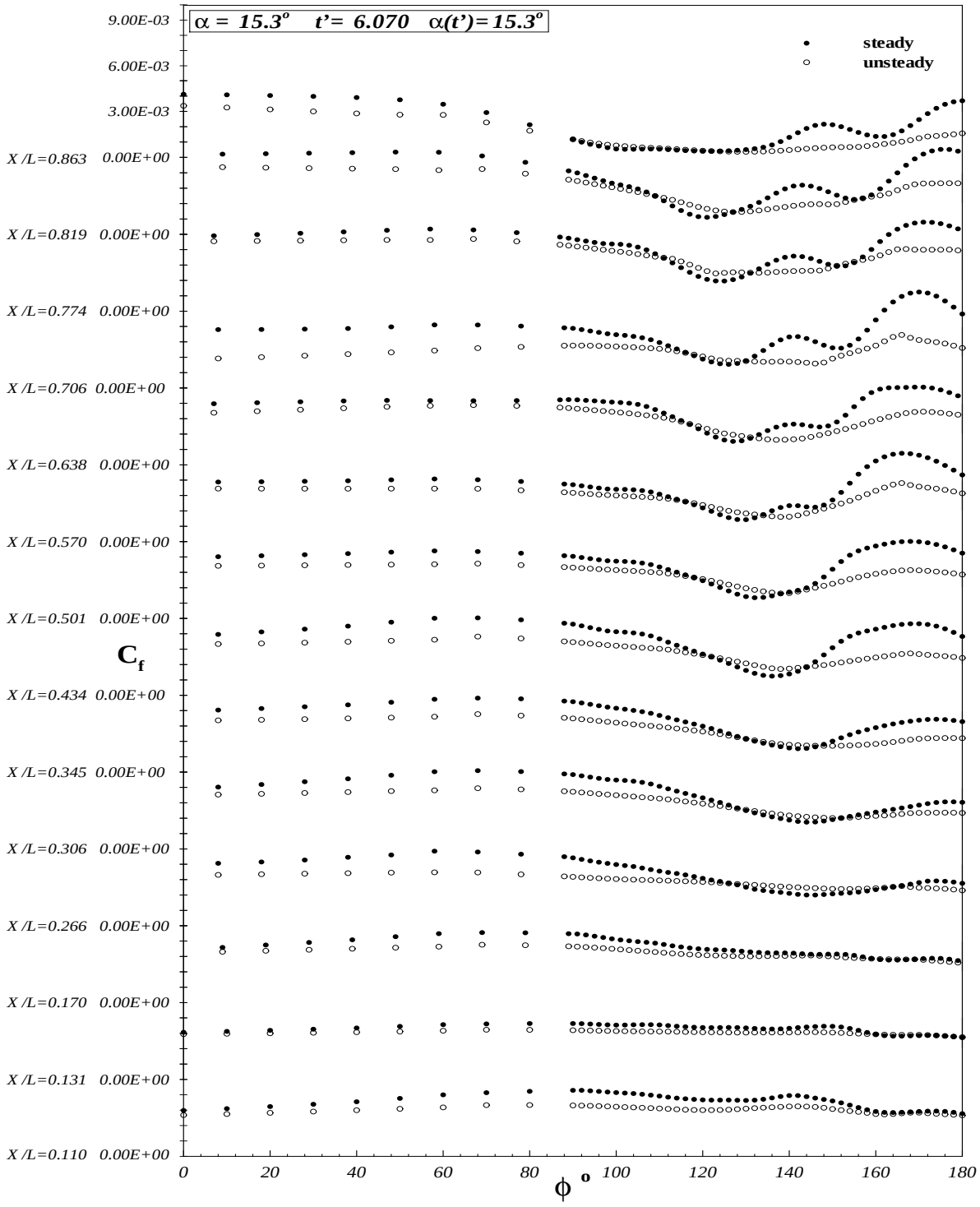


Figure 6.20: Comparison of sail-on-side (region without the sail) $C_f$ vs. $\phi$ distribution for steady and unsteady data at all $x/L$ locations. $\alpha = 15.3\,^\circ$, $t' = 6.070$, $\alpha(t') = 15.3\,^\circ$.

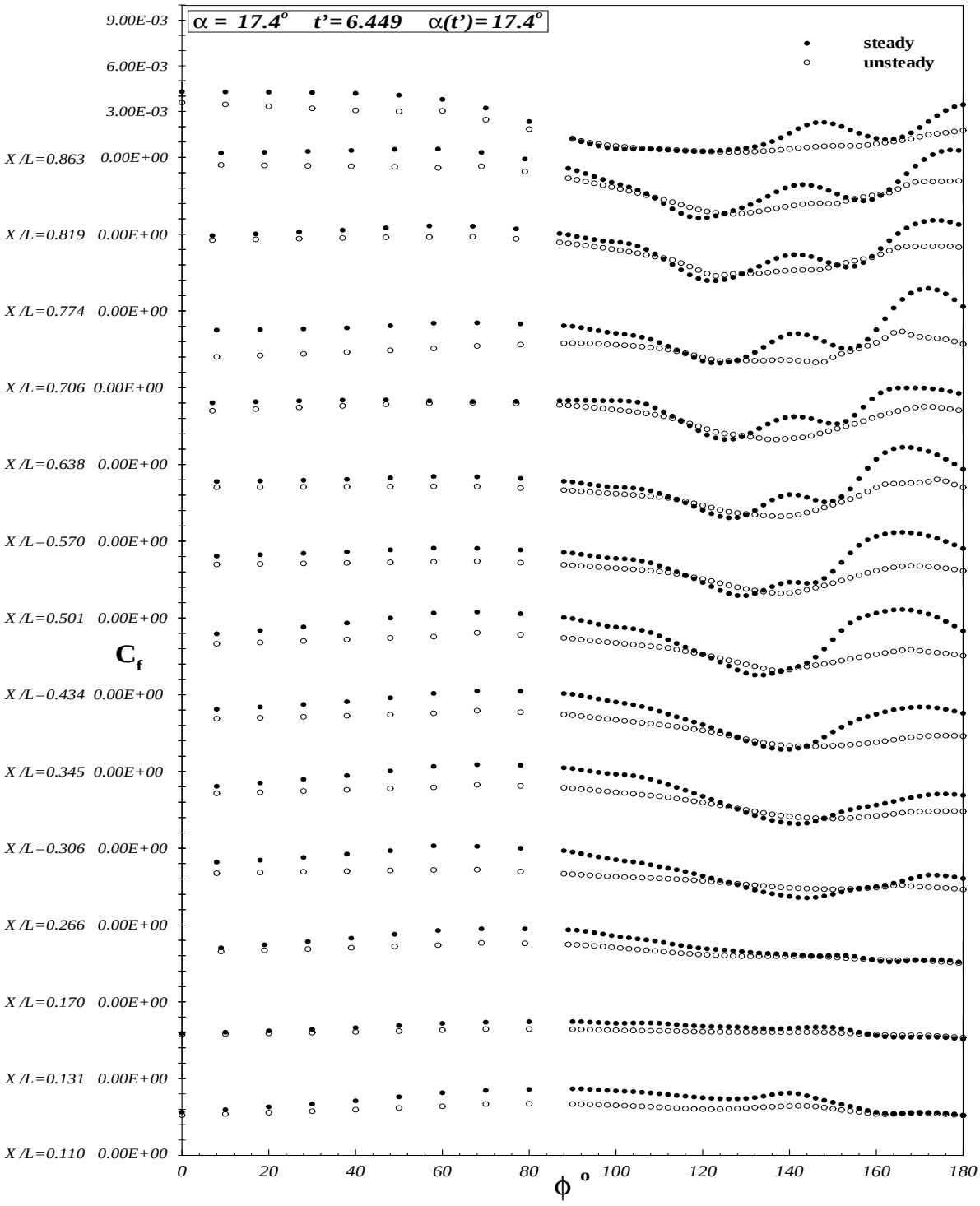


Figure 6.21: Comparison of sail-on-side (region without the sail) $C_f$ vs. $\phi$ distribution for steady and unsteady data at all $x/L$ locations. $\alpha = 17.4\,^\circ$, $t' = 6.449$, $\alpha(t') = 17.4\,^\circ$.

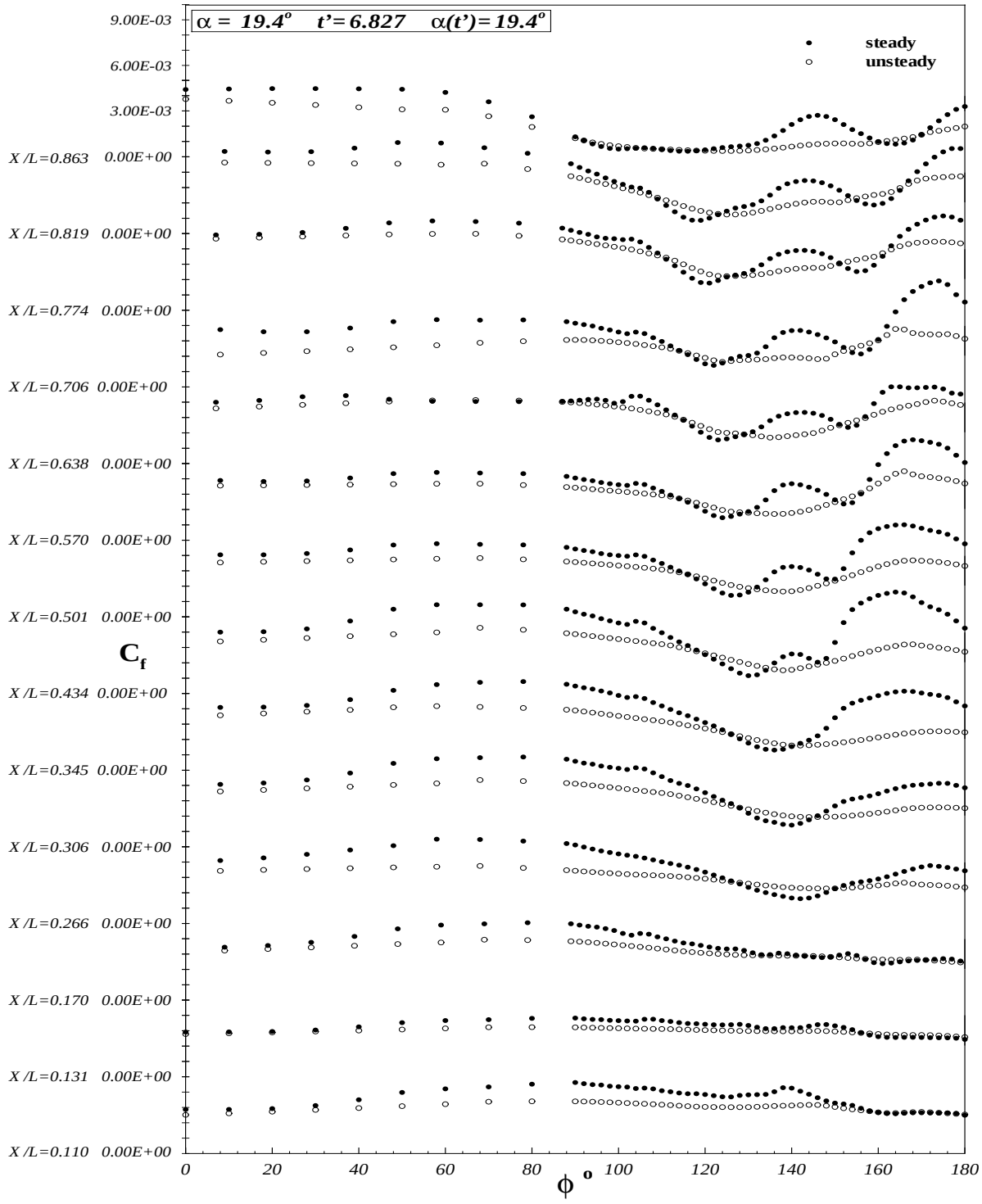


Figure 6.22: Comparison of sail-on-side (region without the sail) $C_f$ vs. $\phi$ distribution for steady and unsteady data at all $x/L$ locations. $\alpha = 19.4\,^\circ$, $t' = 6.827$, $\alpha(t') = 19.4\,^\circ$.

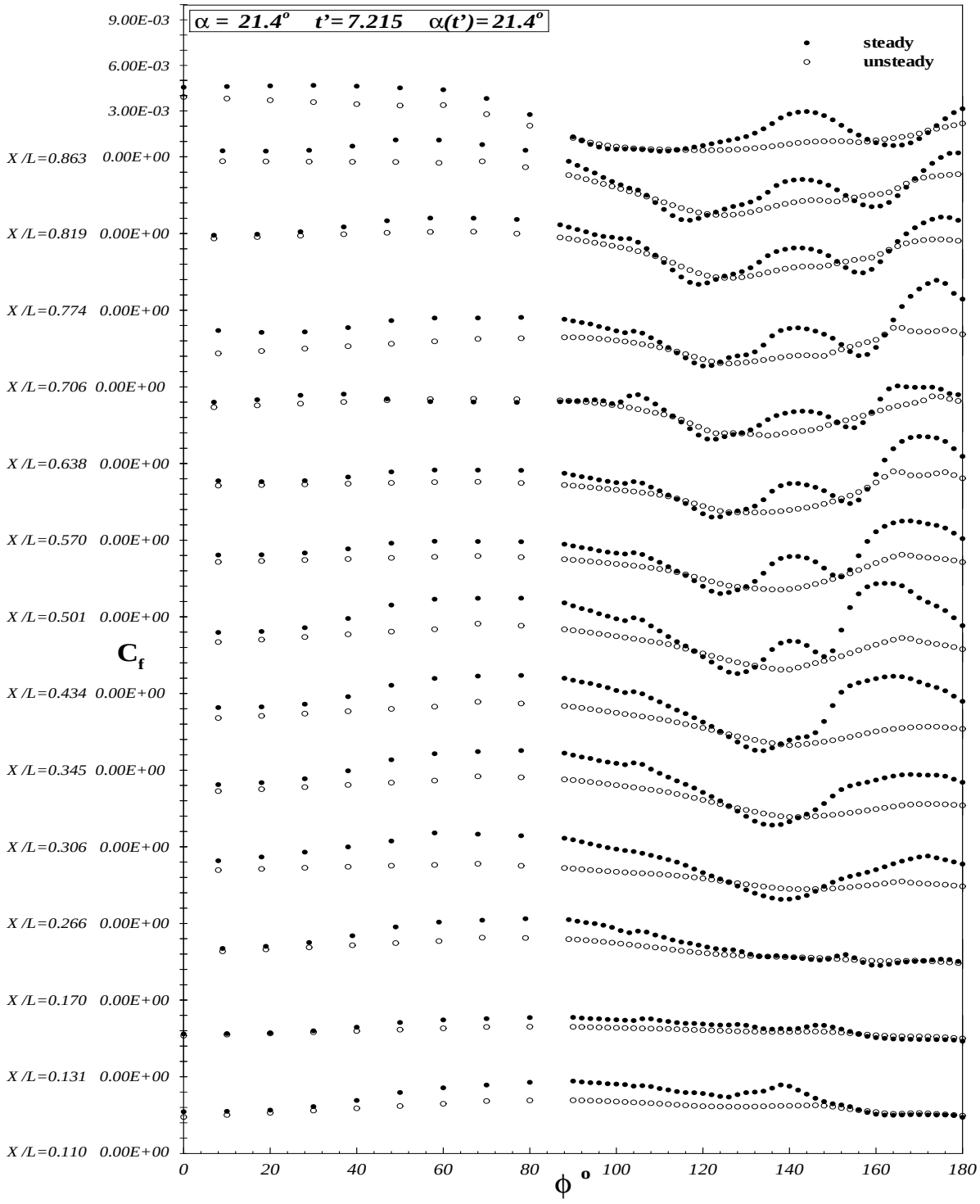


Figure 6.23: Comparison of sail-on-side (region without the sail) $C_f$ vs. $\phi$ distribution for steady and unsteady data at all $x/L$ locations. $\alpha = 21.4\,^\circ$, $t' = 7.215$, $\alpha(t') = 21.4\,^\circ$.

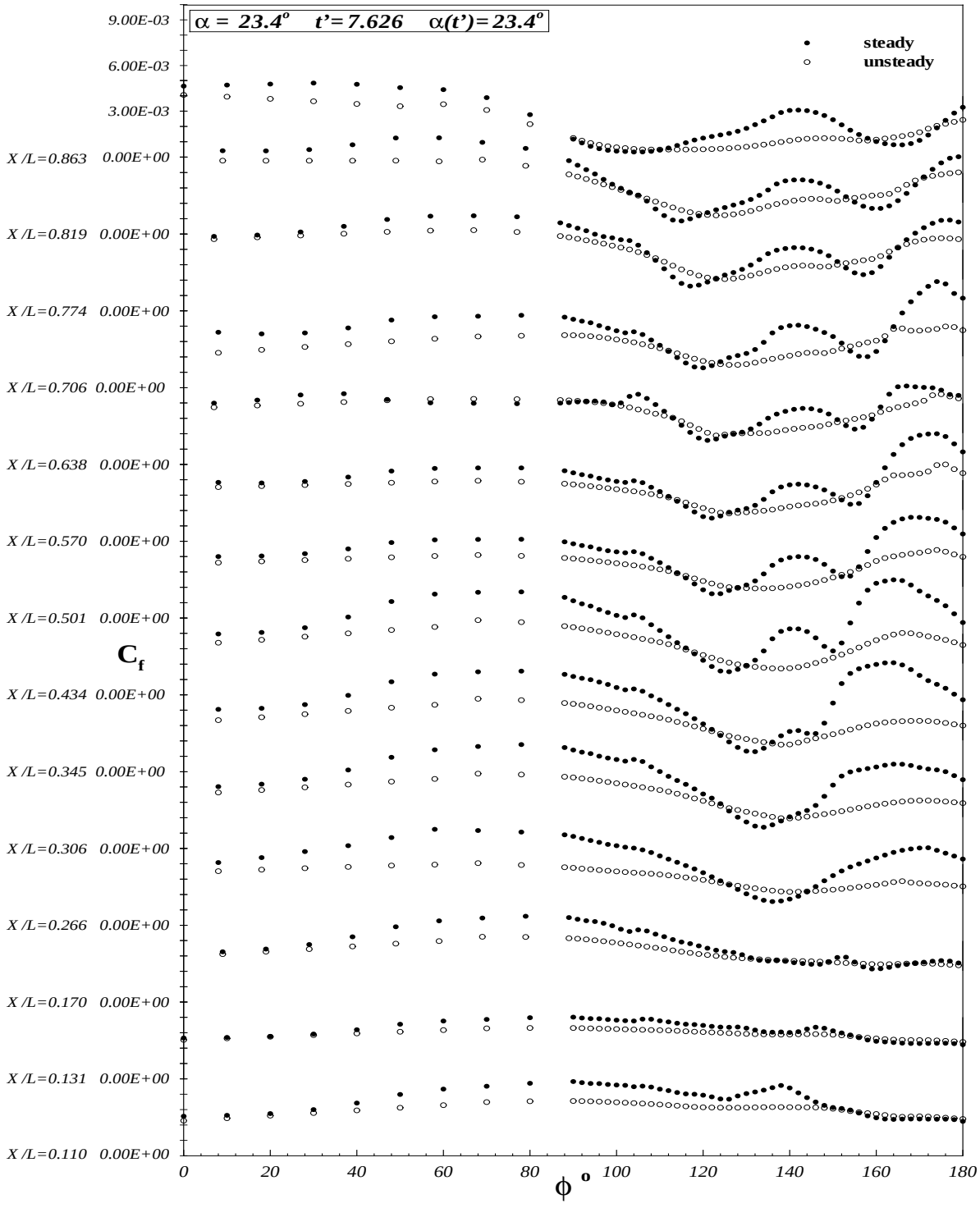


Figure 6.24: Comparison of sail-on-side (region without the sail) $C_f$ vs. $\phi$ distribution for steady and unsteady data at all $x/L$ locations. $\alpha = 23.4\,^\circ$, $t' = 7.626$, $\alpha(t') = 23.4\,^\circ$.

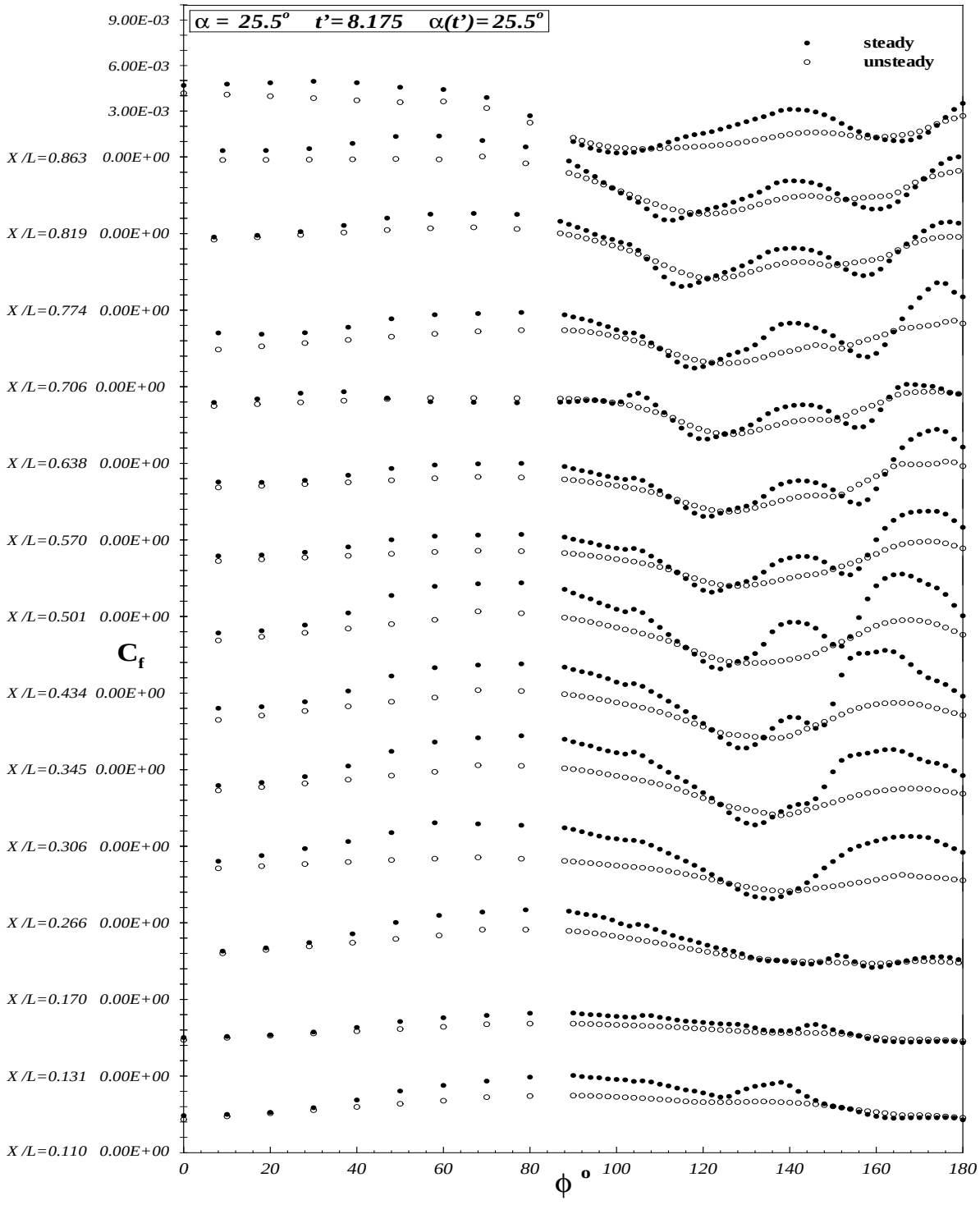


Figure 6.25: Comparison of sail-on-side (region without the sail) $C_f$ vs. $\phi$ distribution for steady and unsteady data at all $x/L$ locations. $\alpha = 25.5\,^\circ$, $t' = 8.266$, $\alpha(t') = 25.5\,^\circ$.

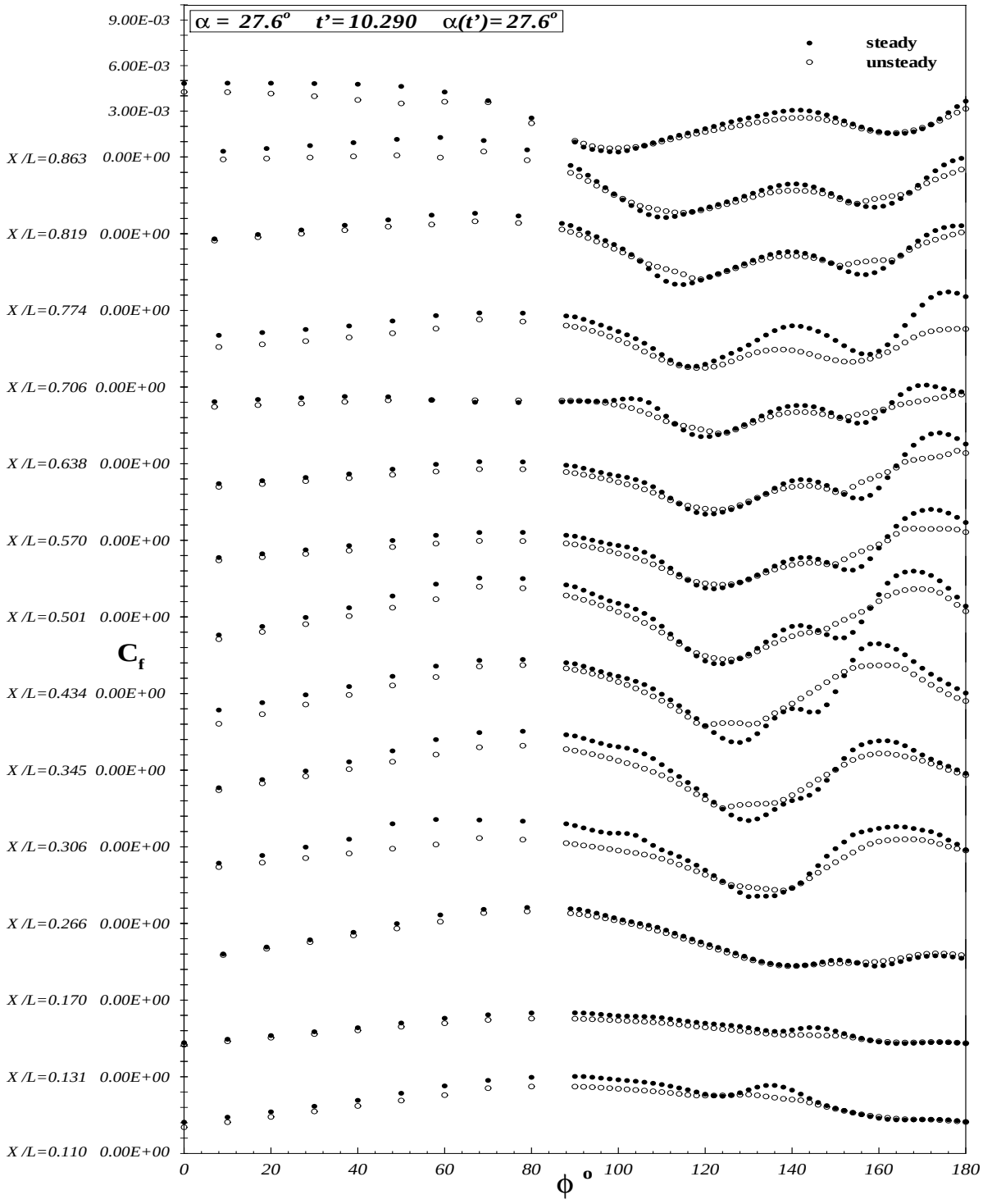


Figure 6.26: Comparison of sail-on-side (region without the sail) $C_f$ vs. $\phi$ distribution for steady and unsteady data at all $x/L$ locations. $\alpha = 27.6\,^\circ$, $t' = 10.290$, $\alpha(t') = 27.6\,^\circ$.

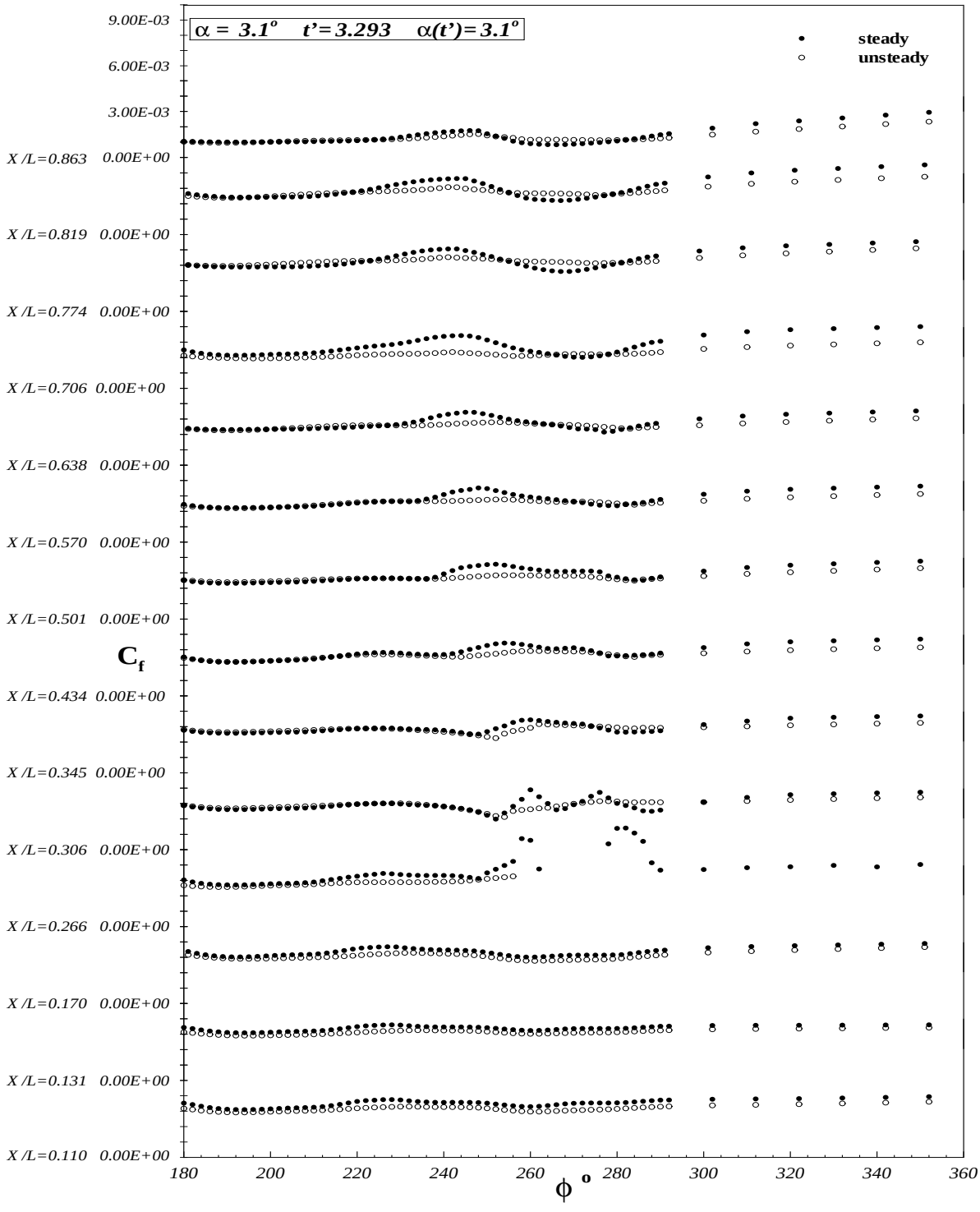


Figure 6.27: Comparison of sail-on-side (region with the sail) $C_f$ vs. $\phi$ distribution for steady and unsteady data at all $x/L$ locations. $\alpha = 3.1\,^\circ$, $t' = 3.293$, $\alpha(t') = 3.1\,^\circ$.

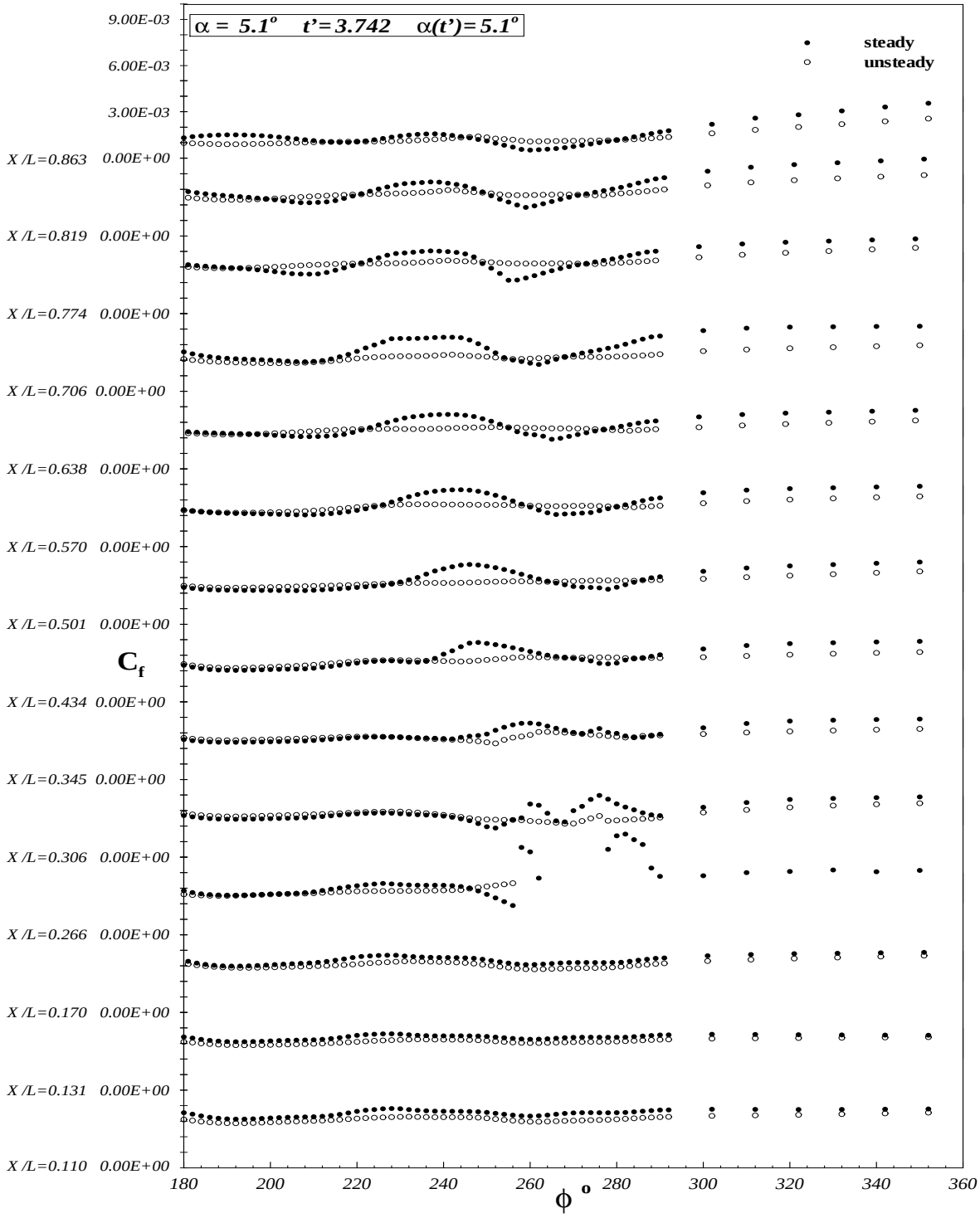


Figure 6.28: Comparison of sail-on-side (region with the sail) $C_f$ vs. $\phi$ distribution for steady and unsteady data at all $x/L$ locations. $\alpha = 5.1\,^\circ$, $t' = 3.742$, $\alpha(t') = 5.1\,^\circ$.

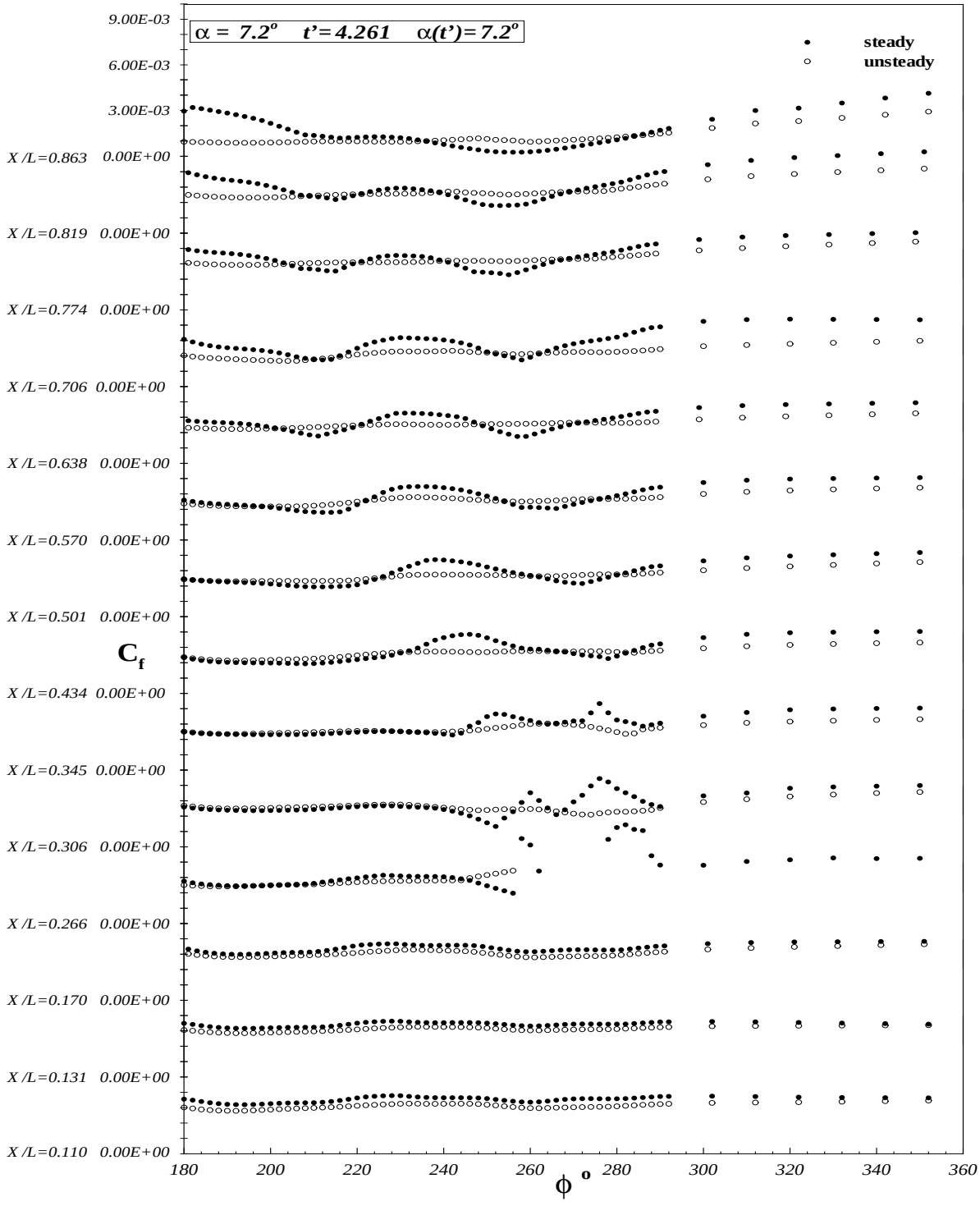


Figure 6.29: Comparison of sail-on-side (region with the sail) $C_f$ vs. $\phi$ distribution for steady and unsteady data at all $x/L$ locations. $\alpha = 7.2\,^\circ$, $t' = 4.261$, $\alpha(t') = 7.2\,^\circ$.

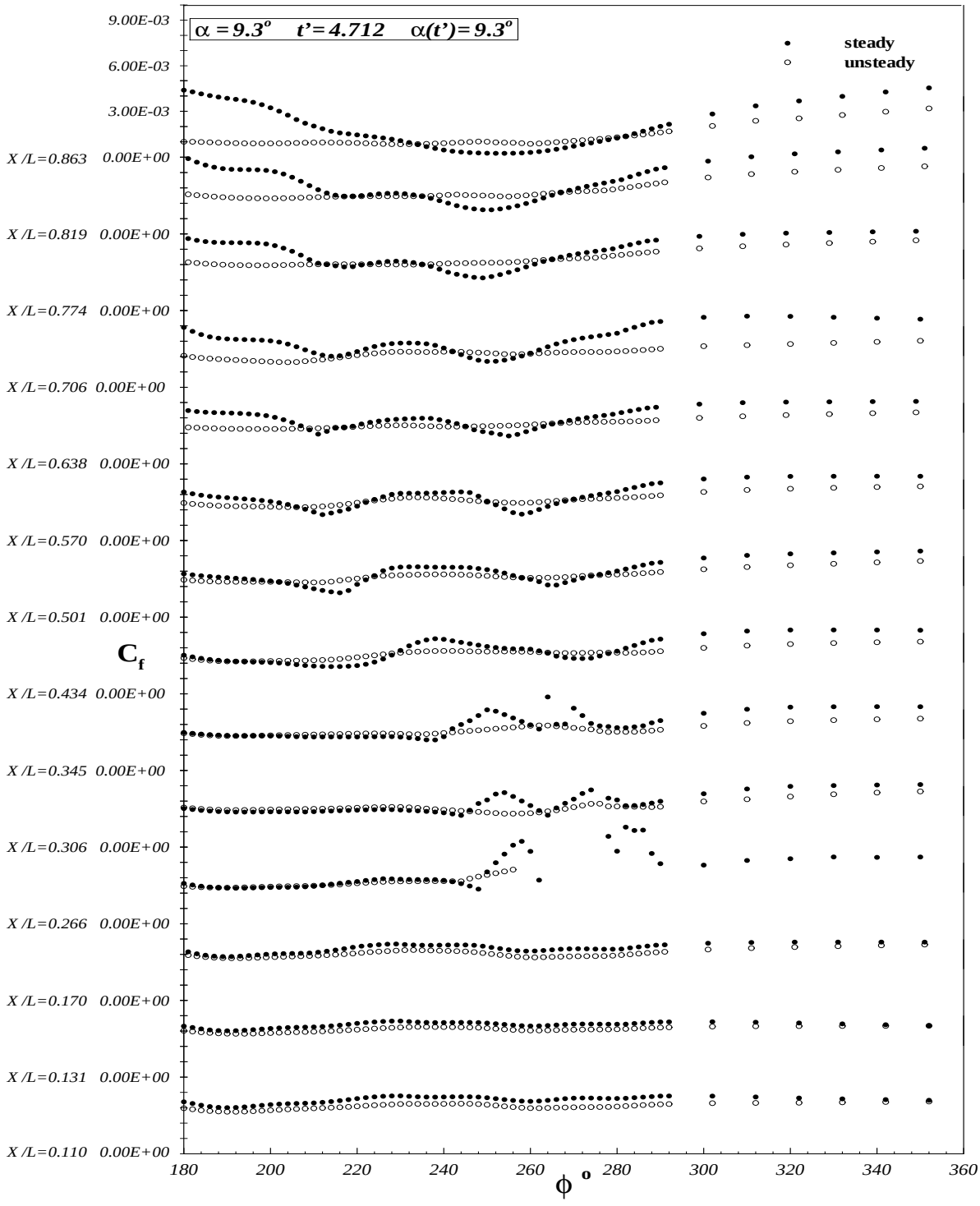


Figure 6.30: Comparison of sail-on-side (region with the sail) $C_f$ vs. $\phi$ distribution for steady and unsteady data at all $x/L$ locations. $\alpha = 9.3\,^\circ$, $t' = 4.7123$, $\alpha(t') = 9.3\,^\circ$.

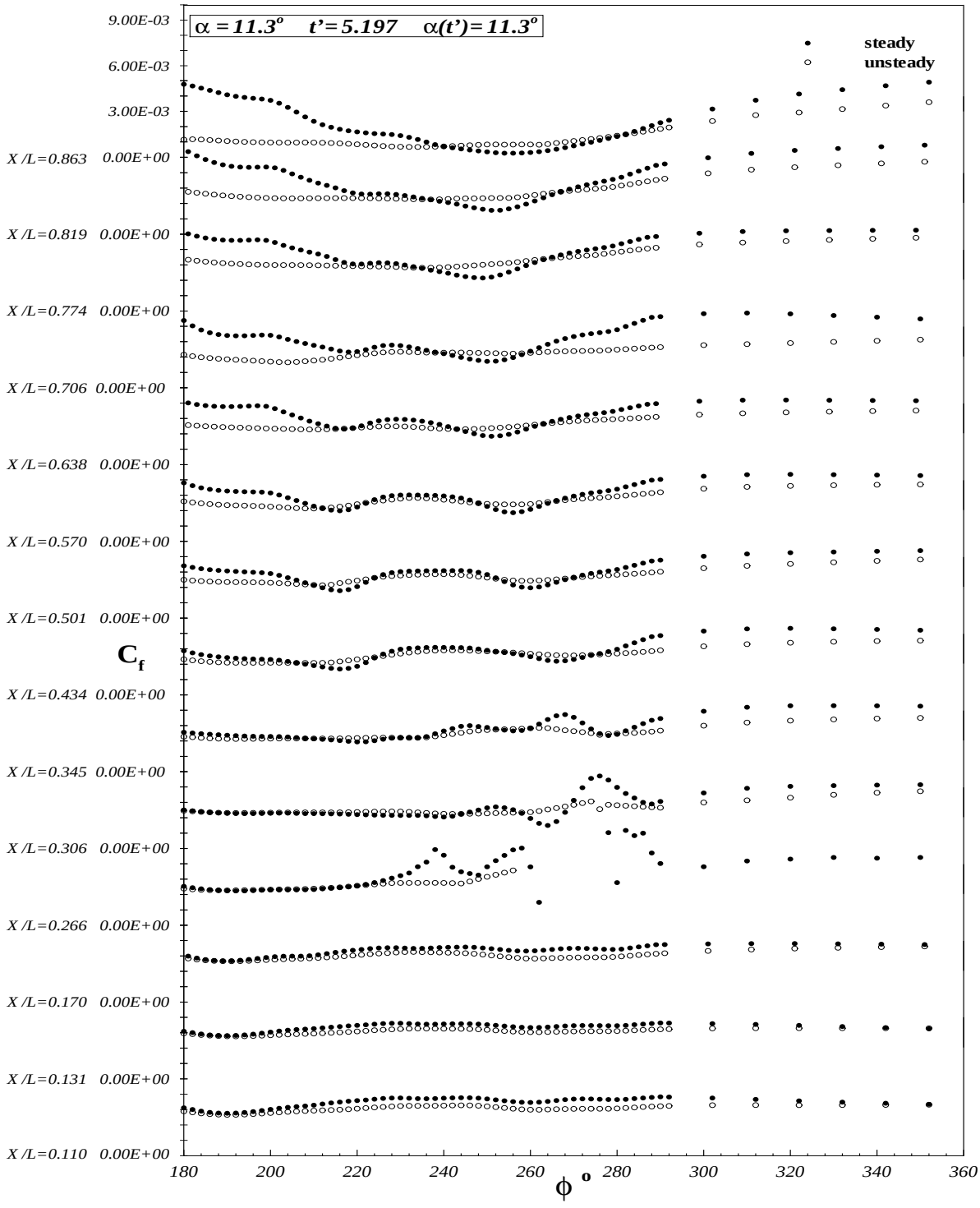


Figure 6.31: Comparison of sail-on-side (region with the sail) $C_f$ vs. $\phi$ distribution for steady and unsteady data at all $x/L$ locations. $\alpha = 11.3\,^\circ$, $t' = 5.197$, $\alpha(t') = 11.3\,^\circ$.

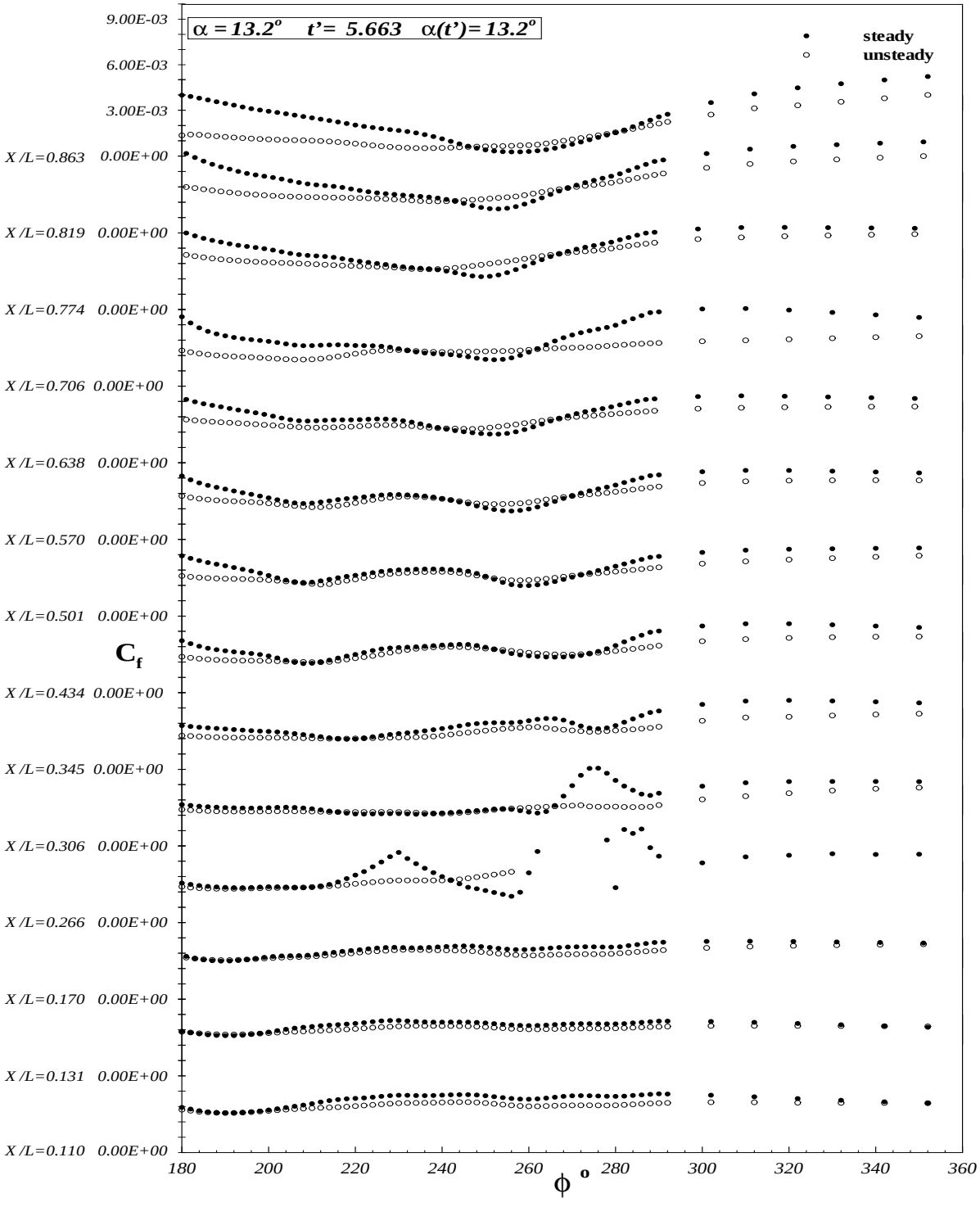


Figure 6.32: Comparison of sail-on-side (region with the sail) $C_f$ vs. $\phi$ distribution for steady and unsteady data at all $x/L$ locations. $\alpha = 13.2\,^\circ$, $t' = 5.663$, $\alpha(t') = 13.2\,^\circ$.

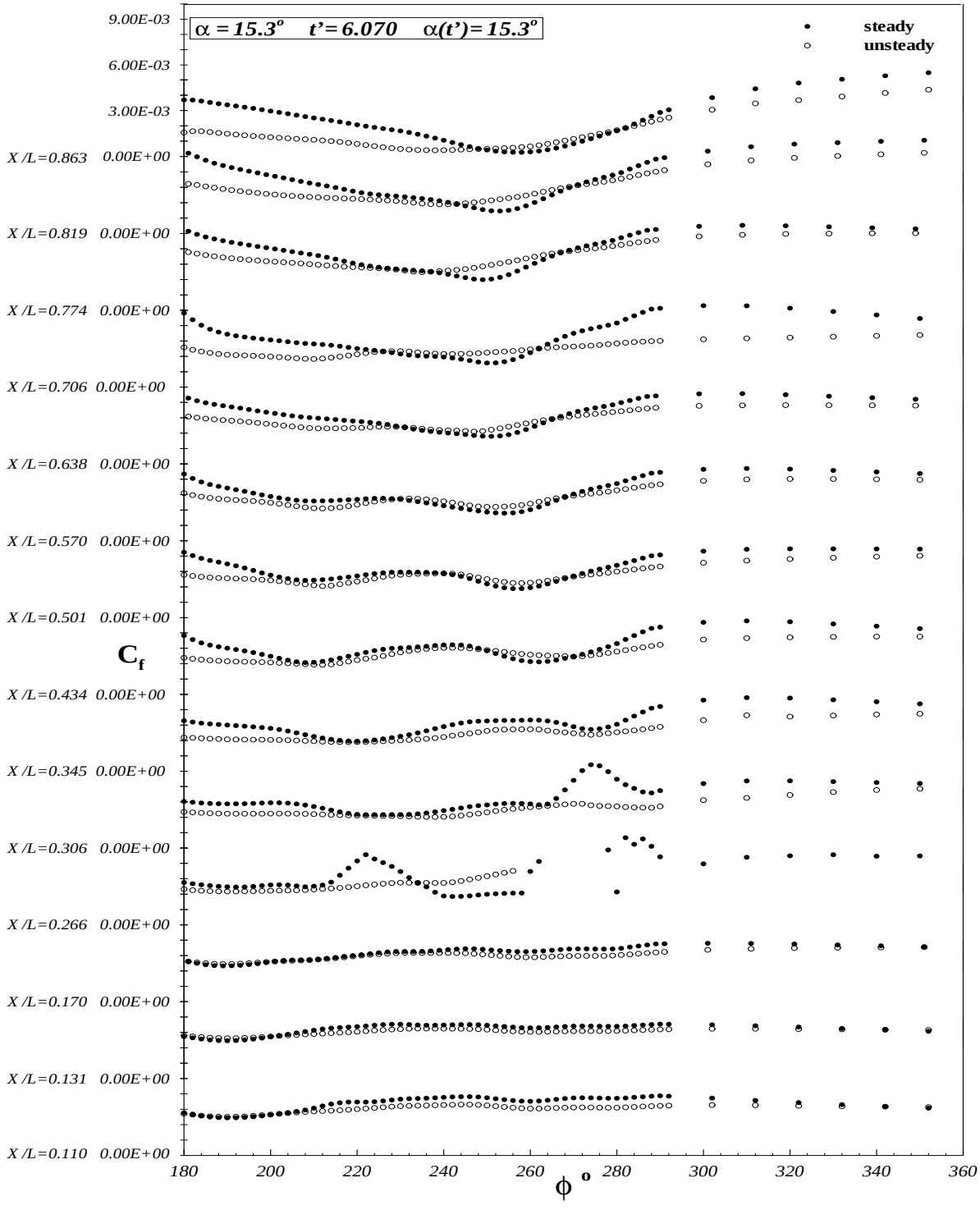


Figure 6.33: Comparison of sail-on-side (region with the sail) $C_f$ vs. $\phi$ distribution for steady and unsteady data at all $x/L$ locations. $\alpha = 15.3\,^\circ$, $t' = 6.070$, $\alpha(t') = 15.3\,^\circ$.

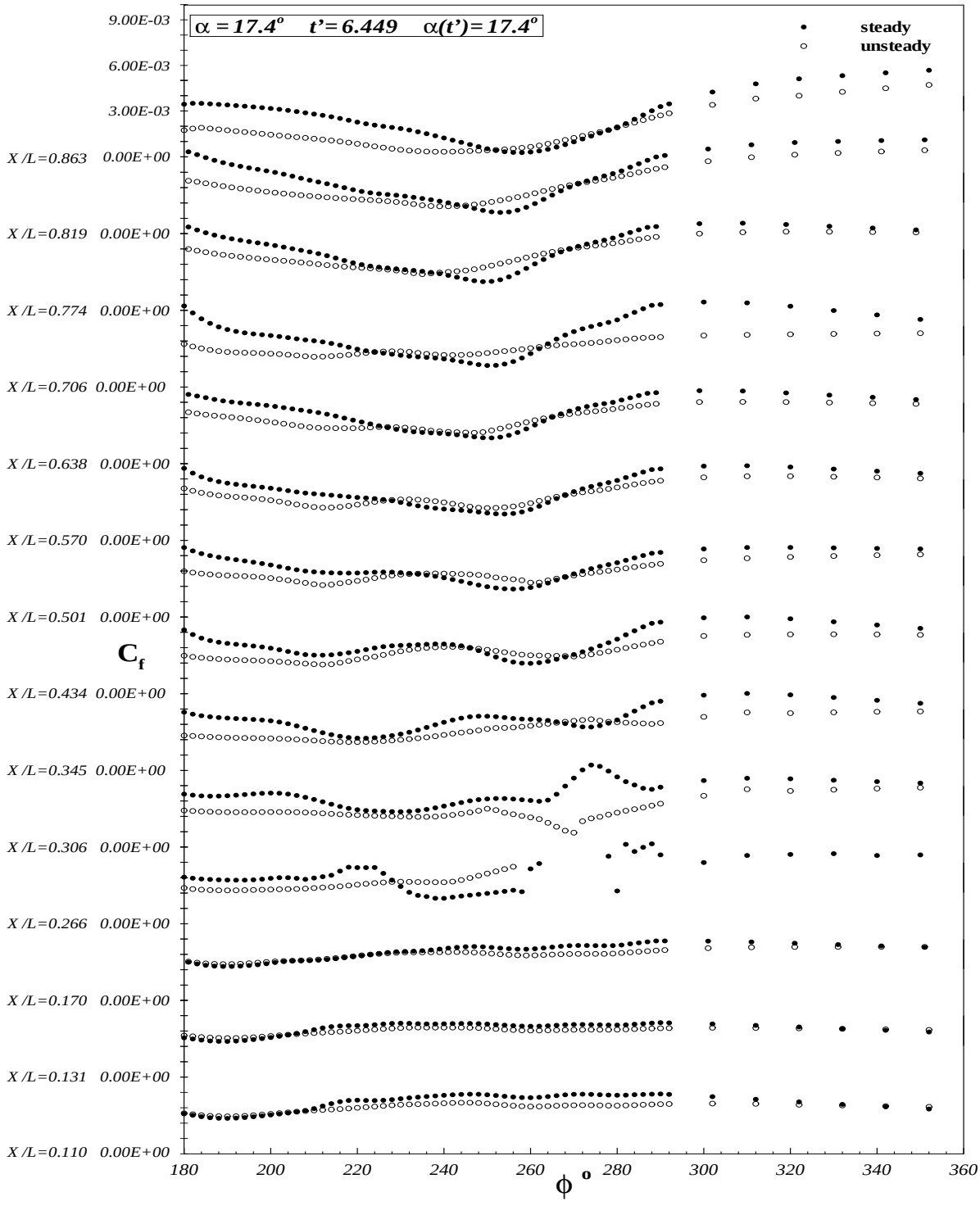


Figure 6.34: Comparison of sail-on-side (region with the sail) $C_f$ vs. $\phi$ distribution for steady and unsteady data at all $x/L$ locations. $\alpha = 17.4\,^\circ$, $t' = 6.449$, $\alpha(t') = 17.4\,^\circ$.

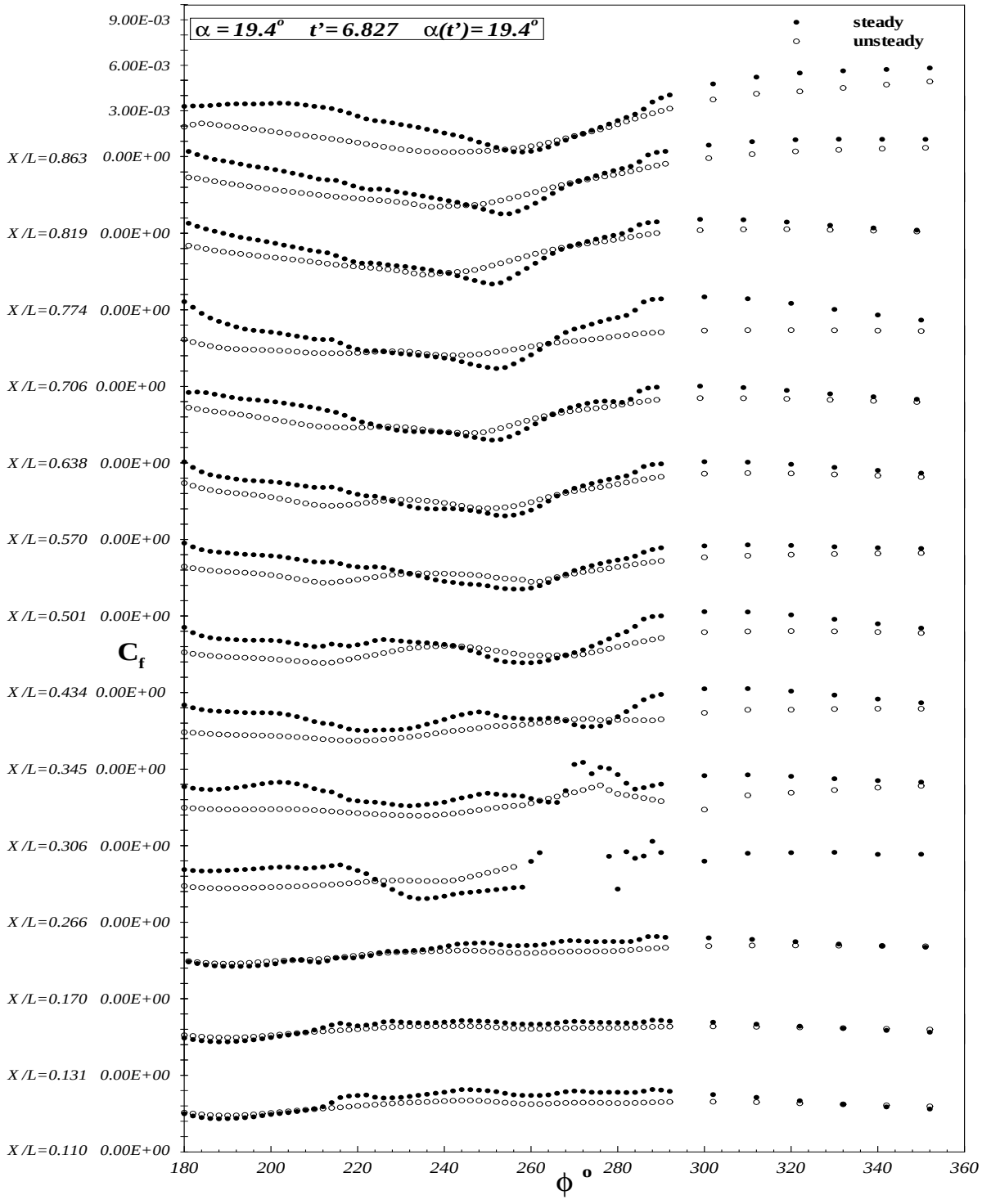


Figure 6.35: Comparison of sail-on-side (region with the sail) $C_f$ vs. $\phi$ distribution for steady and unsteady data at all $x/L$ locations. $\alpha = 19.4\,^\circ$, $t' = 6.827$, $\alpha(t') = 19.4\,^\circ$.

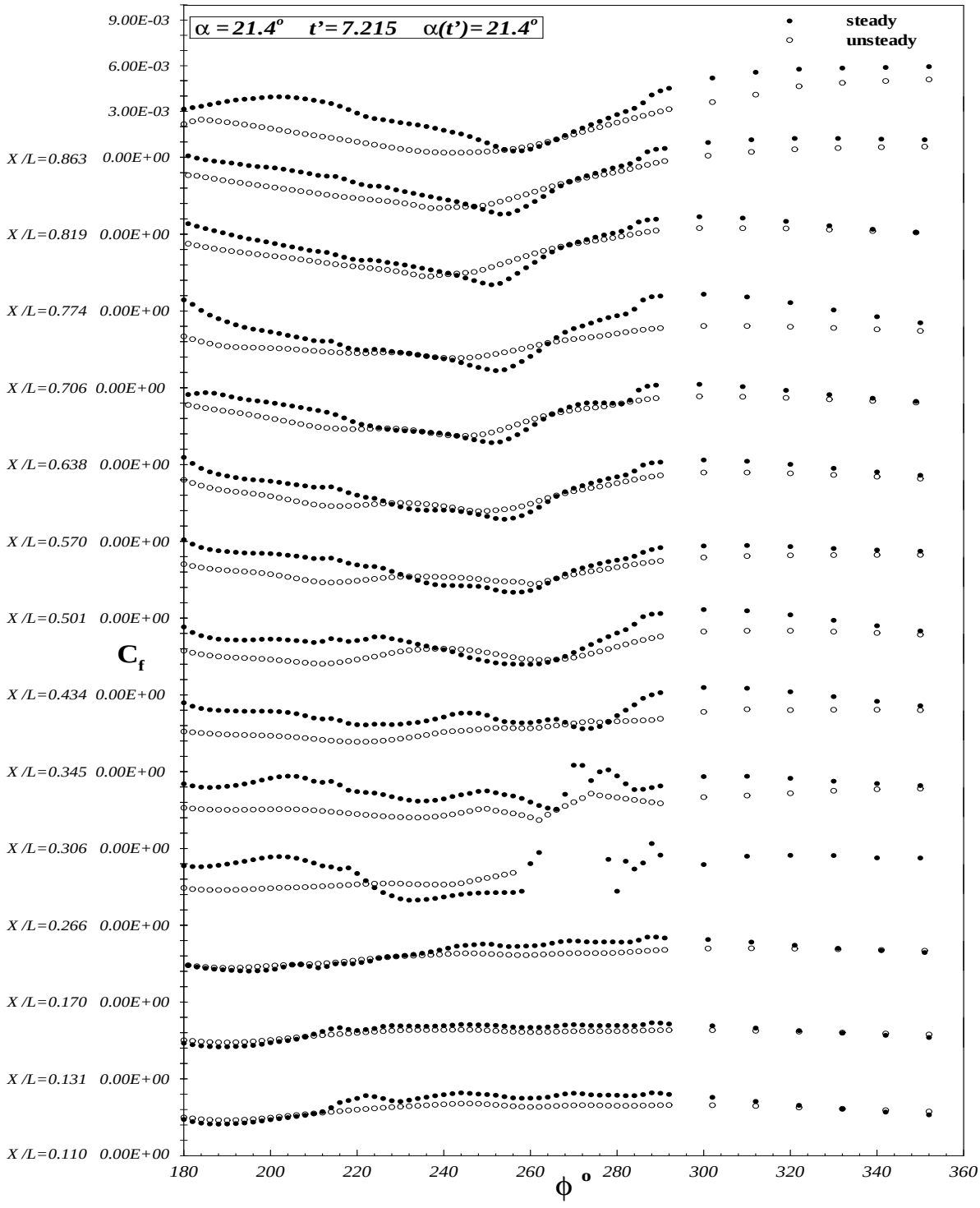


Figure 6.36: Comparison of sail-on-side (region with the sail) $C_f$ vs. $\phi$ distribution for steady and unsteady data at all $x/L$ locations. $\alpha = 21.4\,^\circ$, $t' = 7.215$, $\alpha(t') = 21.4\,^\circ$.

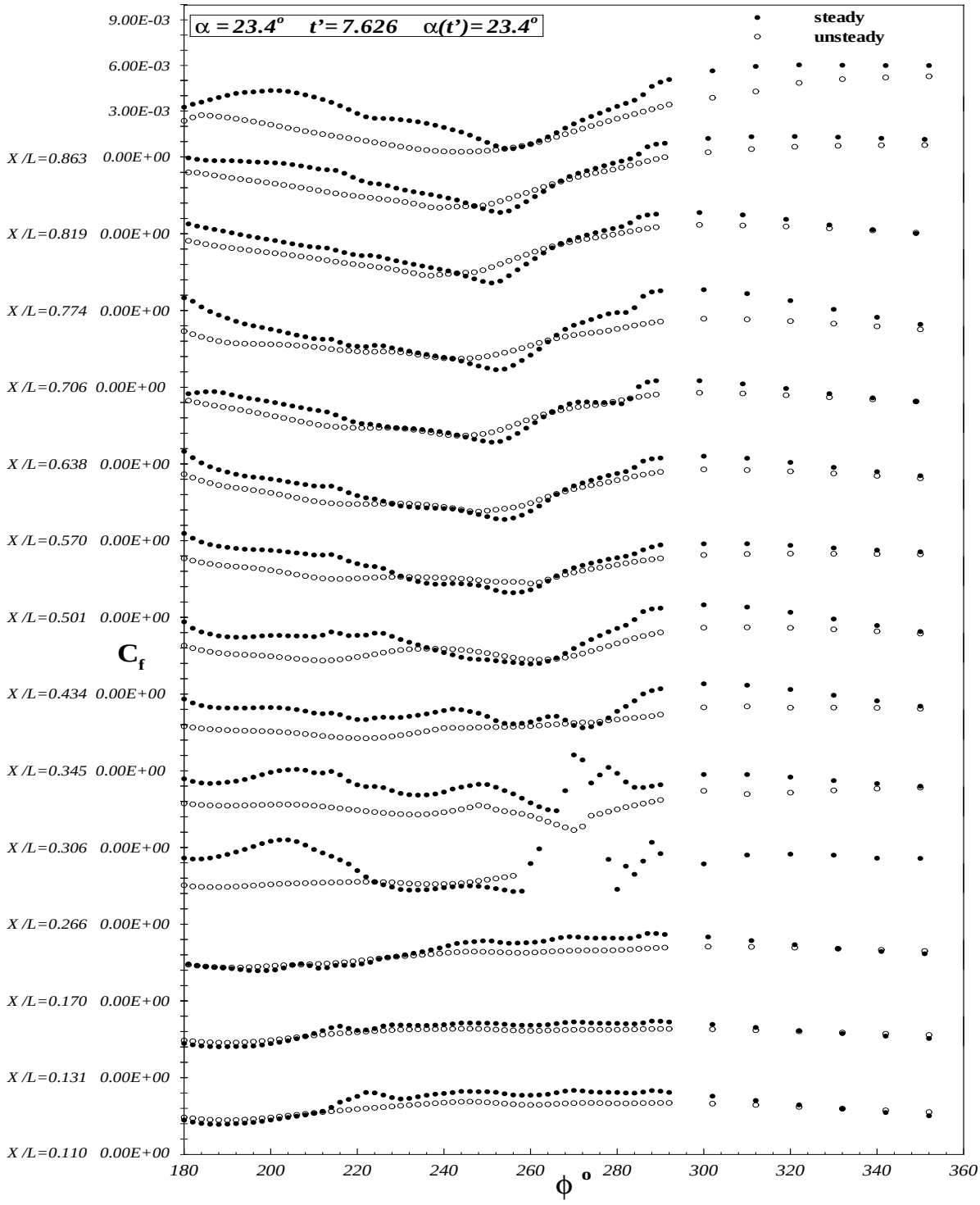


Figure 6.37: Comparison of sail-on-side (region with the sail) $C_f$ vs. $\phi$ distribution for steady and unsteady data at all $x/L$ locations. $\alpha = 23.4\,^\circ$, $t' = 7.626$, $\alpha(t') = 23.4\,^\circ$.

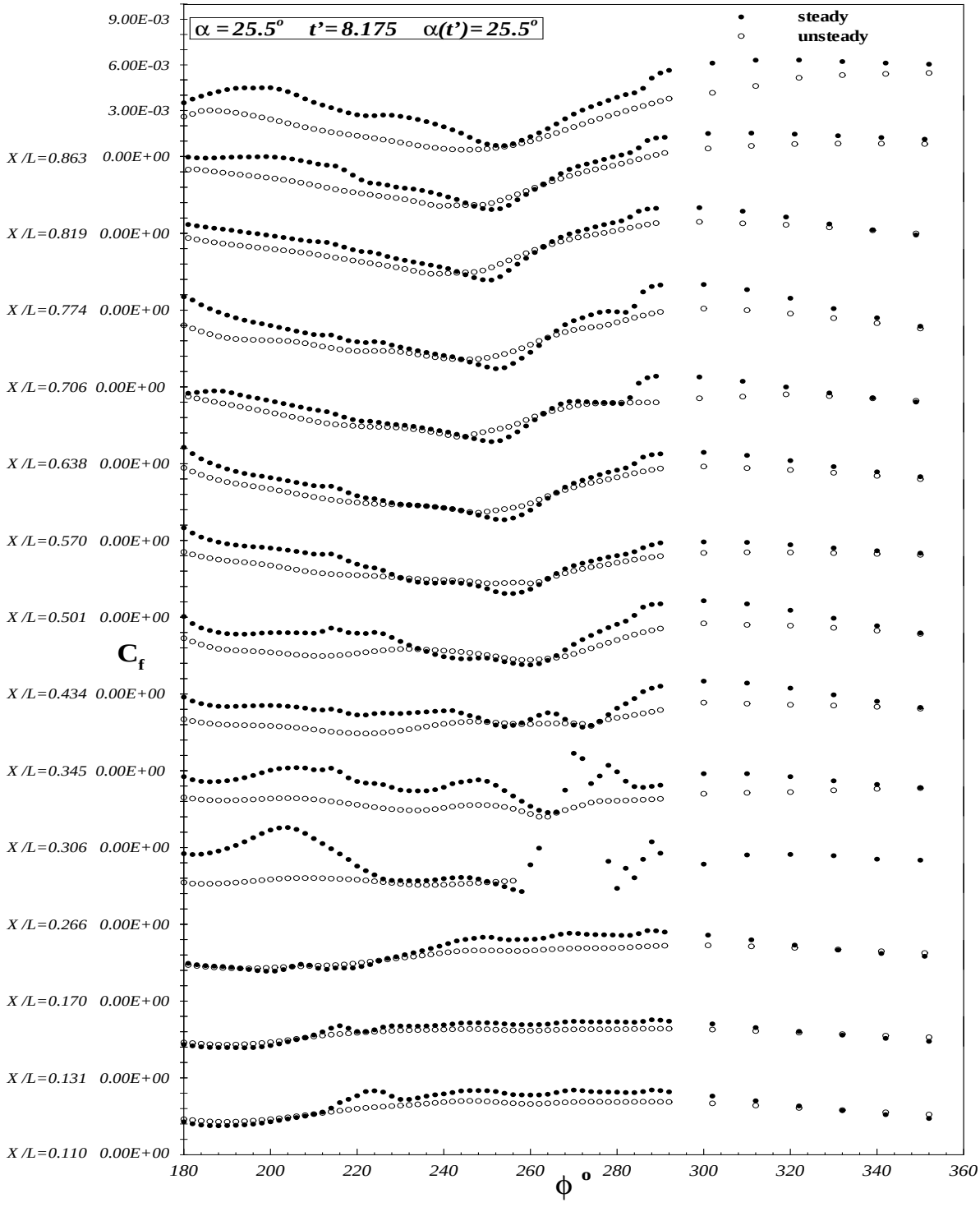


Figure 6.38: Comparison of sail-on-side (region with the sail) $C_f$ vs. $\phi$ distribution for steady and unsteady data at all $x/L$ locations. $\alpha = 25.5\,^\circ$, $t' = 8.266$, $\alpha(t') = 25.5\,^\circ$.

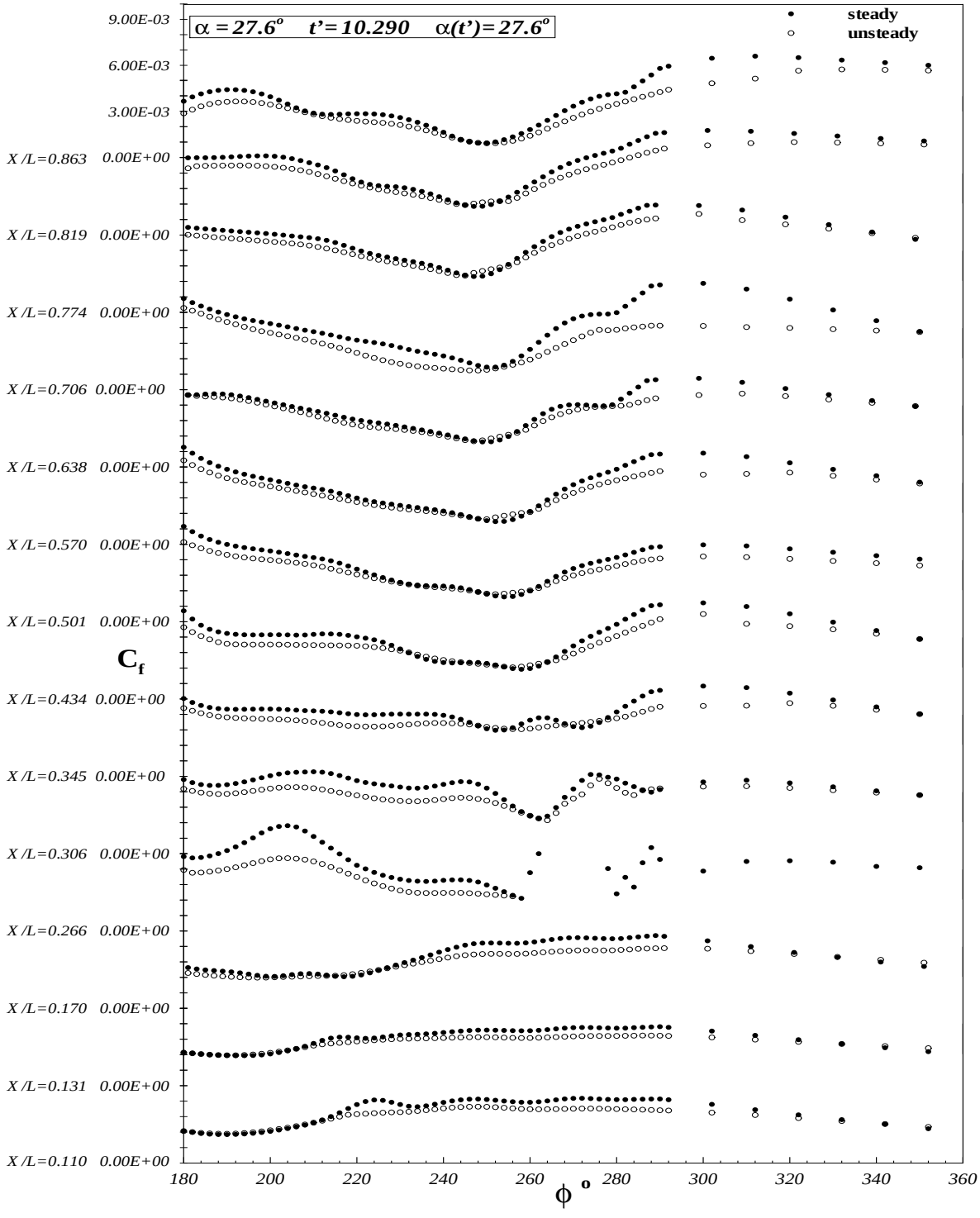


Figure 6.39: Comparison of sail-on-side (region with the sail) $C_f$ vs. $\phi$ distribution for steady and unsteady data at all $x/L$ locations. $\alpha = 27.6\,^\circ$, $t' = 10.290$, $\alpha(t') = 27.6\,^\circ$.

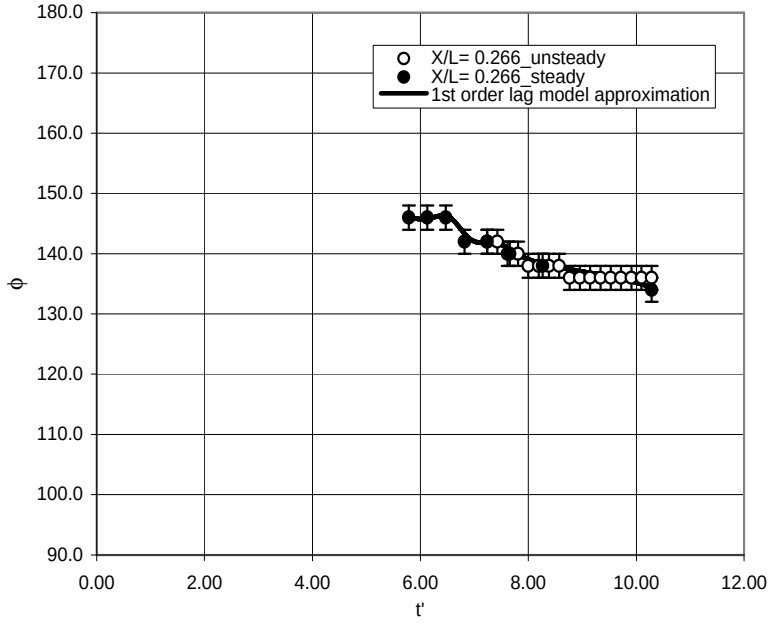


Figure 6.40: First-order differential lag approximation to the unsteady separation data at $x/L = 0.266$ for the barebody case.

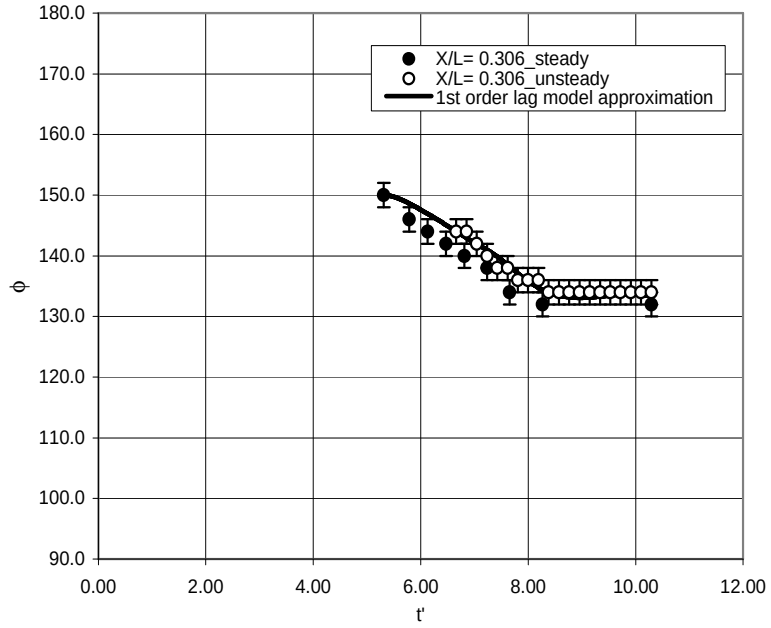


Figure 6.41: First-order differential lag approximation to the unsteady separation data at $x/L = 0.306$ for the barebody case.

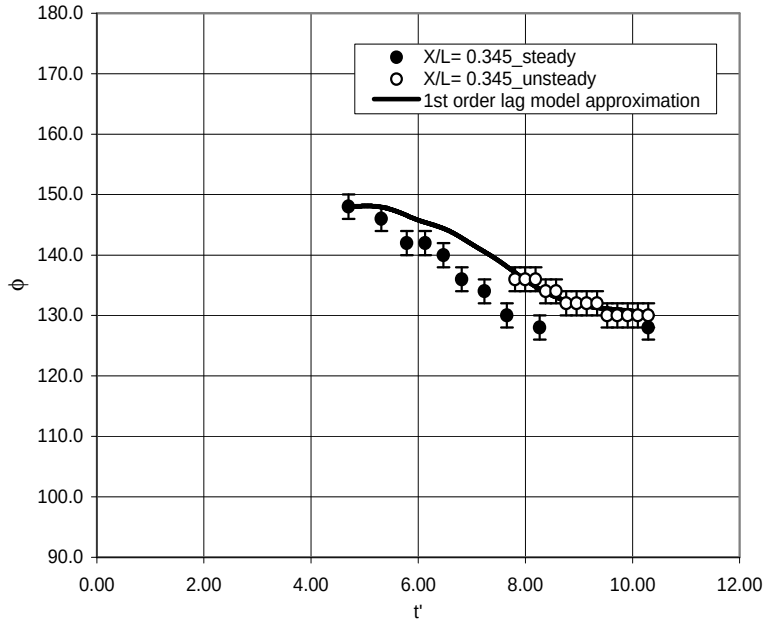


Figure 6.42: First-order differential lag approximation to the unsteady separation data at $x/L = 0.345$ for the barebody case.

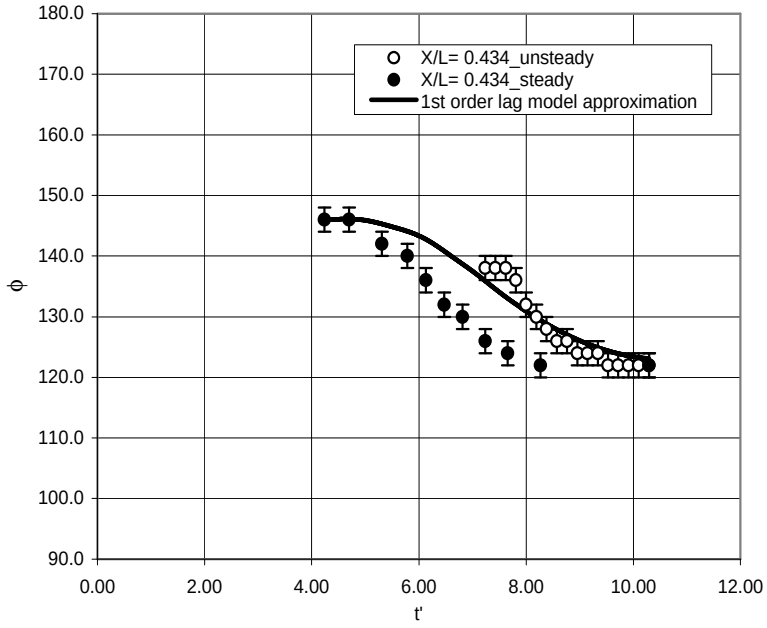


Figure 6.43: First-order differential lag approximation to the unsteady separation data at $x/L = 0.434$ for the barebody case.

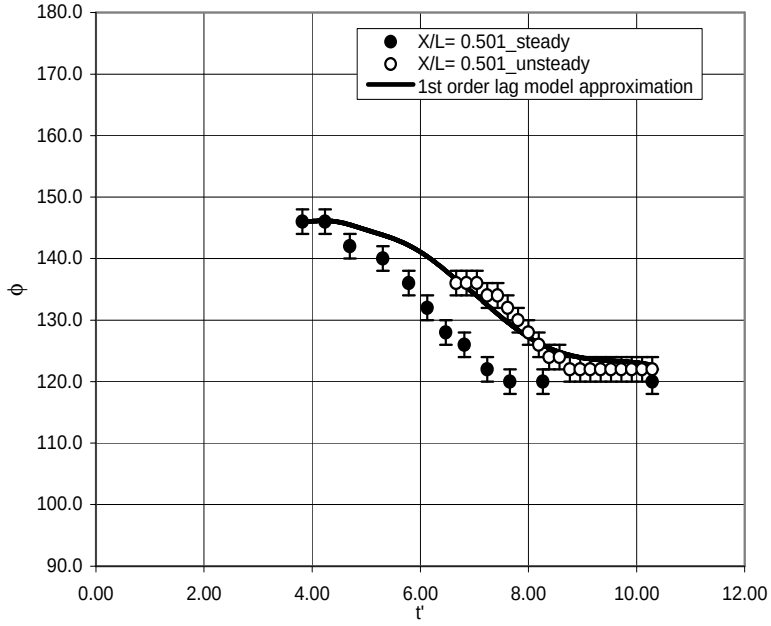


Figure 6.44: First-order differential lag approximation to the unsteady separation data at $x/L = 0.501$ for the barebody case.

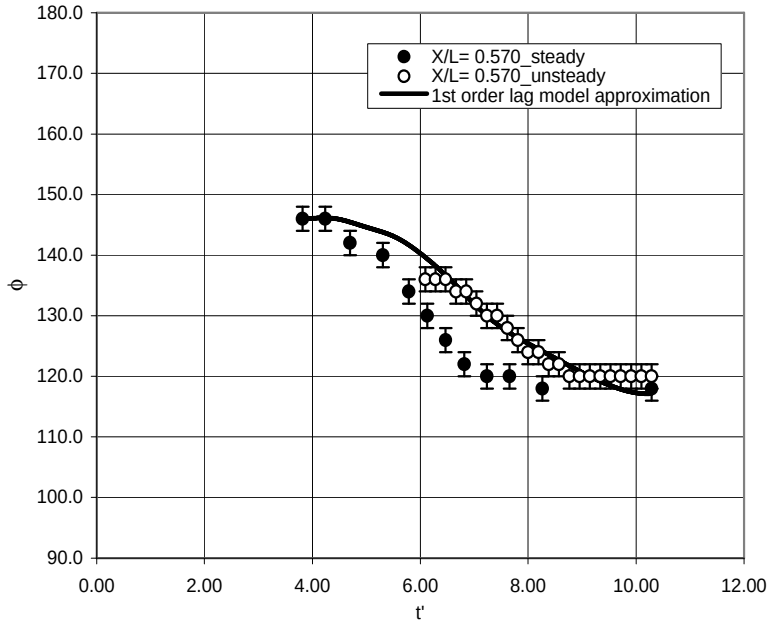


Figure 6.45: First-order differential lag approximation to the unsteady separation data at $x/L = 0.570$ for the barebody case.

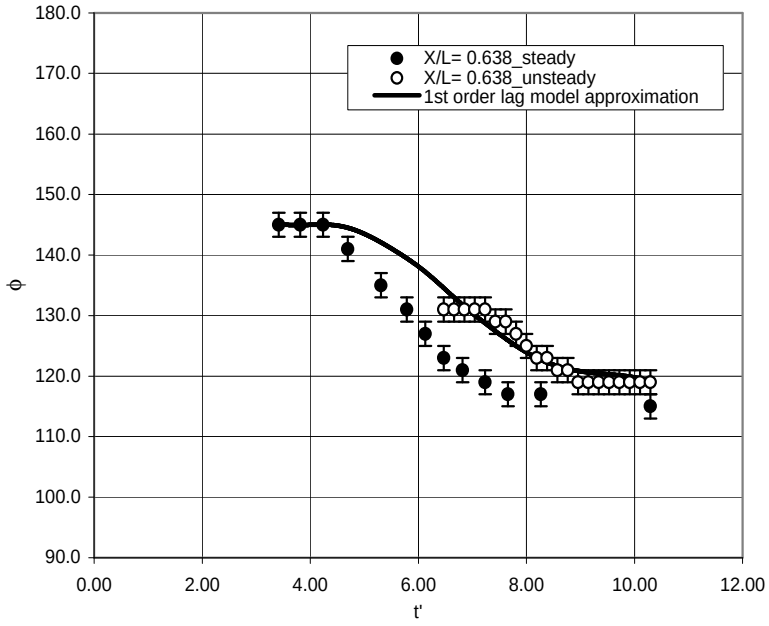


Figure 6.46: First-order differential lag approximation to the unsteady separation data at $x/L = 0.638$ for the barebody case.

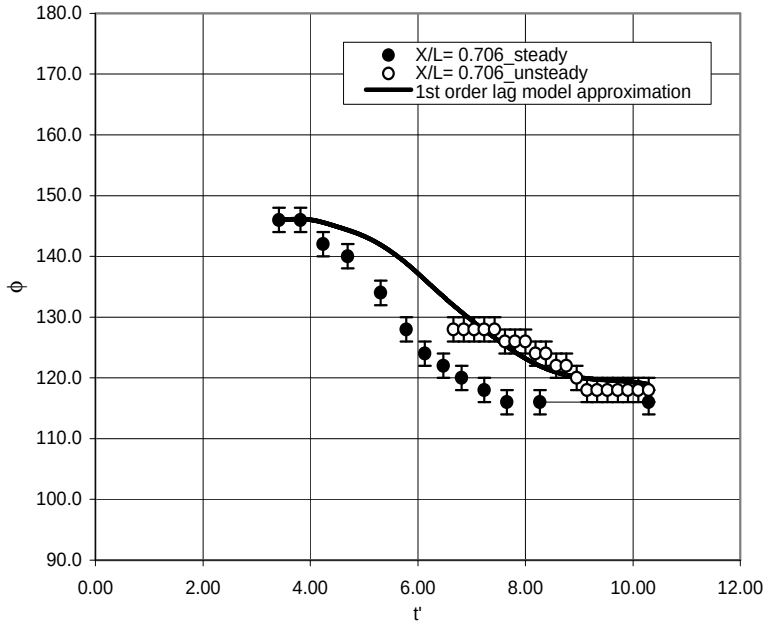


Figure 6.47: First-order differential lag approximation to the unsteady separation data at $x/L = 0.706$ for the barebody case.

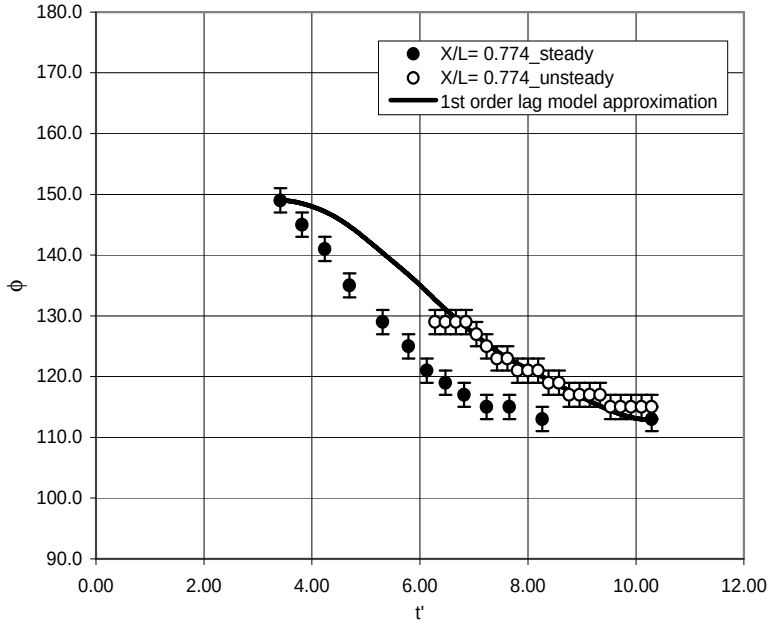


Figure 6.48: First-order differential lag approximation to the unsteady separation data at $x/L = 0.774$ for the barebody case.

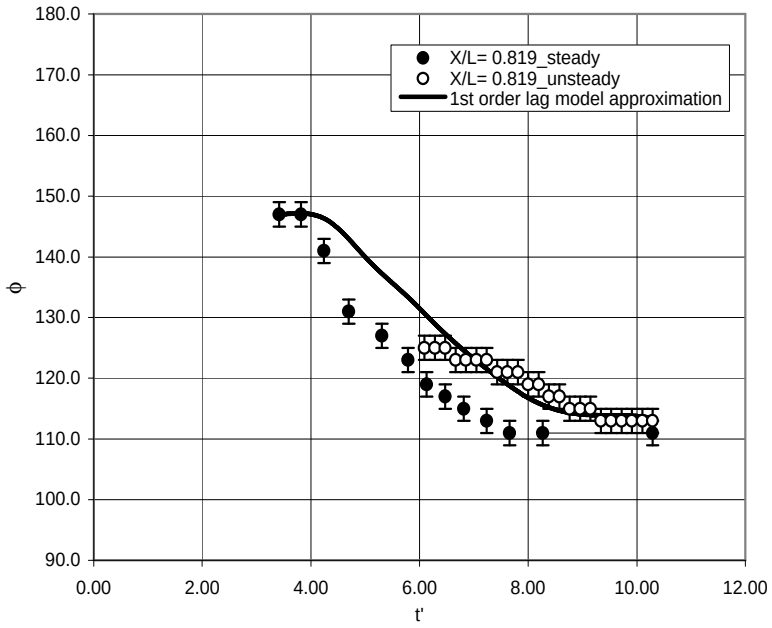


Figure 6.49: First-order differential lag approximation to the unsteady separation data at $x/L = 0.819$ for the barebody case.

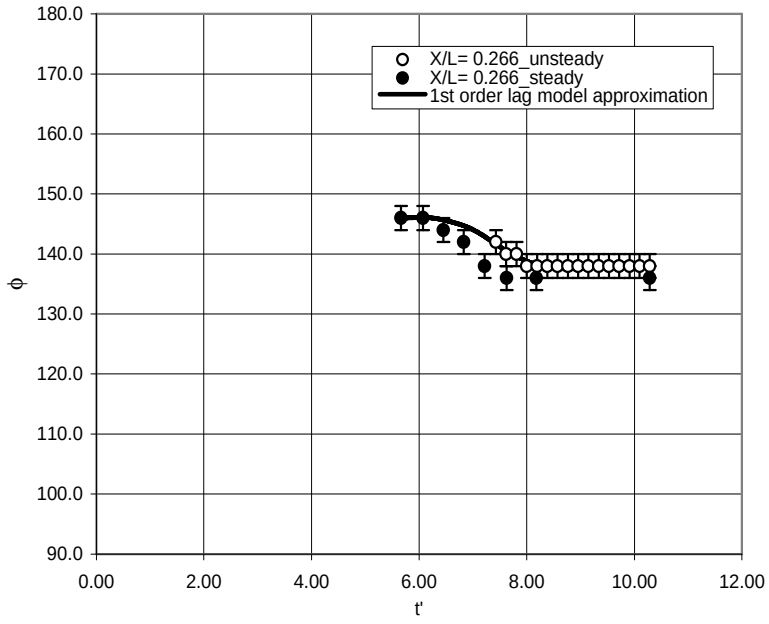


Figure 6.50: First-order differential lag approximation to the unsteady separation data at $x/L = 0.266$ for the non-sail region of the sail-on-side case.

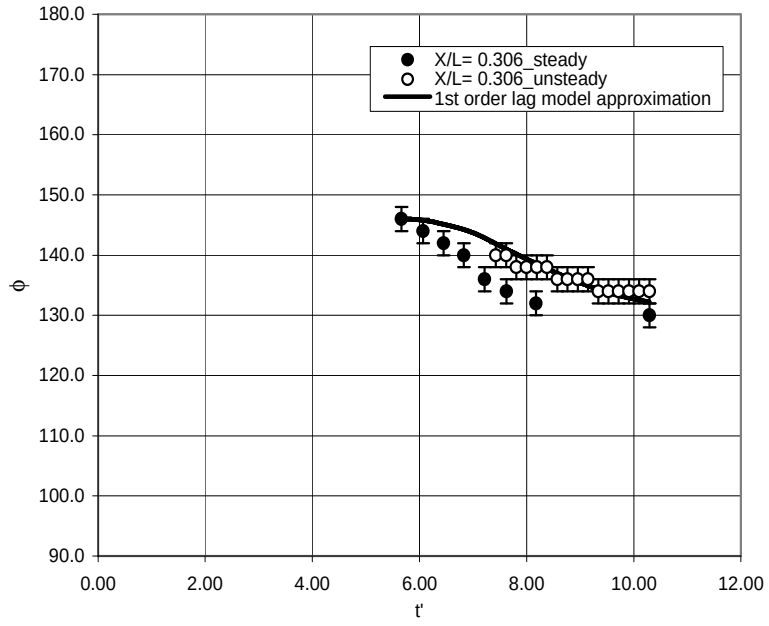


Figure 6.51: First-order differential lag approximation to the unsteady separation data at $x/L = 0.306$ for the non-sail region of the sail-on-side case.

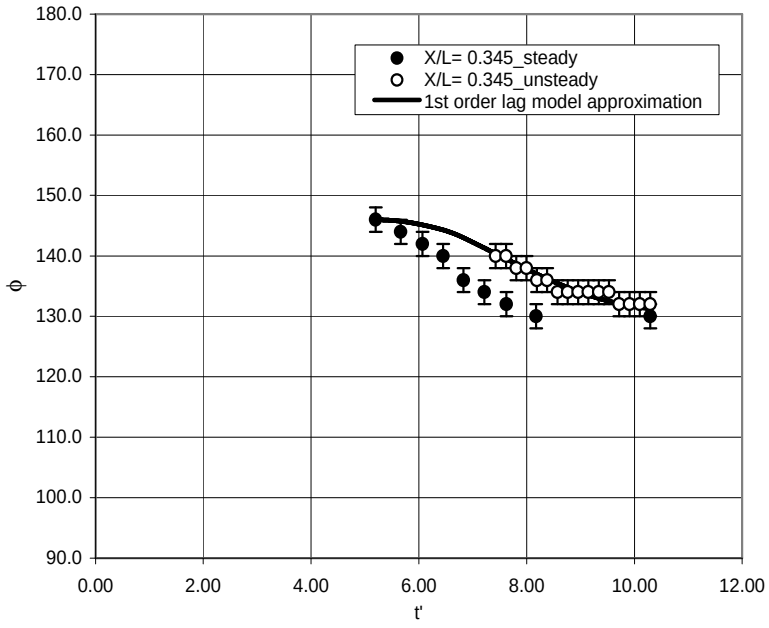


Figure 6.52: First-order differential lag approximation to the unsteady separation data at $x/L = 0.345$ for the non-sail region of the sail-on-side case.

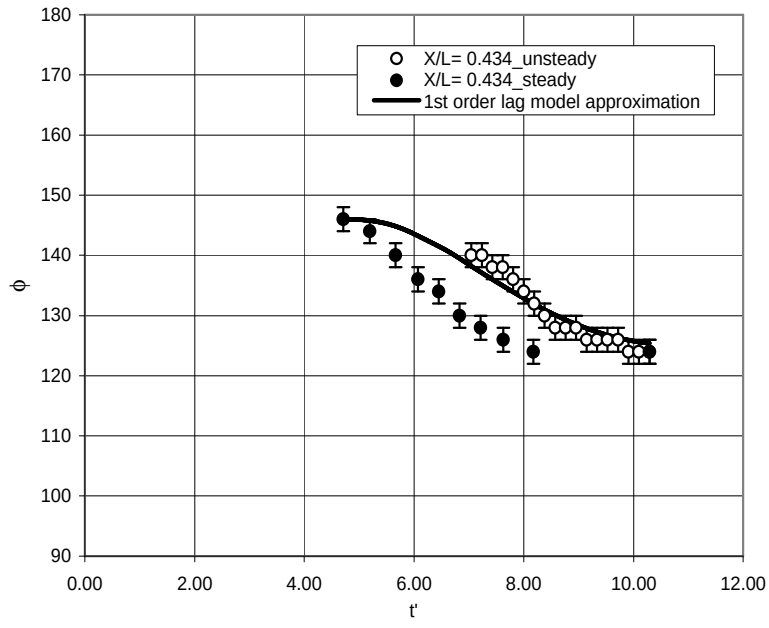


Figure 6.53: First-order differential lag approximation to the unsteady separation data at $x/L = 0.434$ for the non-sail region of the sail-on-side case.

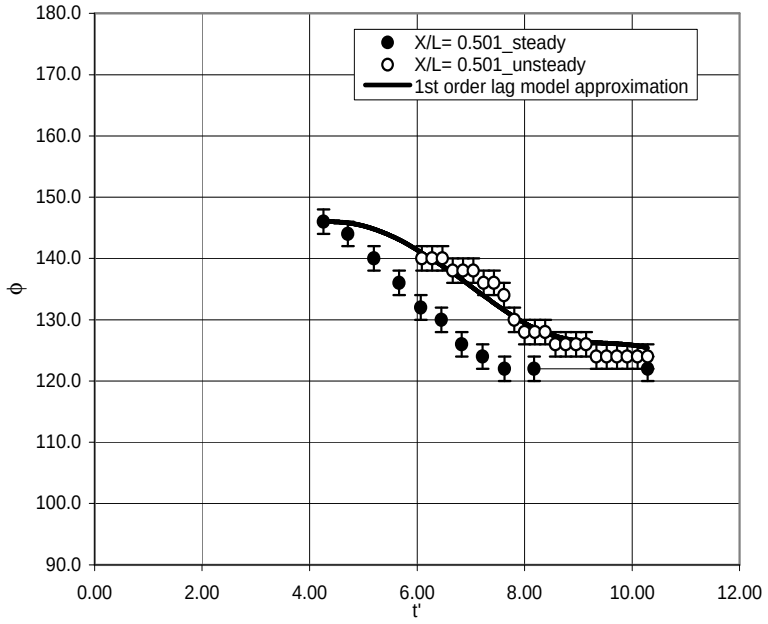


Figure 6.54: First-order differential lag approximation to the unsteady separation data at $x/L = 0.501$ for the non-sail region of the sail-on-side case.

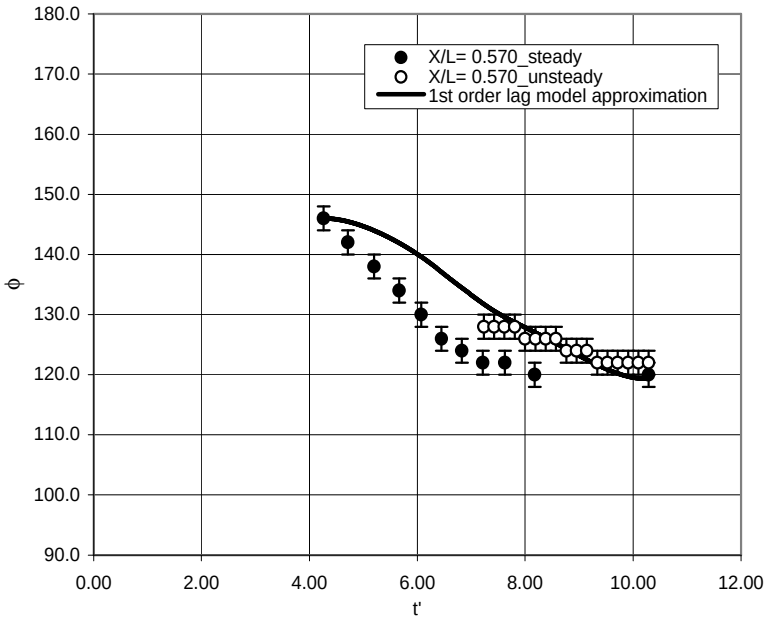


Figure 6.55: First-order differential lag approximation to the unsteady separation data at $x/L = 0.570$ for the non-sail region of the sail-on-side case.

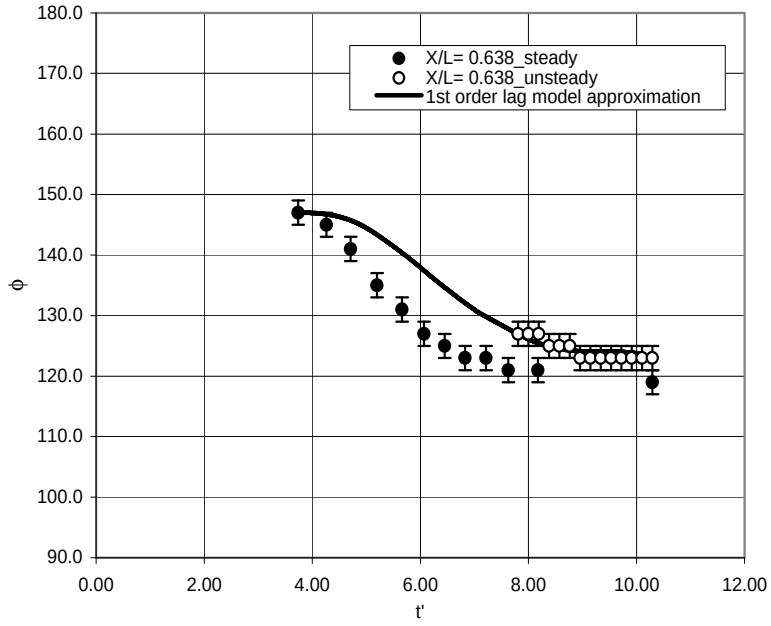


Figure 6.56: First-order differential lag approximation to the unsteady separation data at $x/L = 0.638$ for the non-sail region of the sail-on-side case.

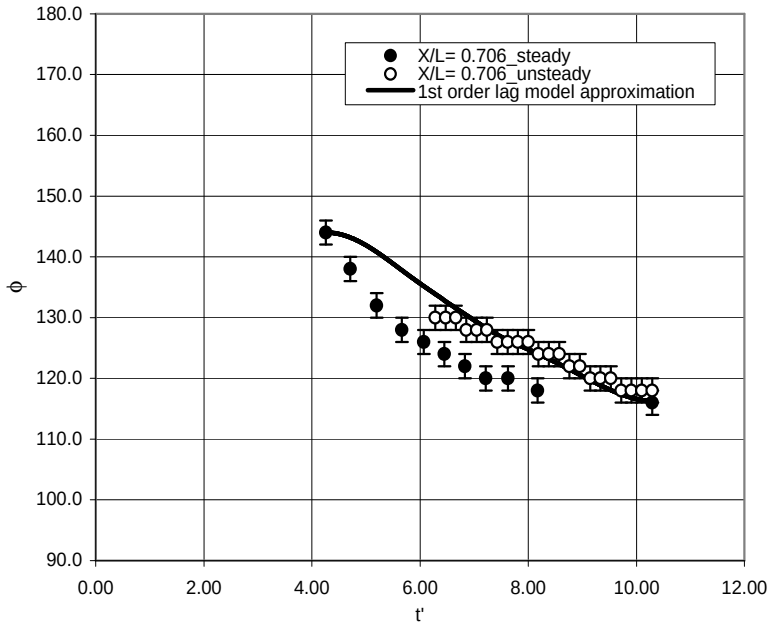


Figure 6.57: First-order differential lag approximation to the unsteady separation data at $x/L = 0.706$ for the non-sail region of the sail-on-side case.

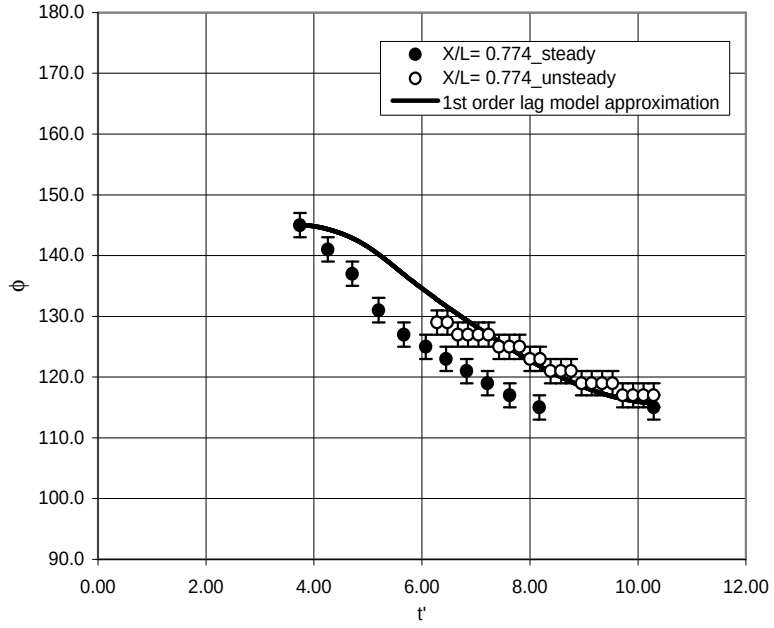


Figure 6.58: First-order differential lag approximation to the unsteady separation data at $x/L = 0.774$ for the non-sail region of the sail-on-side case.

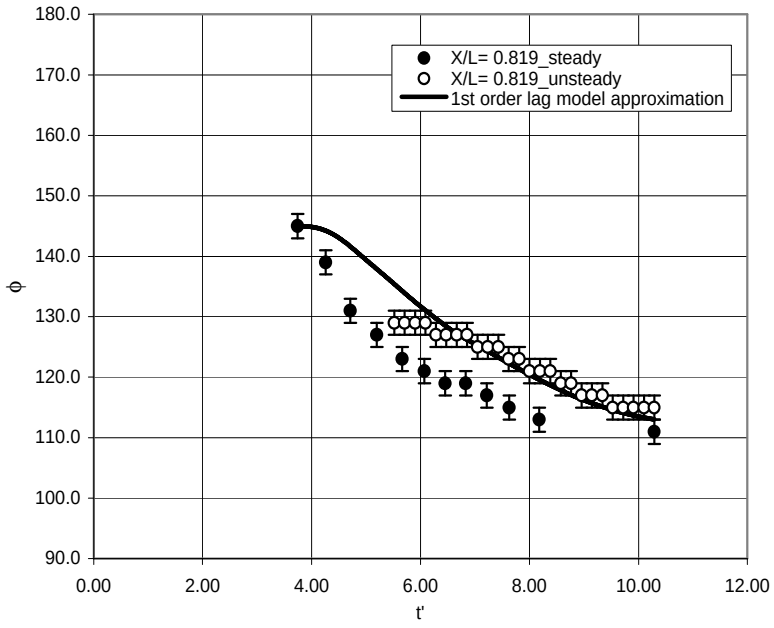


Figure 6.59: First-order differential lag approximation to the unsteady separation data at $x/L = 0.819$ for the non-sail region of the sail-on-side case.

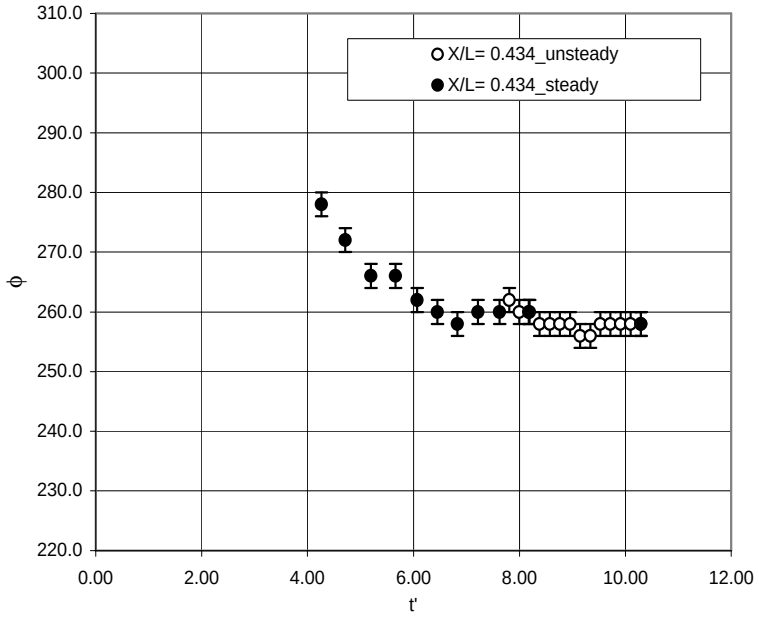


Figure 6.60: Steady and unsteady separation locations (second minima in $C_f$ measured from $\phi = 180\,^\circ$) vs $t'$ at $x/L = 0.434$ for the sail region of the sail-on-side case.

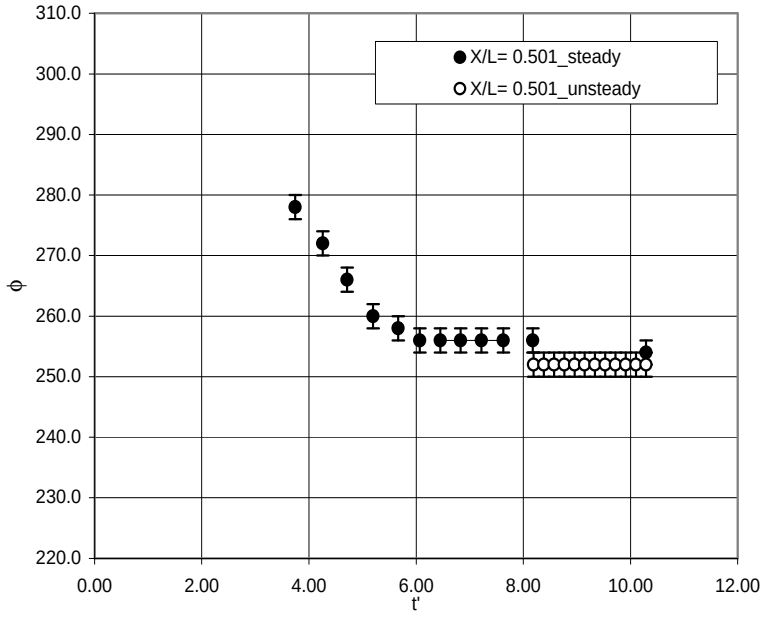


Figure 6.61: Steady and unsteady separation locations (second minima in $C_f$ measured from $\phi = 180\,^\circ$) vs $t'$ at $x/L = 0.501$ for the sail region of the sail-on-side case.

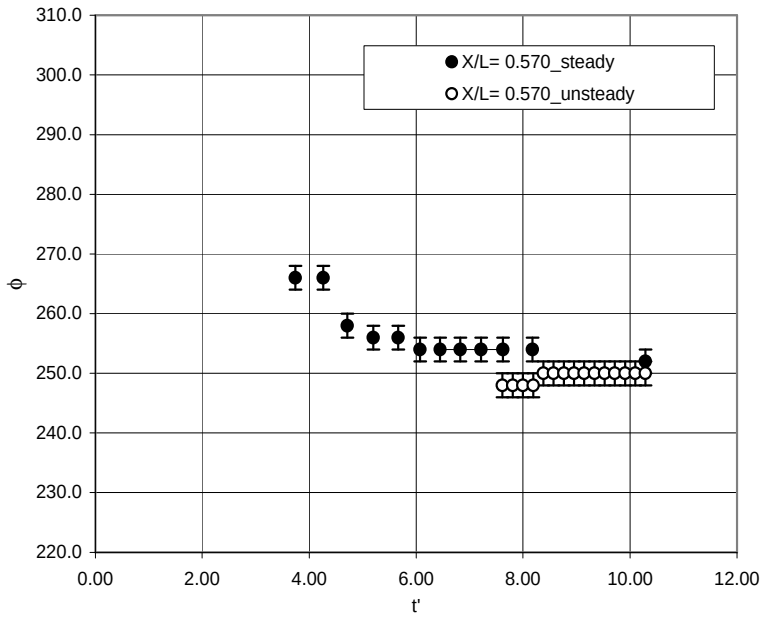


Figure 6.62: Steady and unsteady separation locations (second minima in $C_f$ measured from $\phi = 180\,^\circ$) vs $t'$ at $x/L = 0.570$ for the sail region of the sail-on-side case.

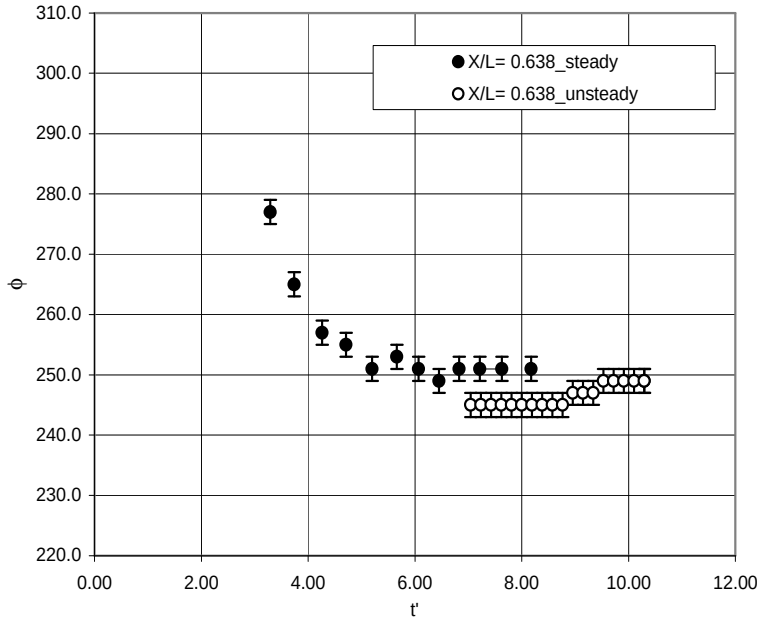


Figure 6.63: Steady and unsteady separation locations (second minima in $C_f$ measured from $\phi = 180\,^\circ$) vs $t'$ at $x/L = 0.638$ for the sail region of the sail-on-side case.

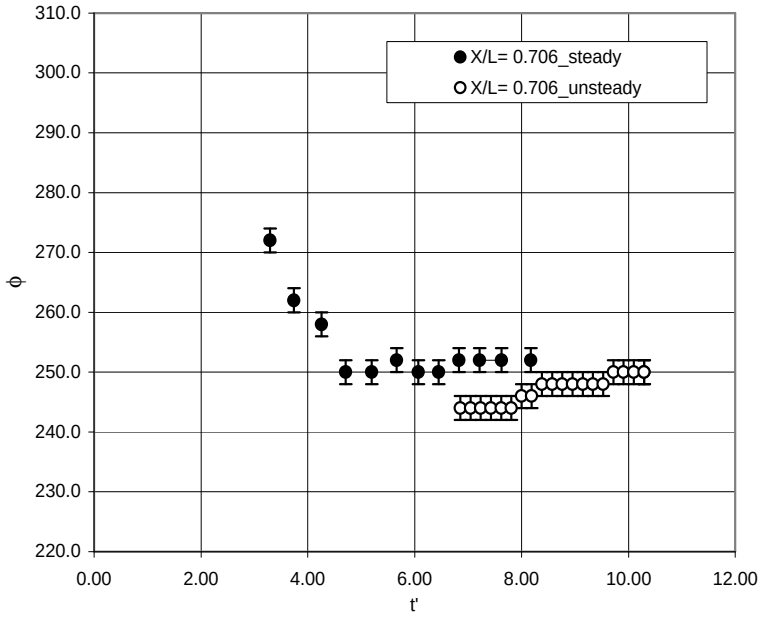


Figure 6.64: Steady and unsteady separation locations (second minima in $C_f$ measured from $\phi = 180\,^\circ$) vs $t'$ at $x/L = 0.706$ for the sail region of the sail-on-side case.

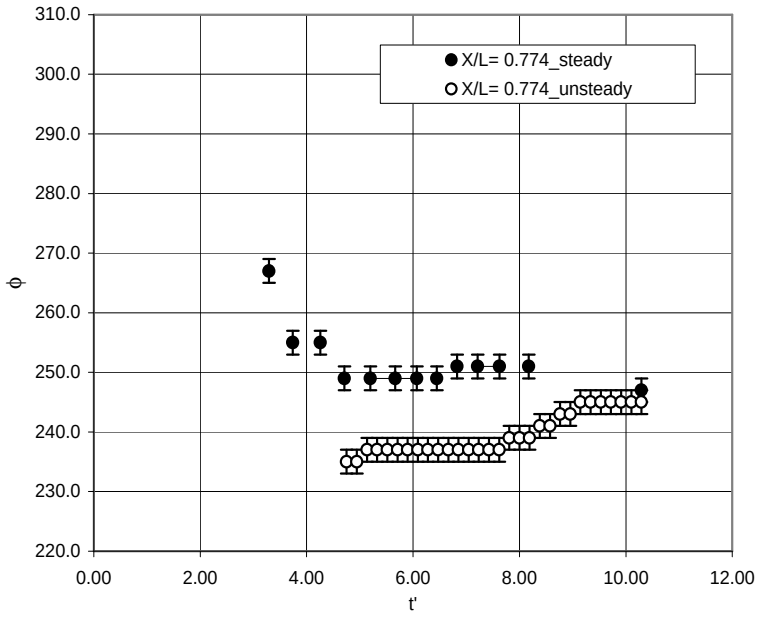


Figure 6.65: Steady and unsteady separation locations (second minima in $C_f$ measured from $\phi = 180\,^\circ$) vs $t'$ at $x/L = 0.774$ for the sail region of the sail-on-side case.

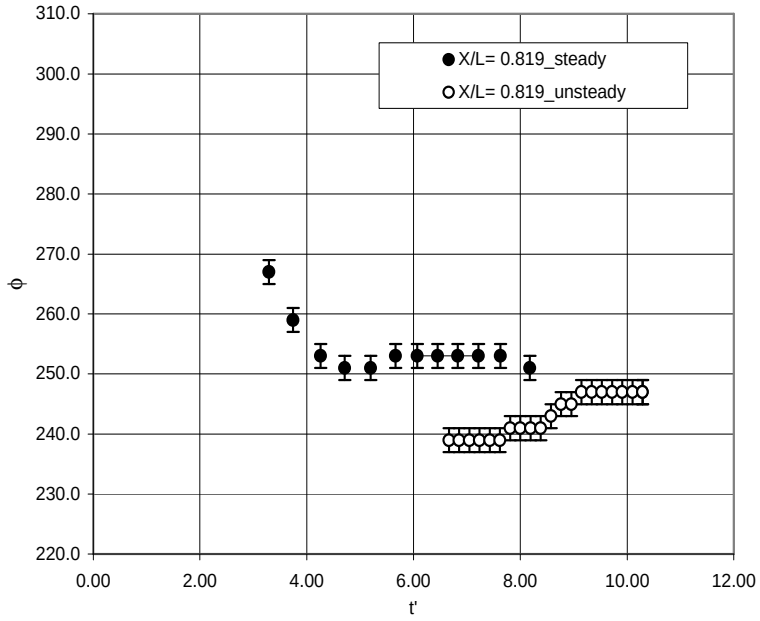


Figure 6.66: Steady and unsteady separation locations (second minima in $C_f$ measured from $\phi = 180\,^{\circ}$) vs $t'$ at $x/L = 0.819$ for the sail region of the sail-on-side case.

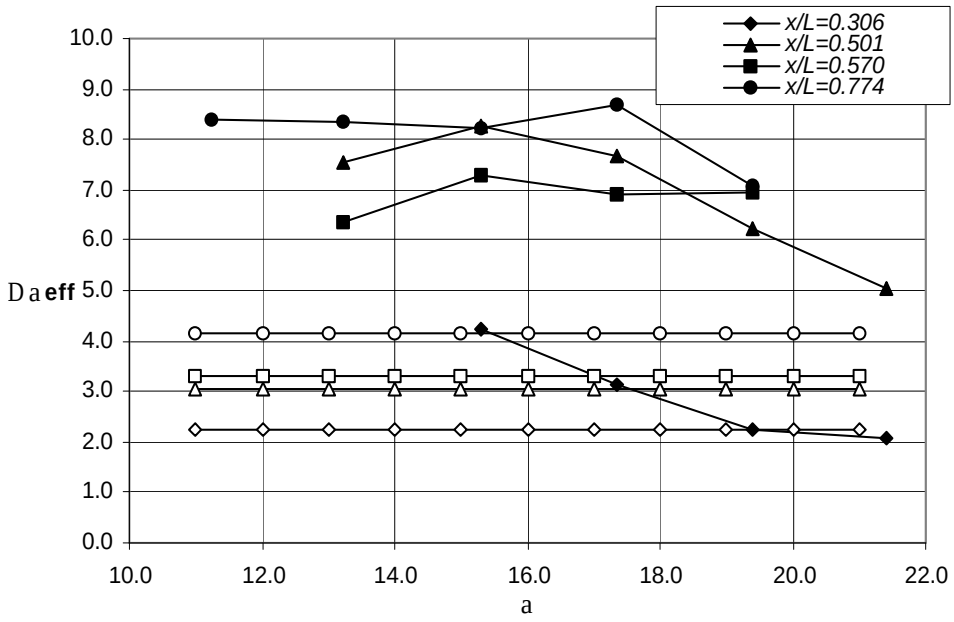


Figure 6.67: Incremental effective angle of attack $\Delta\alpha_{eff}$ for the barebody pitch-up maneuver at four $x/L$ stations as a function of instantaneous angle of attack $\alpha(t')$. Open symbols show the $\Delta\alpha_{eff}$ given by the equation 6.17.(Both angles are in degrees)

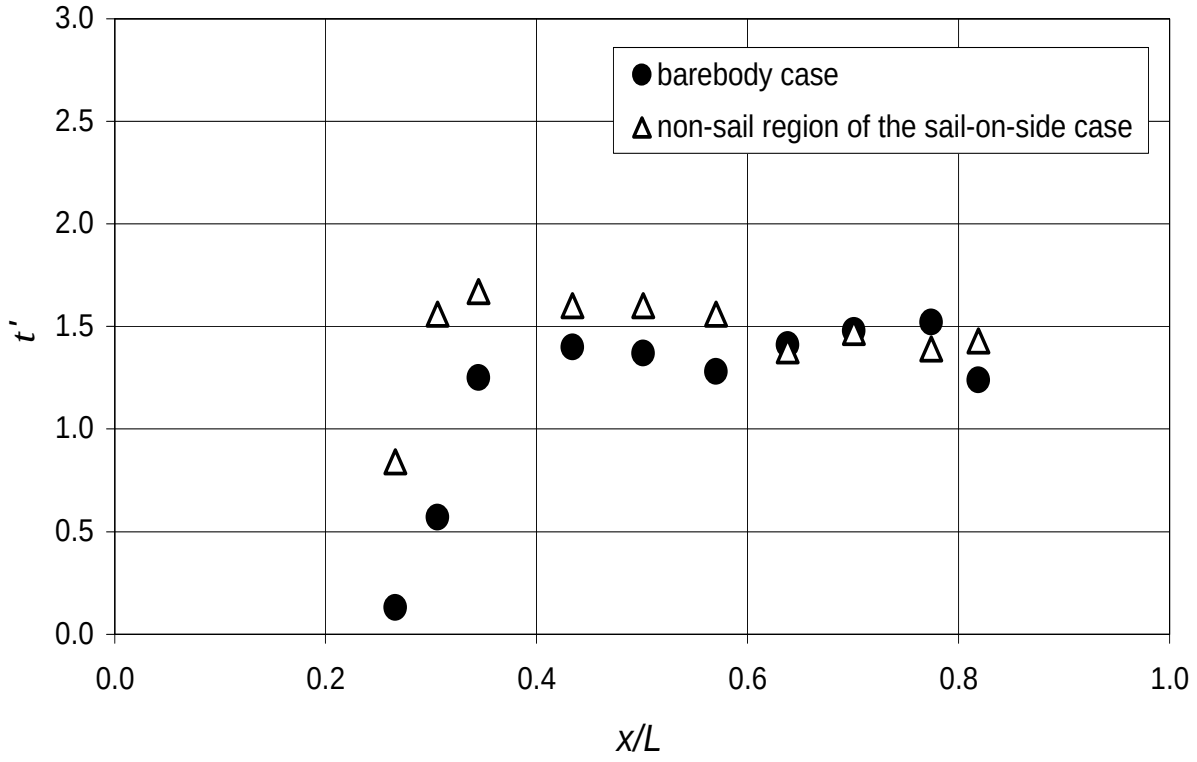


Figure 6.68: Computed time lags as a function of $x/L$ for the barebody and the non-sail region of the sail-on-side case.